NONINVASIVE CHARACTERIZATION OF 3D MYOCARDIAL STRAIN IN MURINE LEFT VENTRICLES POST INFARCTION

by

Arvin H. Soepriatna

A Dissertation

Submitted to the Faculty of Purdue University

In Partial Fulfillment of the Requirements for the degree of

Doctor of Philosophy

Weldon School of Biomedical Engineering

West Lafayette, Indiana

December 2019

THE PURDUE UNIVERSITY GRADUATE SCHOOL
STATEMENT OF COMMITTEE APPROVAL

Dr. Craig J. Goergen, Chair
Weldon School of Biomedical Engineering

Dr. Chi Hwan Lee
Weldon School of Biomedical Engineering

Dr. Thomas M. Talavage
School of Electrical and Computer Engineering

Dr. Jessica M. Ellis
Department of Physiology, East Carolina University

Approved by:
Dr. George R. Wodicka

Education is not the learning of facts, but training of the mind to think.

Albert Einstein (1879-1955)

Dedicated to all those who have inspired me to never stop learning,
especially my parents, Christiana and Harianto.

ACKNOWLEDGMENTS

The completion of this doctoral dissertation would not have been possible without the constant support that I received from my mentors, friends, and family. First and foremost, I would like to express my deepest appreciation to my advisor, Dr. Craig J. Goergen, for sharing his knowledge, inspiring me to innovate, and constantly challenging me to improve. His invaluable guidance over the past five years has positively changed the way I view research by cultivating a more active approach towards thinking. I would like to extend my gratitude to my dissertation committee members, Drs. Chi Hwan Lee, Thomas M. Talavage, and Jessica M. Ellis, as well as my close research collaborators, Drs. John J. Boyle, Guy M. Genin, Stavros Thomopoulos, Grace D. O'Connell, Tamara L. Kinzer-Ursem, L. Tiffany Lyle, and Jingwu Xie. These individuals motivated me to think beyond the cardiovascular system and apply my research to a multitude of disciplines through collaborations.

I am also very grateful to past and present members of the Cardiovascular Imaging Research Laboratory (CVIRL) for always providing constructive feedback on my research and for creating an environment where we can freely bounce ideas during our lab lunches. I especially would like to thank those who worked closely with me on the projects presented in this dissertation, including the dedicated undergraduate students whom I had the privilege of mentoring over the past five years. Additionally, I would like to thank my labmate Gurneet Sangha, who joined CVIRL at the same time I did and will graduate with me in December. Although we had absolutely no idea what we had gotten ourselves into when we decided to pursue our doctoral degrees, I am grateful that we embarked on this journey together and supported each other throughout. Our constant exchange of scientific ideas, philosophical discussions, and constructive criticisms for each other's work certainly influenced the way I think, which helped me become the researcher that I am today.

There are many other individuals that I would like to acknowledge for making my experiences at Purdue memorable. I want to thank my close friends John Damrath and Andrea Acuña for their words of encouragement when challenges arose, both in lab and in life. I am also grateful to the BME Graduate Student Association for establishing a close-knit community with a great support network. Lastly, my journey towards completing this doctoral degree would not have been possible without the constant love and support that I received from my family. I would like

to express my deepest gratitude to my parents, Harianto and Christiana, for providing me with everything that I needed to get to where I am today. Everything that I have achieved (and will achieve) is possible because of the strong qualities that they instilled in me throughout my childhood.

Finally, I would like to acknowledge the Weldon School of Biomedical Engineering and the Purdue Graduate School for granting me the Ross and the Donnan Fellowships. It was through these funding sources that I was able to carry out the research presented in this dissertation.

PREFACE

Three chapters of this dissertation **(Chapters 4, 5, and 6)** have been published in peer-reviewed journals as noted at the start of those chapters. Minor edits to the formatting and wording have been made in these chapters to produce a cohesive piece of writing. The organization of this dissertation begins with a brief introduction on the prevalence of heart failure post-infarction **(Chapter 1)**, followed by an in-depth review of cardiac remodeling and the associated imaging techniques used to track disease progression **(Chapter 2)**. **Chapter 3** focuses on the identification of a research gap, which will be addressed in subsequent chapters. **Chapters 4 and 5** describe our recent efforts in the development of a four-dimensional ultrasound imaging technique and a 3D strain algorithm, respectively. This is followed by a thorough longitudinal study that integrates these two techniques to characterize spatial changes in 3D myocardial strain post-infraction **(Chapter 6)**. Finally, we conclude by reflecting on the scientific contribution of this dissertation, as well as provide future directions of our research **(Chapter 7)**. Please refer to the publications section on page 145 for a comprehensive list of authored journal articles and their scientific impact.

TABLE OF CONTENTS

LIST OF TABLES

LIST OF FIGURES

ABBREVIATIONS

2D	Two-Dimensional
3D	Three-Dimensional
4D	Four-Dimensional (3D + Time)
$\varepsilon_{\theta\theta}$	Circumferential Cyclic Strain
AAA	Abdominal Aortic Aneurysm
AngII	Angiotensin II
apoE$^{-/-}$	apolipoprotein-E deficient
CAD	Coronary Artery Disease
CO	Cardiac Output
CT	Computed Tomography
CVD	Cardiovascular Disease
DDE	Direct Deformation Estimation
DIC	Digital Image Correlation
DVC	Digital Volume Correlation
ECG	Electrocardiogram
EDV	End-Diastolic Volume
EF	Ejection Fraction
E_I	Maximum or First Principal Strain
EKV	ECG-gated Kilohertz Visualization
fps	Frames-per-second
GL	Green-Lagrange
H&E	Hematoxylin and Eosin
I/R	Ischemia-Reperfusion
IS	Infarct Size
LCA	Left Coronary Artery
LK	Lucas-Kanade
LSF	Least Squared Fit
LV	Left Ventricle

MCE	Myocardial Contrast Echocardiography
MI	Myocardial Infarction
MMP	Matrix Metalloproteinase
MRI	Magnetic Resonance Imaging
MTC	Masson's Trichrome
PET	Positron Emission Tomography
PL	Permanent Ligation
PSV	Peak-Systolic Volume
SPECT	Single Photon Emission Computed Tomography
SR	Strain Rate
SV	Stroke Volume
TDI	Tissue Doppler Imaging
TGF-β	Transforming Growth Factor Beta
XCOR	Cross Correlation

ABSTRACT

Coronary artery disease remains the leading cause of death in the United States with over 1 million acute coronary events predicted to take place in 2019 alone. Heart failure, a common and deadly sequela of myocardial infarction (MI), is attributed to adverse ventricular remodeling driven by cardiomyocyte death, inflammation, and mechanical factors. Despite strong evidence suggesting the importance of myocardial mechanics in driving cardiac remodeling, many *in vivo* MI studies still rely on 2D analyses to estimate global left ventricular (LV) function and approximate strain using a linear definition. These metrics, while valuable in evaluating the overall impact of ischemic injury on cardiac health, do not capture regional differences in myocardial contractility. The objective of this work is therefore to expand upon existing ultrasound studies by enabling regional analysis of 3D myocardial strain. By integrating our recently developed four-dimensional ultrasound (4DUS) imaging technique with a direct deformation estimation algorithm for 3D strain, we identified unique remodeling patterns and regional strain differences between two murine models of MI with different infarct severities. By constructing 3D strain maps of the remodeling LVs, we were able to capture strain heterogeneity and characterize a sigmoidal strain profile at infarct border zones. Finally, we demonstrated that the maximum principal component of the 3D Green-Lagrange strain tensor correlates with LV remodeling severity and is predictive of final infarct size. Taken together, the presented work provides a novel and thorough approach to quantify regional 3D strain, an important component when assessing post-MI remodeling.

1. INTRODUCTION

Coronary artery disease (CAD) is the leading cause of death in the world, accounting for 14% of total global mortality in 2013 [1,2]. In the United States alone, over 1 million acute coronary events are predicted to take place in 2019 [3]. CAD is a condition in which atherosclerotic plaque accumulates in the coronary artery, restricting blood flow to the myocardium. This deprives the myocardium of the oxygen needed for the heart to pump blood efficiently, and if left untreated, vulnerable plaque may rupture, forming a thrombus that may cause a heart attack or even death. The heart's natural response to chronic ischemia or ischemia-induced necrosis is to undergo molecular, structural, and mechanical changes in the cardiomyocyte framework to ensure that it delivers and maintains a sufficient supply of blood to the rest of the body [4,5]. This adaptive process, termed cardiac remodeling, is typically associated with wall thinning, chamber dilation, and alterations in the cardiac extracellular matrix (ECM) composition, which significantly influence left ventricular (LV) performance [6]. Even though the initial remodeling phase may be considered beneficial, as it aims to prevent LV rupture, the long-term effects of cardiac remodeling can be maladaptive and closely linked to heart failure progression [4,7].

Many types of cardiac remodeling exist depending on the nature of the injury and whether it is driven by pressure [8] or volume overload [9]. Even though the technologies developed in this dissertation can be applied to study these unique remodeling processes, this dissertation focuses specifically on LV remodeling following a heart attack, also known as a myocardial infarction (MI). We chose to study LV remodeling post-MI because ischemia-induced injury is one of the most prevalent outcomes of CAD. Although advancing medicine has significantly improved patient survival rates from acute MIs, many surviving patients continue to develop heart failure [10]. This shifts the patient population who are at risk of developing heart failure, increasing its incidence and making it a major public health issue [11]. Despite this increasing trend, the factors that drive heart failure post-MI remains unclear. As such, better understanding the pathophysiology behind heart failure would facilitate the development of more effective treatments that could potentially improve patient prognosis following an acute MI.

One well-known determinant of heart failure post-MI is infarct size [12]. Immediately following an ischemic event, the ECM of the infarcted myocardium undergoes significant structural changes, which includes the gradual formation of stiff fibrotic scars. The now passive

and non-contractile developing scar becomes susceptible to systolic stretching when the remote, healthy myocardium contracts, leading to infarct expansion early in remodeling [13,14]. In fact, studies have shown that infarct expansion, defined as infarct growth associated with acute dilation and wall thinning unexplained by myocardial necrosis, is prevalent in 60% of patients with acute MIs [15]. Despite a strong positive correlation between infarct size and heart failure incidence [16,17], the factors that determine the rate and extent of infarct expansion remain unclear. Although several mechanisms for infarct expansion have been proposed, including the degradation of collagen struts [18], delayed formation of the fibrotic scar tissues [19], and loss of myocardial wall elasticity [20], the factors that contribute to the stabilization of infarct zones remain unanswered. What factors determine how far an infarct will expand? What factors regulate the rate of infarct expansion? What is the role of myocardial mechanics in post-infarction remodeling? Answering these questions, which is the goal of this dissertation, may provide novel insights into the role that mechanics play in determining remodeling outcomes. Furthermore, the ability to develop a noninvasive imaging tool to characterize early mechanical changes in the remodeling myocardium may help doctors identify patients at risk of developing heart failure so that they may receive early intervention, hence improving their prognosis.

2. BACKGROUND

Before discussing our investigation on the role of myocardial mechanics post-infarction, it is important to address the multitude of factors that regulate the complex process of cardiac remodeling. This chapter provides an in-depth review of the current state of knowledge on post-infarction remodeling and discusses some of the most widely accepted tools used to noninvasively study cardiac disease progression. We will first begin by describing the different biological events that transpire following an acute MI and how they work in tandem to develop a stiff fibrotic scar that minimizes infarct expansion. We will then address the challenges that current imaging techniques, including ultrasound and magnetic resonance imaging, face in the assessment of global cardiac function and estimation of myocardial strain.

2.1 Pathophysiology of Cardiac Remodeling

Cardiac remodeling is a complex, multifactorial process instigated by cellular, molecular, mechanical, and neurohormonal changes in response to ischemia or myocardial injury [4,21,22]. Early remodeling begins with an inflammatory response that drives the resorption of necrotic tissues followed by a fibrotic phase that involves the deposition of collagenous fibrotic scars [14]. Both processes are important in infarct healing, which is regulated in part by the changing mechanical properties of the surrounding environment, including the extracellular matrix (ECM) and the developing infarct scar [14,23]. A poorly structured scar, however, leads to infarct expansion and has been shown to have detrimental long-term effects, such as significant LV wall thinning, dilation, and impaired LV function [4,24,25]. Because of a strong positive correlation between infarct size and heart failure [12], infarct expansion is often proposed as a determinant of remodeling outcomes. However, due to the complexity of post-infarction remodeling, the factors that determine the rate and extent of infarct expansion remain unclear. To better understand how a changing mechanical environment contributes to cardiac remodeling, it is important to take a step back and review in detail the complex series of events that transpire in the heart following an ischemic event, beginning with cardiomyocyte death.

2.1.1 Pathways Leading to Cardiomyocyte Death

Cardiomyocytes, cardiac muscle cells responsible for contraction, obtain most of their energy from oxidative phosphorylation [26,27] and fatty acid β-oxidation [28]. During ischemia, occluded coronary arteries are unable to deliver the necessary metabolic substrates, in this case oxygen, needed for the heart to generate energy through oxidative phosphorylation. As a compensatory mechanism, the heart relies on an alternative metabolic pathway called anaerobic glycolysis to produce energy [26]. Under chronic hypoxia, the accumulation of intracellular H^+ ions as byproducts of anaerobic glycolysis leads to acidosis and is believed to be the primary cause of necrosis, the predominant mechanism behind cardiomyocyte death post-infarction [29].

Necrosis is defined as premature cell death that leads to cell rupture, uncontrolled release of cellular materials into the extracellular space, and a strong inflammatory response [30]. The underlying mechanism for acidosis-induced necrosis originates from the loss of balance between H^+, Na^+, and Ca^{2+} ions in the cytoplasm [26]. Following acidosis, ion pumps in the plasma membrane remove excess H^+ by exchanging them with Na^+. This increase in intracellular Na^+ concentration reverses the direction of the Na^+/Ca^{2+} exchanger by inhibiting the efflux of Ca^{2+}, hence increasing the concentration of intracellular Ca^{2+}. Gradient-driven Ca^{2+} uniporter in the mitochondria then governs the transport of Ca^{2+} from the cytoplasm into the mitochondria [31]. Calcium overload in the mitochondria then increases oxidative stress [32], lead to mitochondrial rupture [33], and cause cell swelling [26], all of which are important stimuli for necrosis [34].

Apoptosis, on the contrary, is a highly regulated programmed cell death associated with chromatin condensation and breakage of the nucleus. Unlike necrosis, the cells containing the fragmented DNA and organelles are divided into smaller apoptotic bodies that are eliminated by phagocytes, therefore averting an inflammatory response [35]. Although the extent and role of apoptosis in inducing cardiomyocyte death is still under debate, several theories suggest that ischemia, to some degree, triggers both the extrinsic and intrinsic apoptosis pathways [36,37]. In the extrinsic pathway, both hypoxia and acidosis in murine hearts activate several death receptor ligands, particularly the Fas and tumor necrosis factor (TNF)-α ligands [36,38]. Binding of the ligand to the death receptor leads to a signaling cascade involving caspase activation that ultimately results in apoptotic cell death. Mitochondrial calcium overload, on the other hand, initiates caspase activation and apoptotic cell death in the intrinsic pathway [38].

Other pathways responsible for causing cardiomyocyte death have also been proposed. Under mild to moderate ischemia, autophagy, an alternative metabolic mechanism involving the degradation of intracellular components, inhibits cell death [26]. However, under severe ischemia and during the reperfusion of infarcted areas, autophagy is triggered through a unique mechanism that promotes cell death [26]. Taken together, depending on the cell-death pathway and duration of ischemia, differences in the degree of inflammatory response and cardiomyocyte death will be observed. Under chronic ischemia, necrosis will be the primary driver of cardiomyocyte death, leading to a prominent inflammatory response that plays a vital role in post-infarction remodeling. However, under mild to moderate ischemia, apoptosis and autophagy minimize inflammation and reduce the extent of cardiomyocyte death.

2.1.2 Pathways Leading to Myocardial Infarct Expansion and Heart Failure

Inflammation significantly contributes to the changing mechanical environment of the damaged myocardium and is the first step of infarct healing. Following necrosis as part of the inflammatory response, neutrophil infiltration leads to matrix metalloproteinase (MMP) production early in remodeling. The ECM, which acts as a stress-tolerant and viscoelastic scaffold for cardiomyocytes, is then degraded by MMPs, disrupting the integrity of the cardiomyocyte framework [39]. This process involves the degradation of highly-structured collagen struts, which causes cardiomyocyte slippage [18]. Simultaneously, macrophages recruited to the damaged tissue are responsible for the resorption of nonviable cardiomyocytes, leading to temporary weakening of the infarcted myocardium [14].

To provide temporary support during a vulnerable period where significant structural changes are occurring, a provisional granulation tissue rich in fibrin, laminin, and glycosaminoglycans is quickly formed to stiffen the ECM and prevent LV rupture [14]. The now passive and non-contractile infarcted myocardium becomes susceptible to cyclic systolic stretching when the healthy myocardium contracts. The stretching of a stiff ECM releases the transforming growth factor beta (TGF-β) from the latent-associated peptide complex due to increased mechanical resistance to cell tension [23]. TGF-β then promotes the differentiation of cardiac fibroblasts to myofibroblast, a key regulator of collagen scar formation [14,23], gradually replacing the provisional structure with fibrotic scar tissue rich in collagen in a process called myocardial scarring [21]. However, until the provisional structure is completely replaced by the

fibrotic scar, the infarcted myocardium is susceptible to infarct growth at the infarct border zone, a process called infarct expansion [14]. As the scar matures, the collagen fibers undergo significant cross-linking to increase the tensile strength of the infarct scar to minimize further infarct expansion. [40]. Taken together, the constantly changing mechanical environment and its interplay with cyclic stretching during LV contraction contribute significantly to the development of the infarct scar and remodeling outcomes.

In the long term, the combination of a stiff scar and reductions in functional elastin leads to significant reduction in the elasticity of the infarcted regions, contributing to chamber dilation and wall thinning [20,41]. Chamber dilation and wall thinning of the infarcted regions [42] contribute to increased wall stress and afterload on the heart [21]. As governed by the force-velocity relationship, the resulting increase in afterload decreases the velocity of myocardial fiber shortening. Given a constant ejection period, this response leads to a decrease in stroke volume and cardiac output, thus reducing blood pressure. Baroreceptors in both the aortic arch and carotid artery detect this decrease in blood pressure and incite a sympathetic response. The subsequent release of norepinephrine either directly or indirectly leads to myocardial hypertrophy. Ju *et al.* discovered that in rat hearts, norepinephrine induces myocardial hypertrophy through the $G_{q\alpha}$-signaling pathway [43]. Higher expression levels of $G_{q\alpha}$ protein were detected in regions along the infarct border than in healthier regions away from the infarct to minimize the extent of wall thinning, suggesting that cardiac remodeling behaves in a spatial dependent manner. Additionally, high norepinephrine levels in the plasma indirectly induce hypertrophy by activating the release of renin from the juxtaglomerular apparatus in the kidneys [21]. This leads to increases in endothelin-1 and angiotensin II (AngII) in the renin-angiotensin-aldosterone system (RAAS), triggering a series of biochemical cascades which increases sarcomere count in the cardiomyocytes and contributes to hypertrophy [44]. Another widely accepted mechanism for hypertrophy is mechanical stretch. Gerdes *et al.* discovered that the length of ischemic cardiomyocytes is significantly longer than that of healthy, more elliptical cardiomyocytes [5,24]. This increases mechanical stretching, which enhance the local release of AngII to induce hypertrophy [45].

The pathways described here only represent some of the most widely accepted mechanisms behind cardiac remodeling. To help recapitulate the major pathways that play pivotal roles in cardiac remodeling, from the beginning of ischemia to LV dilation and hypertrophy of the remote cardiomyocytes, a summary of the complex cardiac remodeling process is presented in **Fig. 2.1**. It

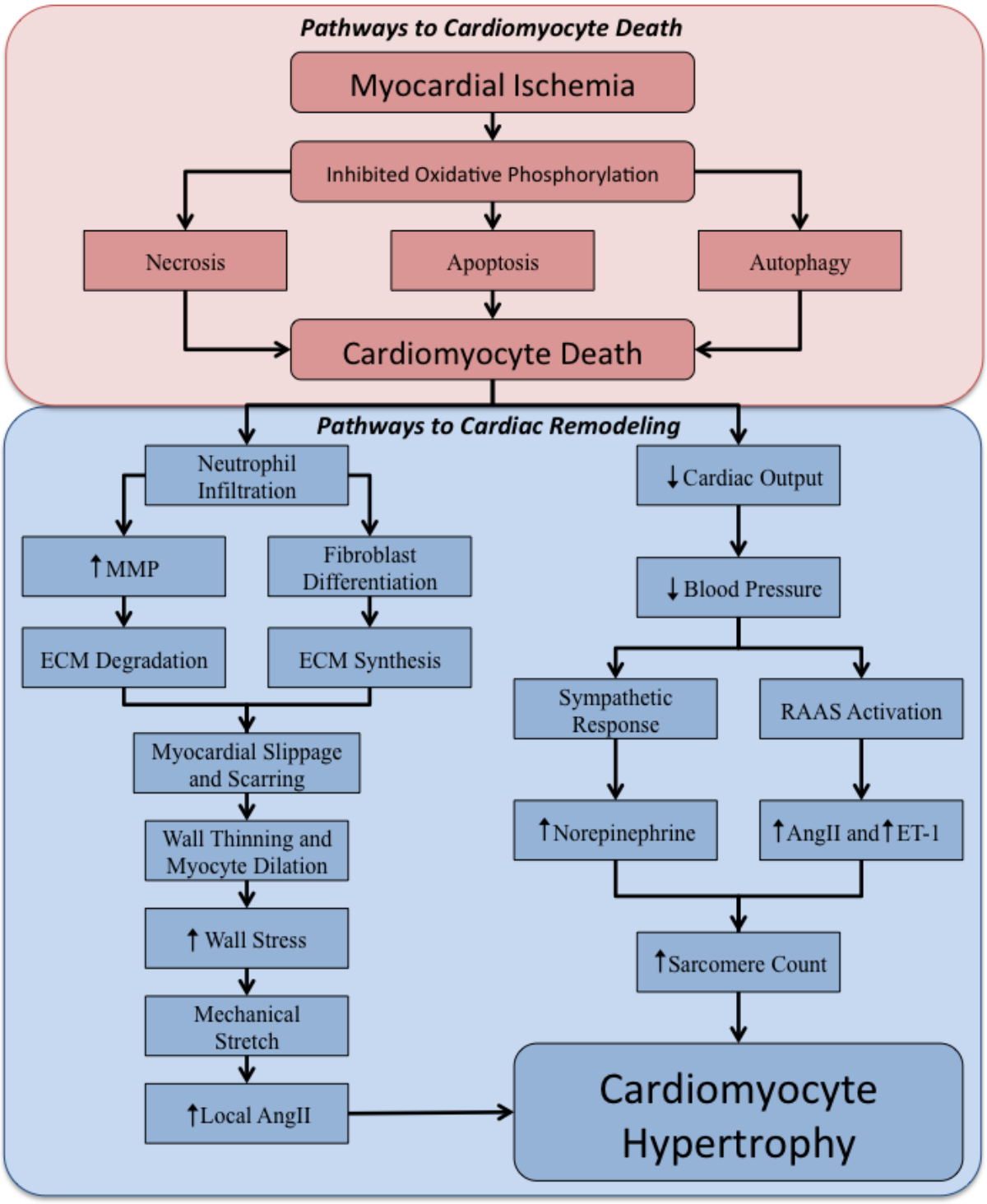

Fig. 2.1: A summary of the series of events behind cardiac remodeling, from ischemia initiation to hypertrophy. ECM: extracellular matrix; RAAS: renin-angiotensin aldosterone system in the renal juxtaglomerular apparatus; AngII: Angiotensin II; ET-1: Endothelin-1.

is beneficial to conceptualize cardiac remodeling as an ongoing reparative process aimed to sustain healthy heart function following a myocardial injury. To compensate for an increased afterload due to the presence of necrotic tissues, the heart hypertrophies to help distribute the load evenly and to maintain a constant stroke volume. Cardiac remodeling continues to transpire until an optimal balance between the loading conditions on the chamber wall and cardiac output is established. Failure to achieve this optimal balance, common in patients with large infarcts, results in a continuous remodeling process that eventually leads to heart failure.

2.2 Noninvasive Approaches to Assess Cardiac Remodeling in Murine Models

Researchers primarily study the complex molecular pathways behind cardiac remodeling through histological staining, genetic manipulations, or proteomics analysis of the dissected hearts. These approaches, however, do not elucidate the progressive cardiac remodeling process or take into account for animal-specific remodeling patterns as they rely on terminal procedures. Furthermore, pathological assessments of infarcts have significant variability and is limited in its ability to quantify regional differences as they often rely on whole organ samples to quantify proteomics. As a result, researchers rely on non-invasive imaging modalities to evaluate cardiac health following an ischemic event. Integrating murine models of myocardial infarction with serial imaging of the heart provides researchers with the necessary tools to visualize and study the progression of cardiac remodeling from the initiation of ischemia to the end stage of heart failure. The majority of research on cardiac remodeling, however, primarily focuses on LV remodeling. In this section, we discuss common imaging techniques, predominantly those involving echocardiography and cardiac MRI, used to assess cardiac remodeling. In the next section, we will delve into greater depth and discuss the role of strain in cardiac remodeling.

2.2.1 Echocardiography

In both clinic and research settings, echocardiography is the most popular imaging modality used for the assessment of cardiac health. Because different tissues have their own unique acoustic properties, echocardiography provides the necessary structural information needed to obtain heart measurements. Its high spatiotemporal resolution and fast acquisition time make it possible to quickly acquire movies of a beating heart. This helps researchers pinpoint the location

of necrotic tissues, identify asymmetry in myocardial wall thickness, and detect any discrepancies in myocardial contractility.

Conventional echocardiographic evaluation of cardiac function typically involves the quantification of LV dimensions during end-diastole and peak-systole from several representative views [4]. Although echocardiography has been used for decades to assess cardiac function in both large and small animals, Gao *et al.* conducted the first serial echocardiographic study of post-infarct LV remodeling in mice [46]. In their experiment, they induced myocardial infarctions in mice by ligating their left coronary artery (LCA; mistakenly referred to as the left anterior descending coronary artery in mice) and monitored for LV remodeling at 1, 2.5, 6, and 9 weeks post-surgery. Gao *et al.* discovered that even though there were only modest increases in LV diameters within 1 week, significant dilation was not observed until 2.5 weeks post-surgery [46]. This suggests that the initial remodeling process is distinct from late-stage remodeling and may play a pivotal role in minimizing infarct expansion and dilation of the LV.

Other more recent studies have utilized new parameters to more accurately capture the cardiac remodeling process. For example, Schaefer *et al.* proposed a parameter, the Tei index, which estimated LV global dysfunction and observed its progressive increase following a myocardial infarction [47]. Software integration of volume measuring techniques, such as the Teicholz method [48] and Simpson's rule [49], using 2D slices of the heart has also simplified the quantification of LV lumen and myocardial wall volume, and hence the assessment of ejection fraction (EF) and myocardial wall thickening. Benavides-Vallve *et al.* showed, using echocardiography, that cardiac remodeling following LCA ligation in mice was associated with progressive dilation and LV wall thickening in the remote regions, which can be clearly visualized in both the parasternal short-axis (top) and long-axis views (bottom) of the LV **Fig. 2.2** [50]. Furthermore, the infarcts were localized to the LV apex through the presence of thin, non-contracting scar tissues in the parasternal long axis view of the heart. Over time, as the LV progressively dilates, the geometry of the LV becomes more spherical. Taken together, these geometrical changes led to significant decreases in ejection fraction (EF = 67% at day 0 vs. 45% at day 90). Benavides-Vallve *et al.* also discovered a negative correlation between infarct size and EF, as mice with large infarctions and myocardial scarring experienced a greater decrease in EF.

In addition to LV geometrical measurements, infarct size is an important parameter to consider when studying cardiac remodeling. The evaluation of infarct size using ultrasound

primarily relies on the detection of wall motion abnormalities and wall thinning [51]. Infarcted tissues or myocardial scars are tissues that have undergone fibrosis and are high in collagen content [40]; consequently, they are stiffer and exhibit reduced contractility [52]. Van Melle *et al.* used tissue Doppler imaging to identify hypodynamic LV wall regions and contractility for the assessment of infarct size [53]. Myocardial contrast echocardiography (MCE) is another potential imaging technique in quantifying not only infarct size, but also myocardial areas at risk for infarct expansion [54,55]. MCE, used to study myocardial circulation, bursts intravenously injected gas-filled microbubbles with high-energy ultrasound and then measures the rate of microbubble replenishment [56,57]. The rate of replenishment, a measure of tissue perfusion, approximates mean blood flow; a slow replenishment rate indicates decreased blood flow to the region, which can be used to detect infarction sites [57].

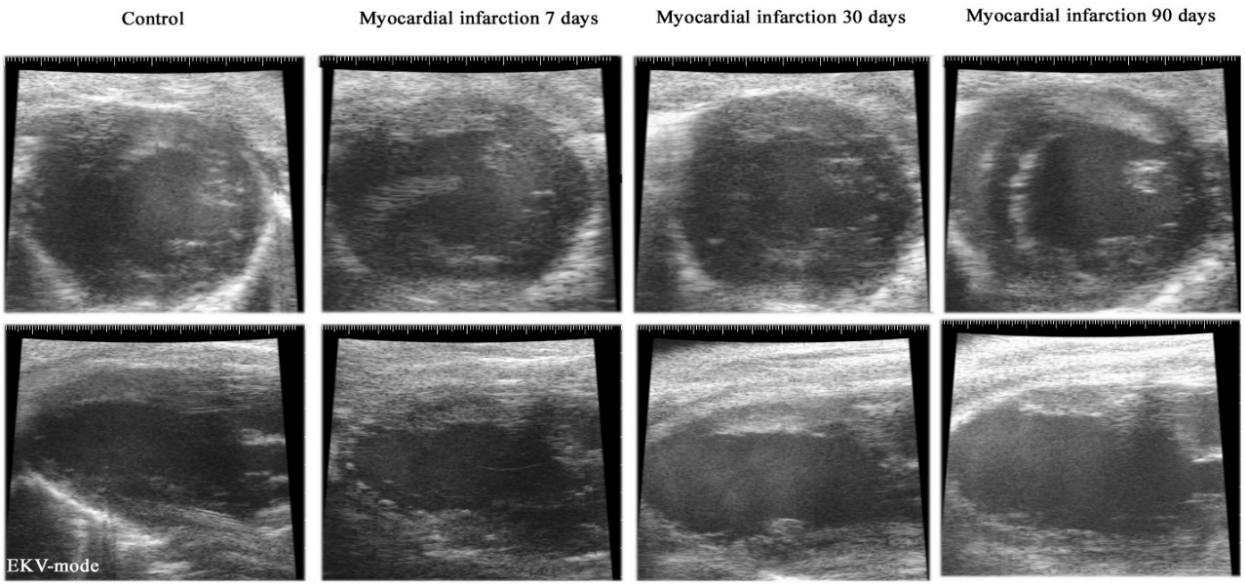

Fig. 2.2: Representative echocardiography images of mouse LVs acquired at baseline and on days 7, 30, and 90 post-surgery. **(Top)** Parasternal short-axis views. **(Bottom)** Parasternal long-axis views. Infarcts are localized to the apex of the LV. Over time, cardiac remodeling leads to LV dilation and wall thickening. Figure adapeted from Benavides-Vallve *et al*. [50].

2.2.2 Cardiac MRI

Similar to echocardiography, cardiac MRI assessment of LV function relies primarily on the quantification of LV dimensions. However, unlike ultrasound, MRI requires an expensive imaging system and is associated with long acquisition times, making it a less popular cardiac

imaging modality than ultrasound. MRI, when used in combination with gadolinium contrast agent, enhances boundary detection, improving the accuracy of LV measurements [58]. Gray *et al.* and Nahrendorf *et al.* conducted MRI serial studies of LV remodeling following LCA ligation in mice and rats respectively and showed that, while LV volumes increased significantly following myocardial infarction, ejection fraction decreased significantly. These results are consistent with observations obtained from echocardiography, although the degree of percent change tends to be slightly higher in data recorded from ultrasound than that obtained from MRI. **Fig. 2.3A** depicts several representative short-axis MR images of a mouse LV, taken using a gadolinium contrast agent, following coronary artery ligation; these images show progressive LV dilation, consistent with literature [58]. 3D renderings of the LV, taken at baseline **(Fig. 2.3B)** and at the end of the study **(Fig. 2.3C)**, reconfirm LV dilation and show the myocardial infarct site at the LV apex.

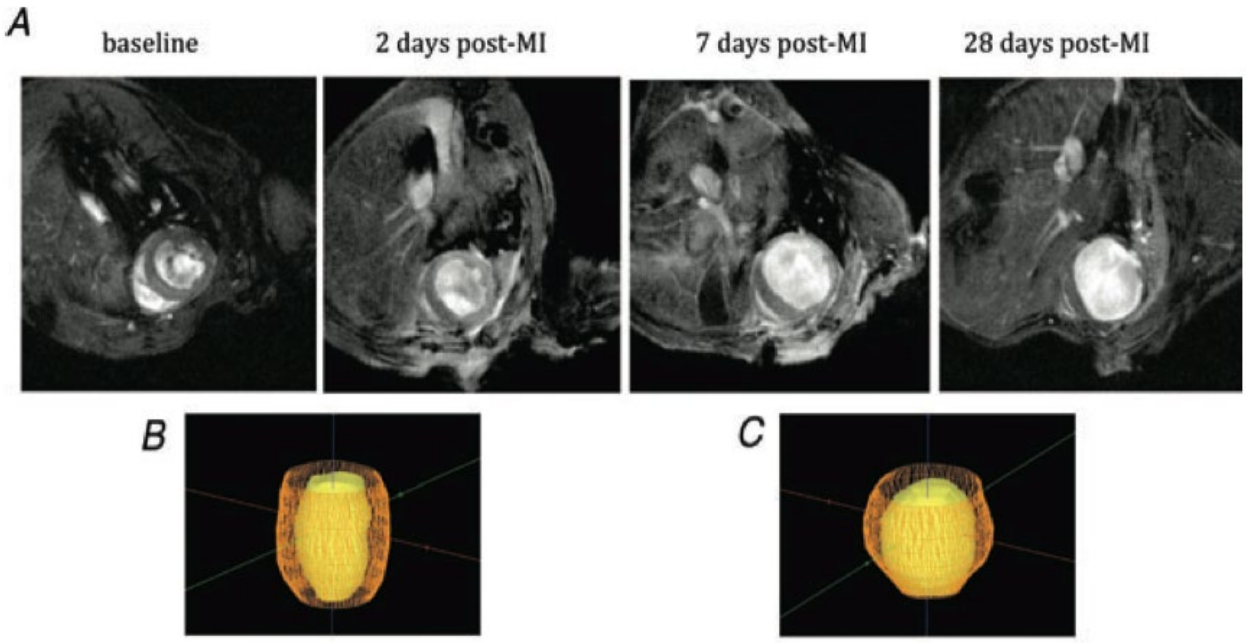

Fig. 2.3: (A) Representative short-axis MR images of a mouse LV, taken with a gadolinium contrast agent at baseline and on days 2, 7, and 28 post-infarction. 3D renderings of **(B)** a healthy and **(C)** a dilated LV taken at 28 days post-surgery show infarct location at the apex. Figure adapted from Gray *et al.* [58].

2.2.3 CT, SPECT, and PET

Other imaging modalities, such as computed tomography (CT) [59], single-photon emission computed tomography (SPECT) [60,61], and positron emission tomography (PET) [62]

are rarely used to study cardiac remodeling due to their dependence on either ionizing radiation or radioactive contrast agents. While Vrachimis *et al.* utilized microSPECT/CT to study myocardial perfusion and identify infract size in mice, Liu *et al.* employed a high-resolution SPECT system to study LV function in mice. SPECT/CT, with its ability to obtain structural details, can detect abnormalities in LV contractility following an infarction [59]. However, unlike SPECT or CT, the use of PET imaging is strictly limited to the identification of infarcted tissues. Since PET is a functional imaging technique that measures changes in metabolic activity and since infarcted tissues are characterized by its lack of metabolic activity, radionuclide tracers can be used to quantify infarct size. Stegger *et al*. and Greco *et al*. introduced a radioactive-labeled glucose derivative, ^{18}F-FDG, into mice that have undergone LCA ligation to differentiate between healthy and infarcted tissues and to quantify for infarct size.

2.3 The Role of Strain in Cardiac Remodeling

As mentioned previously, the time course, mechanical properties, and size of the myocardial scar determine LV remodeling outcomes post-infarction. Although global metrics of LV function are important in studying post-infarction remodeling, these metrics are simply manifestations of the remodeling process and are not predictive tools that can be used early on to predict LV remodeling outcomes. The ability to stratify MI patients based on their estimated risk of developing heart failure may allow physicians to better tailor treatment regimens. Furthermore, many patients who develop heart failure post-infarction have preserved ejection fraction, indicating the need for a better quantitative metric [63]. Because of the well-known role of infarct expansion on LV remodeling [52,58,64], better understanding the role of mechanics in infarct expansion may provide insights into a novel metric for the prediction of remodeling outcomes.

Myocardial strain, often measured as Lagrangian strain instead of Eularian strain, is a dimensionless measure of deformation. It is expressed as the fractional dimensional change that a region of the myocardium endures relative to its original dimension throughout a cardiac cycle [65]. In the clinic, Lagrangian strain (ε) is commonly defined using a linear definition **(Eq. 2.1)**,

$$\varepsilon = \frac{L - L_0}{L_0} = \frac{\Delta L}{L_0} \tag{2.1}$$

where L is the deformed instantaneous length, and L_o is the undeformed reference length. This linear approximation, however, does not consider the nonlinear components of strain and is only appropriate when estimating small deformations less than 5% [66]. This is not the case in many soft tissues, such as the heart, where large deformations are observed *in vivo*. It is also important to realize that during contraction, the LV undergoes rotational twisting to pump blood effectively [67]. Therefore, to accurately describe the regional deformation that the LV undergoes throughout a cardiac cycle, several quantitative parameters of strain needs to be defined. Myocardial strain can be divided into its 6 principal components: 3 components of normal strain (longitudinal, circumferential, and radial) and 3 components of shear strain (circumferential-longitudinal, circumferential-radial, and longitudinal-radial) **(Fig. 2.4)** [68]. The circumferential-longitudinal shear strain (ε_{xy}) is often used to evaluate for torsion or twisting of the LV. Strain rate is another parameter often used to study LV deformation and is defined as the speed at which deformation occurs; it is simply calculated by taking the derivative of strain with respect to time.

Both myocardial strain and strain rate are powerful tools used to study the effects of myocardial scarring on LV function. Since infarcted tissues are comprised primarily of collagen and necrotic cells [40], they can be identified as regions with reduced contractility and strain. The strength of myocardial strain, however, lies in its ability to quantitatively characterize wall motion at the interface between healthy and infarcted myocardium. Regions immediately adjacent to an infarct site are of particular interest in the study of infarct expansion. The criteria for infarct propagation remain unclear to this day. What factors determine how far an infarct will expand? What factors regulate the rate of infarct expansion? These are some of the questions that remain unanswered. Strain characterization of regions neighboring an expanding and isolated infarct site may help elucidate the answers to these questions. Even though 2D myocardial strain has been used to study the effects of myocardial infarction on LV function [65,69], a progressive study of 3D myocardial strain analyzing the extent of infarct expansion following ischemia has yet to be conducted. This is partly due to concerns regarding the reliability and reproducibility of image-based strain analysis techniques, which are still limited to 2D. Here, we present a review of existing algorithms commonly used to quantify myocardial strain.

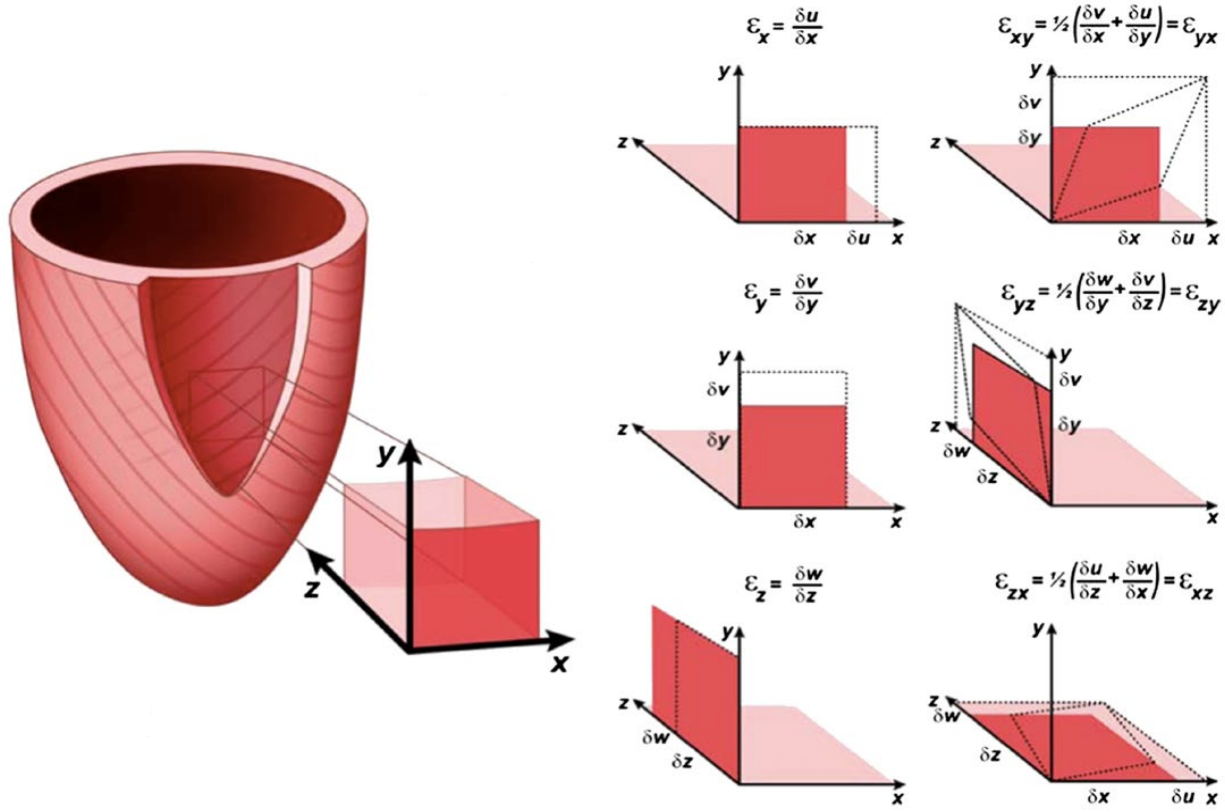

Fig. 2.4: Visual representations of the 6 components of strain required to quantify the contraction and torsion of the LV. In the small cubic sample of myocardial tissue, the x- and y-axes are oriented tangentially to the myocardial wall in the circumferential direction and longitudinal direction, respectively, while the z-axis is oriented radially. The 3 components of normal strain (ε_x, ε_y, and ε_z) correspond to circumferential, longitudinal, and radial strain, respectively. The 3 components of shear strain (ε_{xy}, ε_{yz}, ε_{zx}) correspond to circumferential-longitudinal, circumferential-radial, and longitudinal-radial shear strain, respectively. *u*, *v*, and *w* represent displacement in the x, y, and z directions, respectively. Figure adapted from Geyer *et al*. [68].

2.3.1 Echocardiography Strain Imaging

Doppler strain imaging, commonly called tissue Doppler imaging (TDI), is one of the first ultrasound imaging techniques used to study myocardial strain. In TDI, instantaneous myocardial tissue velocities are acquired using the Doppler effect [65,70]. The strain rate (SR) can then be calculated by taking the spatial velocity gradient, as follows:

$$SR = \frac{V_2 - V_1}{d} \quad \textbf{(2.2)}$$

where V_1 and V_2 correspond to the instantaneous velocities at two different spatial positions and d is the distance between them [71,72]. Finally, by taking the integral of SR with respect to time, Eulerian strain (ε_n) can be obtained as shown in **Eq. 2.3**.

$$\varepsilon_n = \int_{t_o}^{t} SR \, dt \tag{2.3}$$

Here, t_o and t corresponds to the initial and ending time point, respectively [71]. Although TDI has been used in myocardial infarction studies to demonstrate reduced strain [73], SR [74], myocardial velocity gradient [75], and peak-systolic velocities in infarcted tissues and its immediate surroundings [76], TDI has faced severe criticisms due to its limitations. TDI only allows for linear strain measurements along the axis of ultrasound propagation, whereas 6 parameters of strains are needed to accurately capture LV deformation [71]. Furthermore, TDI velocity measurements are angle dependent, which can have significant repercussions on the calculation of strain [68]. These limitations severely limit the robustness of the strain measurements as they introduce significant noise to the final measurement, making TDI an archaic technique.

More recently, echocardiographic strain algorithms are based on speckle-tracking, an image processing technique that monitors the motion of the heart by tracing inherently existing speckle patterns of the myocardium over a cardiac cycle [77]. These patterns, byproducts of both acoustic reflections and interference arrays, are unique at different locations within the myocardium and can be considered as myocardial "fingerprints" [68]. Displacement vectors for specific regions of the myocardium can be acquired by using cross correlation techniques to track the change in the spatial positions of selected speckle patterns, frame-by-frame, across the cardiac cycle. These displacement vectors can then be transformed into velocity vectors by considering the temporal resolution between consecutive frames. Finally, both the displacement and velocity vectors can be used to estimate Lagrangian strain and SR [68]. Unlike DSI, speckle-tracking is an angle-independent technique that measures 2D deformation, making it a more robust technique capable of quantifying longitudinal, circumferential, and radial strain [71].

Algorithms for tracking speckle patterns continue to be a primary area of research in this field. Currently available speckle-tracking techniques can be divided into two different chains of thought: *a posteriori* and *a priori* algorithms [78]. *A posteriori* algorithms depend on prior observations and assumptions of cardiac motion. For example, Wang *et al.* developed a speckle-tracking framework using previous knowledge of image boundaries and motion statistics [79].

Papademetris *et al.*, similarly, relied on segmenting myocardial boundaries to estimate motion fields using a transverse isotropic linear elastic model [80,81]. On the contrary, *a priori* algorithms do not make assumptions regarding the motion field. One of the most popular techniques used for speckle tracking involves intensity-based, nonrigid registration of ultrasound images using B-spline transformation [82,83]. In this approach, a series of cost functions are used to iteratively search for an optimal deformation field which transforms an image from one time point to its next. Other popular tracking algorithms rely on correlation-based optical flow techniques to track motion of the myocardial wall [84-86].

Extensive infarction studies using speckle-tracking algorithms have been conducted with results confirming reduced strain, SR, peak-myocardial velocity, and contractility in the infarcted regions [77,87,88]. **Fig. 2.5** shows representative displacement fields obtained with speckle tracking and overlaid onto ultrasound short-axis and long-axis views of an infarcted mouse heart. The gradual decrease in displacement field magnitudes from regions of healthy myocardium to infarcted regions suggest that strain may be a function of distance from the point of infarction.

Despite the advantages of speckle tracking algorithms, these techniques are still primarily implemented in 2D. As the heart undergoes 3D twisting and torsion during contraction, there are concerns regarding the speckle patterns being tracked. Given a fixed 2D imaging plane, the speckle

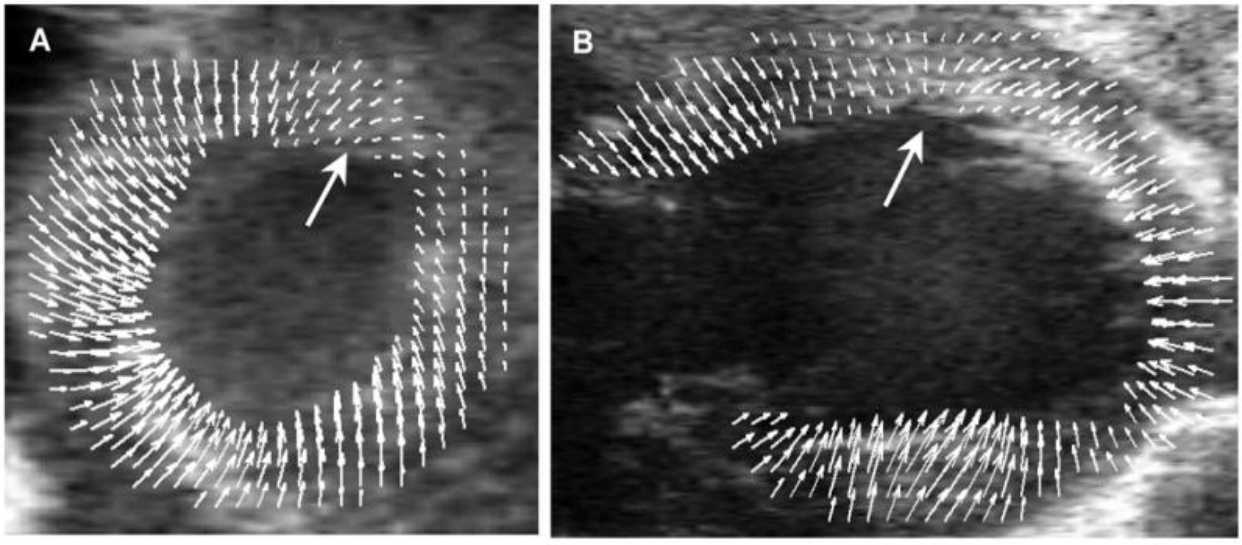

Fig. 2.5: Displacement fields of an infracted mouse heart shown in both **(A)** the short-axis and **(B)** long-axis views. The large white arrows point to the infarction site. Length of the small white arrows is directly proportional to the magnitude of the displacement field. Figure adapted from Li *et al*. [89].

patterns between successive frames used to estimate displacements are subjected to out-of-plane motion. This introduces noise to the measurements and increases the uncertainty of the measured displacement fields [90]. Furthermore, since strains are estimated from these inherently noisy displacement fields, the propagation of error to the final measurements is a limitation that needs to be considered. Knowing this, the implementation of speckle tracking algorithm in 3D is still very limited due to the lack of high resolution four-dimensional (4D) imaging techniques. A more thorough, in-depth discussion of more sophisticated pre-clinical strain techniques and its application to 4D datasets can be found in **Chapter 5** of this dissertation.

2.3.2 Cardiac MR Strain Imaging

MR myocardial tagging, despite being one of the first techniques of its kind, is currently the gold standard used for the assessment of myocardial strain [91]. In myocardial tagging, a selective radiofrequency pulse is applied, prior to image collection, to produce banded regions of reduced signal intensity that act as markers [92]. Axel and Dougherty then extended this technique to construct gridded regions of tissue markers by developing a pulse sequence called SPAMM (Spatial Modulation of Magnetization) [93]. These tissue markers allow for the tracking of myocardial wall motion during contraction. Specifically, the deformation of the tagged grids can be used to obtain displacement fields of the tissue, which is necessary for strain quantification. Epstein *et al.* demonstrated how myocardial tagging could be used to study strain in an infarcted rat's heart **(Fig. 2.6)** [94]. Myocardial tagging of a cross section of the LV indicated that infarcted tissues, which could be seen as a bright signal on the myocardium following gadolinium contrast enhancement **(Fig. 2.6B)** [95], aligned with regions of reduced circumferential shortening, as shown in red in **Fig. 2.6F**. Extensive studies of the effects of myocardial ischemia on LV regional performance using myocardial tagging have been performed with results confirming reduced contractility and strain at infarcted regions and its immediate surroundings [96-98].

2.4 Conclusion

In this review, we have discussed in detail the complex remodeling that transpires in the LV following an MI. Briefly, ischemia-induced necrosis leads to a strong inflammatory response that significantly alters the mechanical properties of the surrounding ECM. These early changes

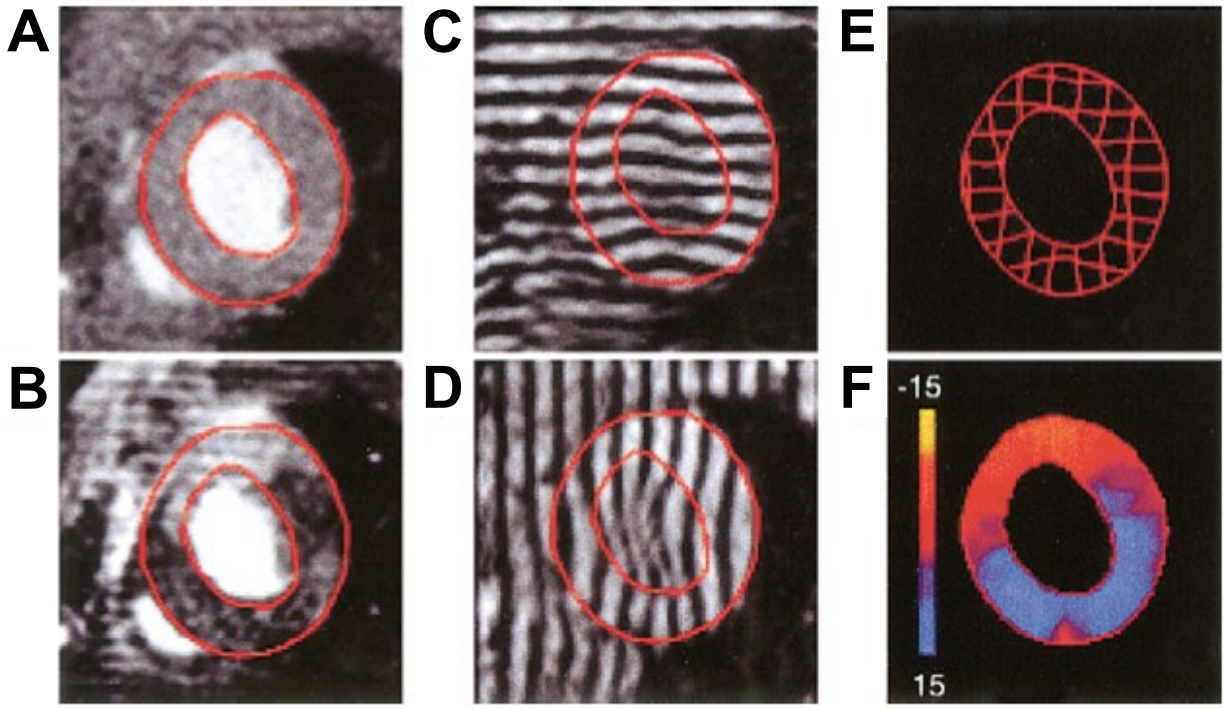

Fig. 2.6: Representative MR images of an infarcted rat LV. **(A)** before and **(B)** after Gd-DTPA contrast enhancement. **(C,D)** Myocardial-tagged images. **(E)** A grid map showing the locations of myocardial tags. **(F)** A map of the percent circumferential shortening reveals impaired contractility in infarcted regions. Figure adapted from Epstein et *al.* [94].

in tissue stiffness, in combination with cyclic stretching at infarct border zones, regulate fibrotic scar formation. Meanwhile, infarct expansion continues to occur until significant collagen cross-linking provides the scar with the increased tensile strength necessary to inhibit further expansion. Taken together, it is evident that myocardial mechanics contribute to final infarct size, which is strongly correlated with remodeling outcomes. Despite these findings, the majority of infarction studies still focus on the global analysis of LV function using traditional planar techniques. Although *in vivo* studies of myocardial mechanics are increasing in popularity, they are still limited to 2D, making it unsuitable when studying the LV that undergoes 3D torsion and twisting. With this in mind, the following chapter **(Chapter 3)** provides an in-depth research plan to overcome the challenges that inhibit the 3D evaluation of *in vivo* strain.

3. RESEARCH PLAN

In this chapter, we will reflect on the research tools discussed previously and propose a plan to overcome the hurdles associated with the assessment of 3D strain. Specifically, this chapter begins with a discussion on the limitations of existing *in vitro* and *in vivo* techniques used to study the role of mechanics in post-infarction remodeling. This is followed by an in-depth research plan that, upon its completion, enables researchers to thoroughly characterize spatial changes in 3D myocardial strain throughout LV remodeling. The three research objectives presented within the research plan will be the basis for the work presented in **Chapters 4-6**.

3.1 Limitations of Existing MI Studies

Studies investigating the molecular and cellular mechanisms behind infarct healing primarily rely on *in vitro* cell work to study how gene expression levels are altered following ischemia and mechanical strain [99,100]. They are often accompanied by proteomics, histological, or *ex vivo* mechanical analysis of the infarcted LVs to correlate how changes in gene expression lead to tissue remodeling [101]. Although these studies are important in elucidating the mechanisms underlying post-infarction remodeling, several key limitations exist. Reproducing physiological mechanical conditions *in vitro* is challenging, even with recent advances in engineered 3D tissue scaffolds [102]. This hurdle makes it difficult to directly investigate how mechanical changes on the tissue level contribute to the remodeling process *in vivo*. These studies also cannot be used to assess regional differences in LV mechanics important in the investigation of infarct expansion. Lastly, there are significant variations in remodeling outcomes *in vivo*, even within the same surgical animal model, stressing the importance of monitoring animal-specific remodeling patterns throughout disease progression.

To overcome the limitations associated with *in vitro* experiments and to better understand how fibrotic scar development impacts overall remodeling, there is increasing interest in using *in vivo* imaging techniques to monitor disease progression. The majority of longitudinal imaging studies, however, still rely on 2D techniques to quantify LV volumes and function. These analyses require the use of geometrical assumptions, which are inappropriate when evaluating diseased LVs. For example, fibrotic scars often develop asymmetrically in the remodeling LVs [89,103].

Applying a geometrical fit to these complex shaped hearts will lead to either underestimation or overestimation of global LV parameters, depending on the plane in which the 2D image is acquired [104]. Additionally, while these parameters are helpful in monitoring progressive wall thinning and LV dilation, they are simply clinical manifestations of cardiac remodeling; therefore, their use as early predictive tools in identifying patients who are at high risk of developing heart failures is limited. Recent advancements in image processing have opened the door for *in vivo* strain analysis of image data, but these techniques are still limited to 2D largely due to the lack of 4D imaging technologies. As mentioned previously, 2D strain analysis yields noisy results due to out-of-plane motion [90] and is not ideal for characterizing the mechanics of an organ that undergoes significant 3D deformations. Therefore, improvements in image acquisition and strain analysis techniques are necessary to better characterize the role of mechanics on LV remodeling.

3.2 Research Plan

The development of a noninvasive 4D imaging technique will address many of the limitations mentioned in the previous section. First, the ability to acquire 4D cardiac data with high spatiotemporal resolution will significantly improve the global assessment of LV function. Since volumetric data across the cardiac cycle are acquired, subject-specific LV geometries can be modeled in 3D to directly quantify LV volumes and function without the need for geometrical assumptions. These 3D models can then be used to accurately track structural changes in the LV, such as wall thinning and chamber dilation, throughout post-infarction remodeling. Importantly, we can utilize these 4D data to develop, test, and validate a reliable 3D strain algorithm, which will eliminate issues attributed to out-of-plane motion. Taken together, incorporating 4D imaging and 3D strain analysis with a longitudinal MI study will provide invaluable information regarding the role of myocardial mechanics on LV remodeling post-infarction. To achieve these goals, we will need to use animal models of acute MI and complete the following objectives.

3.2.1 Animal Models of MI

We will utilize surgical mouse models of acute MIs for the proposed research. Although these models do not experience the gradual series of events leading up to a heart attack, mice respond similarly to ischemic injury and undergo many of the same cardiac remodeling steps as

humans [14]. One notable difference is that mice undergo an accelerated remodeling timeline compared to humans, making them ideal for the study of long-term remodeling to heart failure [14]. Specifically, we will use the permanent ligation (PL) and the more clinically relevant ischemia/reperfusion (I/R) models in this dissertation. As the name suggests, in the PL model, the left coronary artery (LCA) will be permanently ligated with a suture to induce a large transmural apical infarct. On the contrary, the LCA will be temporarily ligated for 30-minutes in the I/R model. This procedure mimics the reperfusion effects of balloon angioplasty or stent deployment often used in the clinic to minimize myocardial tissue damage. By utilizing two MI models with varying ischemia severities, we can investigate if there are significant differences in LV mechanics early in remodeling that contribute to final infarct size.

3.2.2 Objective 1: 4D Ultrasound Development

Develop a gated, volumetric ultrasound imaging technique to acquire 4D cardiac data with high spatiotemporal resolution. *Rationale:* To extend longitudinal 2D strain studies to 3D and to directly evaluate global LV parameters without the need for geometrical assumptions, we first need to develop a noninvasive imaging technique capable of capturing volumetric data over time (4D). In order to reliably estimate strain fields within subregions of the 4D data, however, an imaging modality that can provide high spatial resolution data is necessary. We decided to use ultrasound for the proposed study because of its superior spatial resolutions, faster acquisition times, and lower costs when compared to MRI [105]. *Approach:* We propose to reconstruct 4D data by acquiring successive cardiac and respiratory gated 2D cine loops of the entire LV. Respiration gating will be implemented to eliminate breathing artifacts, while ECG gating will be used to temporally match successive 2D images across the entire cardiac cycle. Finally, image registration will be performed to reconstruct the 4D data. *Hypothesis:* To demonstrate that 4D ultrasound improves the assessment of cardiovascular health, we will compare the measured global LV parameters to those estimated using gold-standard 3D MRI and conventional 2D techniques, for both healthy and infarcted mouse LVs. We hypothesize that direct 4D analysis will result in more accurate and reproducible assessments of LV function when compared to standard 2D techniques, especially when analyzing infarcted LVs. A thorough study based on this objective is presented in **Chapter 4**.

3.2.3 Objective 2: Optimize a Reliable 3D Strain Algorithm

Optimize a reliable 3D strain algorithm to characterize 3D myocardial strain from 4D ultrasound data. *Rationale:* Clinically available 2D strain algorithms rely on linear definitions of strain that are only appropriate when analyzing small deformations less than 5%, which is not the case for the LV. However, more sophisticated 2D speckle tracking algorithms are susceptible to out-of-plane motion and suffer from the well-known challenge of taking numerical gradients of noisy displacement fields, leading to significant error propagation in the final strain calculation. Although the acquisition of 4D data will resolve issues related to out-of-plane motion, we still need to extend existing 2D strain algorithms to 3D and rely on strain methods that do not require the initial calculation of displacement fields to estimate strain. *Approach:* Through a collaborative effort with researchers from Washington University in Saint Louis and Columbia University, we expanded upon a previously published 2D direct deformation estimation (DDE) strain algorithm [106] to 3D. This DDE approach estimates deformation gradient fields directly during voxel intensity mapping by utilizing a novel warping function to map target regions in the reference image to its deformed image; this circumvents the need to estimate strain from noisy displacement fields. *Hypothesis:* We hypothesize that the extension of a DDE strain method to 3D will result in a reliable strain algorithm that is noise-insensitive and yields more accurate results than conventional displacement-based methods. To test for this hypothesis, we plan to compare the performance of this algorithm to other state of the art techniques *in silico* before implementing it to 4D cardiac ultrasound data to characterize 3D myocardial strain. A thorough study based on this objective is presented in **Chapter 5**.

3.2.4 Objective 3: Longitudinal MI Strain Study

Conduct a thorough longitudinal 3D strain study using surgical mouse models of MIs and correlate results with histology. *Rationale:* We have emphasized multiple times throughout this dissertation that the evolving mechanical properties of the infarcted myocardium and its surrounding environment help regulate the formation of fibrotic scars and may play a role in infarct expansion. Therefore, we will integrate our 4D ultrasound imaging technique with a 3D-DDE strain algorithm to, for the first time, thoroughly characterize spatial changes in 3D myocardial strain throughout remodeling. *Approach:* We will separate the mice into three different surgical

groups: 1) sham, 2) PL, and 3) I/R surgery. 4D ultrasound data will be collected at baseline and at various time points post-surgery to capture both the early and late stages of cardiac remodeling up to four weeks. We will quantify both global LV function and 3D strain at the different phases of cardiac remodeling to study how regional differences in myocardial contractility contribute to diminished LV function. Topographical strain maps will then be overlaid onto 3D models of the LV to study how strain profiles correlate to structural changes. Strain at infarct border zones will be thoroughly analyzed to see how infarct severity relates to strain. Our strain results will then be compared to infarct sizes measured from ultrasound and histological analysis. *Hypothesis:* Due to the stiff behavior of fibrotic infarct scars, we hypothesize that reductions in 3D myocardial strain is a determinant of final infarct size and correlates with LV remodeling severity. An in-depth study expanding on this objective is presented in **Chapter 6**.

Taken together, we hope that the completion of the three outlined objectives will help elucidate how myocardial mechanics govern post-infarction cardiac remodeling. We are particularly interested in identifying how strain profiles in infarct border zones differs between hearts with stabilized infarcts and those that continue to progress to heart failure. The objective of this dissertation is therefore to investigate the role of myocardial strain in promoting infarct expansion and assess whether it can predict LV remodeling outcomes. Such a tool may help physicians identify patients at risk of developing heart failure so that they may receive early intervention, improving their overall prognosis.

4. THE DEVELOPMENT OF PRE-CLINICAL FOUR-DIMENSIONAL ULTRASOUND FOR SMALL ANIMAL APPLICATIONS

As outlined in the research plan, the first step in quantifying 3D myocardial strain is to develop a noninvasive imaging technique capable of acquiring *in vivo* volumetric information of the LV across a representative cardiac cycle. These four-dimensional (4D) data will allow us to capture out-of-plane motion frequently missed by 2D imaging, thus considering for the 3D twist mechanics of the LV. This chapter highlights our recent efforts in the development of a 4D ultrasound imaging technique for small animal applications. Specifically, we will discuss how prospective gating and image registration can together be used to reconstruct high resolution 4D data and improve the assessment of cardiovascular health. The content presented in this chapter is adapted from our previous work titled "Cardiac and Respiratory-Gated Volumetric Murine Ultrasound," which was published in the *International Journal of Cardiovascular Imaging*. Minor edits to the formatting and wording have been made to produce a cohesive dissertation.

4.1 Abstract

Purpose: Current cardiovascular ultrasound mainly employs planar imaging techniques to assess function and physiology. These techniques rely on geometric assumptions, which are dependent on the imaging plane, susceptible to inter-observer variability, and may be inaccurate when studying complex diseases. Here, we developed a gated volumetric murine ultrasound technique to visualize cardiovascular motion with high spatiotemporal resolution and directly evaluate cardiovascular health. ***Methods:*** Cardiac and respiratory-gated cine loops, acquired at 1000 frames-per-second from sequential positions, were temporally registered to generate a four-dimensional (4D) dataset. We applied this technique to 1) evaluate left ventricular (LV) function from both healthy mice and mice with myocardial infarction and 2) characterize aortic wall strain of angiotensin II-induced dissecting abdominal aortic aneurysms in apolipoprotein E-deficient mice. ***Results:*** Combined imaging and processing times for the 4D technique was approximately 2 to 4 times longer than conventional 2D approaches, but substantially more data is collected with

4D ultrasound and further optimization can be implemented to reduce imaging times. Direct volumetric measurements of 4D cardiac data aligned closely with those obtained from MRI, contrary to conventional methods, which were sensitive to transducer alignment, leading to overestimation or underestimation of estimated LV parameters in infarcted hearts. Green-Lagrange circumferential strain analysis revealed higher strain values proximal and distal to the aneurysm than within the aneurysmal region, consistent with published reports. ***Conclusion:*** By eliminating the need for geometrical assumptions, the presented 4D technique can be used to more accurately evaluate cardiac function and aortic pulsatility. Furthermore, this technique allows for the visualization of regional differences that may be overlooked with conventional 2D approaches.

4.2 Introduction

Cardiovascular disease (CVD) is the leading cause of death in the United States, responsible for 30% of all deaths in 2013 [2]. With CVD expected to affect 40% of the U.S. population by 2030 [107], there is an increasing need to develop improved *in vivo* imaging techniques to better understand the pathophysiology and progression of CVD. Four-dimensional (4D) imaging, also known as gated three-dimensional imaging, has sparked interest in recent years as it delivers a cinematographic representation of three-dimensional structures with high spatiotemporal resolution [108]. The use of time-dependent 3D geometries is becoming more popular as it provides patient-specific boundary conditions for biomechanical modeling and computational fluid dynamic simulations [109]. Recent developments of clinical 4D computed tomography (CT) [110], magnetic resonance imaging (MRI) [111,112], and ultrasound [113,114] have enabled the study of valve leaflet motion [115], 3D myocardial strain [116], and aortic wall kinematics [117], overcoming the limitations of standard 2D and 3D imaging techniques. These traditional imaging methods often fail to adequately identify differences in motion associated with a variety of pathological conditions. As a result, the advantage of 4D imaging stems from its ability to capture a holistic view of tissue motion, making it a method of increasing interest for the study of CVD.

Small animal models have proven useful in studying various CVD mechanisms. In particular, the development of *in vivo* imaging techniques for mouse models have become invaluable for controlled investigations of CVD progression, while simultaneously reducing the necessary number of animals per study [118]. Still, there are notable obstacles unique to

cardiovascular imaging in rodents that make these techniques challenging. The animals' small size, fast respiration, and rapid heart rate – which ranges from 400 to 600 beats per minute [119] – require an imaging modality with spatiotemporal resolution much higher than that used for humans. While volumetric ultrasound probes exist for large animals and clinical use [120], their low spatiotemporal resolution renders them inadequate for imaging small animals. Recent advancements in high-frequency ultrasound probes have overcome limitations in spatiotemporal resolution by providing a sampling rate adequate for rodents, yet these improvements currently only apply to planar imaging. In these regards, post-processing methods are needed to reconstruct and visualize 4D ultrasound data.

Gating using electrocardiogram (ECG) and respiration signals are often performed in tandem with ultrasound imaging to temporally synchronize periodic events and minimize motion artifacts [119,121]. This paradigm creates a foundation to spatiotemporally combine data from multiple acquisitions, which extends to techniques such as 4D MR microscopy and micro-CT [112,122]. However, as the sampling rate is much slower than that of high-frequency ultrasound probes, these techniques are limited to resolving only large-scale heart motion and often require prolonged administration of anesthesia; in the case of micro-CT, ionizing radiation and an intravenous contrast agent are also needed. While high-frequency ultrasound imaging also requires anesthesia and is subject to imaging artifacts, its ability to image in real-time makes it ideal for measuring cardiac function and pulsatile vascular motion in mice [123].

To date, the majority of cardiovascular imaging research in rodent models has utilized conventional 2D ultrasound to evaluate left ventricular (LV) function and characterize aneurysm growth. However, the extension to gated volumetric ultrasound provides several advantages over these planar techniques. In addition to eliminating the need for geometric assumptions, which are necessary with 2D imaging [124], 4D imaging is capable of capturing regional differences in ventricular and arterial motion that may go undetected with planar approaches. Here, we demonstrate a method for acquiring and analyzing 4D ultrasound data in small animal models of CVD and compared the results to standard 2D techniques and MRI. To the best of our knowledge, this is the first published report comparing 4D ultrasound, MRI, and 2D echocardiography in small animals, highlighting the limitations of 2D techniques. The proposed method combines a linearly translating high frequency ultrasound transducer, ECG and respiratory gating, and image post-

processing to reconstruct 4D data for the direct evaluation of LV health and characterization of dissecting abdominal aortic aneurysm (AAA) wall kinematics.

4.3 Materials and Methods

4.3.1 Animals

All mice were purchased from Jackson Laboratories (Bar Harbor, ME, USA) and were divided into three different experimental groups. The first group consisted of 11 male C57BL/6J wild-type mice and was imaged to evaluate LV function in healthy mice. Mice with ages ranging from 21 to 70 weeks were selected to allow for imaging collection from a wide variety of mouse sizes, but our analysis revealed no statistical correlation between animal age and cardiovascular metrics in these adult mice. The second group consisted of 6 male C57BL/6J wild-type mice with varying degrees of myocardial infarctions (MIs) and was imaged four weeks post-MI induction to assess for LV function in remodeled hearts. In preparation for each myocardial infarction surgery, mice were anesthetized with 2% isoflurane, endotracheally intubated, and ventilated with O_2 (SomnoSuite, Kent Scientific, Torrington, CT, USA) [125]. Pneumothorax was avoided by supplying air to the lungs with a target inspiratory pressure between 16-18 cm H_2O and a minimum peak-end expiratory pressure between 3-5 cm H_2O. After performing a left thoracotomy, we permanently ligated the left coronary artery using 8-0 sutures [126,127] and allowed the mouse to recover **(Fig. A.1)**. The third group consisted of 7 male apolipoprotein-E deficient ($apoE^{-/-}$) mice with dissecting AAAs imaged two weeks post-aneurysm formation to characterize aneurysm wall kinematics. To induce an aneurysm, $apoE^{-/-}$ mice were implanted subcutaneously with mini-osmotic pumps (ALZET Model 2004; DURECT Corporation, Cupertino, CA, USA) to systemically deliver 1000 ng/kg/min of angiotensin II (A9525; Sigma-Aldrich, St. Louis, MO, USA) for 28 days [128,129] **(Fig. A.1)**. A summary of the characteristics for the different experimental mouse groups is shown in **Table 4.1**.

4.3.2 Time-Resolved Volumetric Ultrasound Imaging

Cardiac- and respiratory-gated volumetric ultrasound (4D) data was acquired using the Vevo2100 small animal ultrasound system (FUJIFILM VisualSonics Inc., Toronto, Ontario, Canada) and a 40 MHz linear array ultrasound transducer (MS550D) attached to a linearly moving

Table 4.1: Summary of Different Experimental Mouse Groups

Gender	**Male**		
Genotype	**WT**		**apoE$^{-/-}$**
Study	**Cardiac**		**Abdominal Aorta**
Group	**Healthy**	**Infarcted**	**Aneurysm**
n	11	6	7
Age (weeks)	37 ± 20	15 ± 3	19 ± 2
Weight (g)	35 ± 8	29 ± 2	30 ± 1

step motor (3D Acquisition Motor). Before imaging, we anesthetized the mouse with 2-3% isoflurane at 1.5 L/min room air using a low-flow integrated digital anesthetic vaporizer (Somnosuite, Kent Scientific, Torrington, CT, USA). The SomnoSuite more efficiently delivers isoflurane to the animal, which has been shown to effectively minimize heart rate variations during imaging as long as two hours [20]. We removed hair from the region of interest (i.e. the ventral thorax for cardiac imaging or the abdomen for dissecting AAA imaging) using a depilatory cream and applied ophthalmic ointment to the eyes to prevent corneal desiccation. ECG and respiratory signals were continuously acquired by securing the animal's paws to gold-plated leads using an electrode gel while the animal was positioned supine on a heat-modulated imaging stage (Vevo Imaging Station). Respiratory information was obtained by monitoring for low frequency changes in the signal associated with fluctuating electrical impedance during inspiration. We implemented cardiac and respiratory gating by acquiring ultrasound data at successive 1 ms delays between RR peaks and by using a 40% acquisition window in between inhalation peaks. Isoflurane levels were gradually decreased throughout image acquisition to further minimize fluctuations in heart rates. To prevent hypothermia, the animal's body temperature was monitored using a rectal temperature probe, and the temperature of the heated stage was adjusted accordingly. We also used a heating lamp as a secondary source to help maintain body temperature during imaging. On average, setting the temperature of the stage between 40-42°C maintained the animal's body temperature to 36.1±0.6°C, even in experiments as long as 90 min.

Once the respiration rate of the mouse had stabilized, we applied warmed ultrasound gel to the skin and positioned the ultrasound probe at the center of the region of interest, perpendicular to the intended axis of translation. For example, when imaging the LV, short-axis cine loops were

collected with the probe translating along the long-axis of the heart. A custom MATLAB script (MathWorks, Natick, MA, USA) was used to automate the translation of the probe and acquisition of cine data at each sequential location. Step sizes ranging between 80 to 200 μm were used for both cardiac and dissecting AAA acquisitions, depending on the length of the region of interest. Cine loops were acquired at 1000 frames-per-second (fps) using the ECG-gated kilohertz visualization (EKV) module (FUJIFILM VisualSonics Inc.). EKV acquisition utilized both cardiac and respiratory gating to reconstruct ultrasound images over one representative cardiac cycle from data over multiple beats. This is only possible because of similarities between sequential heartbeats. As such, each EKV cine loop consisted of planar snapshots of the region imaged across one representative cardiac cycle with a temporal resolution of approximately 1 ms. The number of frames obtained in an EKV loop was dependent on the animal's heart rate, which remained relatively stable throughout image acquisition. Total acquisition times ranged from 40 to 90 minutes, depending primarily on the length of the scanned region and the defined step size, with each slice taking approximately 30-45 seconds to acquire.

4.3.3 Data Reconstruction

The series of position-dependent EKV cine loops were exported to MATLAB for analysis. Spatially adjacent cine loops were aligned and temporally matched such that each reconstructed volume represents one synchronized time-point in the cardiac cycle. The total number of frames in each successive EKV loop could vary due to heart rate fluctuations. These discrepancies are typically confined to 2-3% of the mean number of frames and were therefore considered negligible. During reconstruction, this was accounted for by removing end-diastolic frames in longer loops before temporally matching the remaining frames. Gaussian filters were applied both spatially and temporally for noise removal; since the voxels were anisotropic, the kernel window used was 10% of the total number of pixels in each spatial dimension, and the Gaussian filter width was chosen relative to a desired isotropic resolution size. Linear interpolation was used to reconstruct isotropic voxels and simplify post-processing analysis: 60 μm for cardiac data and 40 μm for aortic aneurysm data. A smaller voxel size was chosen for the aortic data to better capture the wall boundaries and visualize motion of the stiff dissecting aneurysm. A diagram of the acquisition method is outlined in **Fig. 4.1** using a sample murine cardiac dataset. The MATLAB codes for image acquisition and reconstruction are provided as supplementary materials.

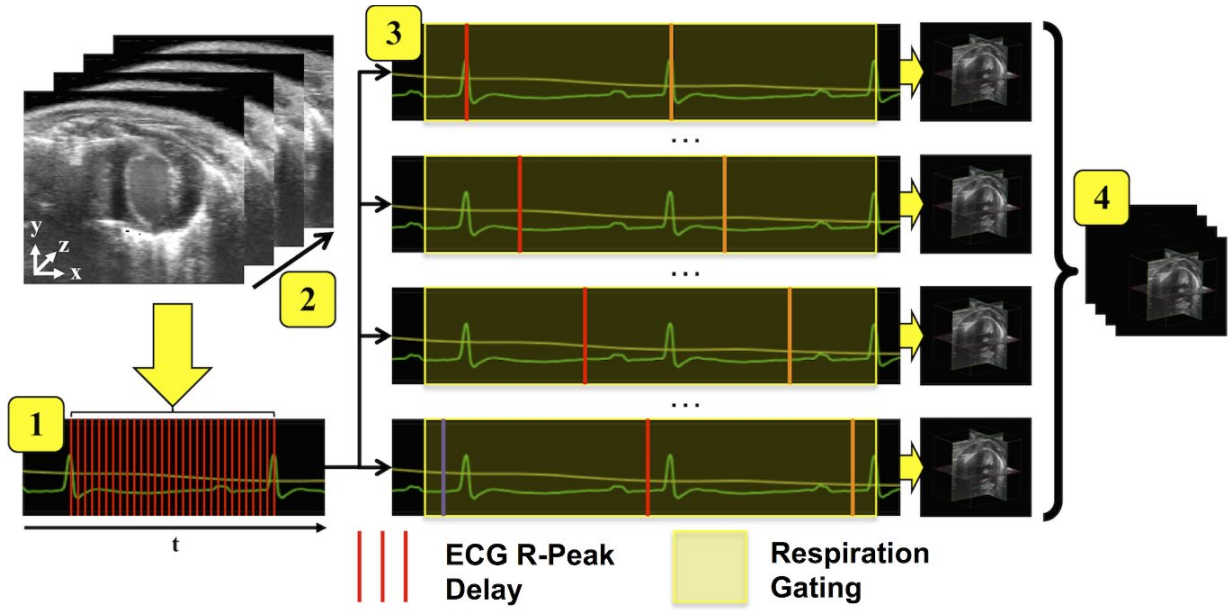

Fig. 4.1: A schematic of the imaging technique from data acquisition to volumetric rendering. The steps include **1)** acquiring respiratory- and ECG-gated 2D cine loops at 1000 fps from a specific location, **2)** translating the ultrasound probe using the attached motor and repeating step one at each location, **3)** combining the extracted frames from each cine loop, dependent on their timing within the cardiac cycles, to create 3D volumes at each respective time-point, and **4)** temporally concatenating said volumes to create 4D datasets.

4.3.4 Analysis of 4D Cardiac Dataset

Manual segmentation was performed on the reconstructed 4D cardiac data to outline the endocardial and epicardial surfaces of the LV, extending from the apex to the mitral and aortic valves at end-diastole and peak-systole. To study the contribution of papillary muscle on lumen volume measurements, two endocardial boundaries were obtained: one with the inclusion and a second with the exclusion, of papillary muscles during segmentation. The segmented boundaries were then used to create 3D representations of the LV at both end-diastole and peak-systole. All volume measurements were converted to physical units by multiplying the number of voxels within the 3D volumes by the physical dimensions of each isotropic voxel. End-diastolic volume (EDV) and peak-systolic volume (PSV) were used to evaluate LV function including stroke volume (SV), ejection fraction (EF), and cardiac output (CO). These measurements were calculated using the following equations **(Eqs. 4.1-4.3)**:

$$SV = EDV - PSV \quad \textbf{(4.1)}$$

$$EF = \frac{SV}{EDV} \text{ x } 100 \quad \textbf{(4.2)}$$

$$CO = SV \text{ x Heart Rate} \quad \textbf{(4.3)}$$

We also calculated LV volumes using two established methods commonly used in the clinic – the Teicholz method **(Eq. 4.4)** and the modified Simpson's rule of discs **(Eq. 4.5)** – and compared them to LV volumes obtained by direct measurements from the reconstructed 4D datasets. As recommended by the guidelines for cardiac chamber quantification provided by the American Society of Echocardiography, the papillary muscles were considered part of the LV cavity when performing endocardial wall tracings [49,130-132].

$$\text{LV Volume}_{\text{Teicholz}} = \frac{7}{(2.4+d_i)} d_i^3 \quad \textbf{(4.4)}$$

$$\text{LV Volume}_{\text{Simpson's}} = \frac{\pi}{4} h \sum d_i^2 \quad \textbf{(4.5)}$$

In **(Eqs. 4.4-4.5)** above, d_i corresponds to the LV internal diameter, and h symbolizes the height of the circular discs.

4.3.5 Analysis of 4D Dissecting AAA Dataset

Similar to the cardiac analysis, the aortic walls of the 4D dissecting AAA datasets were manually segmented at systole and diastole. Branching vessels, including the superior mesenteric artery, celiac artery, and renal arteries were excluded for simplicity. To quantify aortic wall kinematics, maximum Green-Lagrange circumferential cyclic strain ($\varepsilon_{\theta\theta}$) was calculated at each axial location by using the effective systolic (d_S) and diastolic (d_D) diameters calculated from the segmented cross-sectional areas of the abdominal aorta [133]:

$$\varepsilon_{\theta\theta} = \frac{1}{2}\left[\left(\frac{d_S}{d_D}\right)^2 - 1\right] \times 100 \quad \textbf{(4.6)}$$

4.3.6 Magnetic Resonance Imaging

MRI data for infarcted hearts were acquired using the Bruker 7T Biospec 70/30 USR System (Bruker, Billerica, MA, USA) and a small animal volume coil (RF RES 300 1H 075/040 quadrature surface transmit receive coil, Bruker). We anesthetized the mouse with 2-3% isoflurane in room air and acquired ECG, respiration, and temperature data using the MR-Compatible Monitoring and Gating System (SA Instruments, Stony Brook, NY, USA). ECG and respiratory-gated cine fast low angle shot (FLASH) pulse sequence (TE = 3 ms; TR = 7 ms; FA = 20°; Matrix Size = 256 x 256; Number of averages = 1) was used to acquire contiguous 1 mm thick short-axis cine loops of a beating left ventricle.

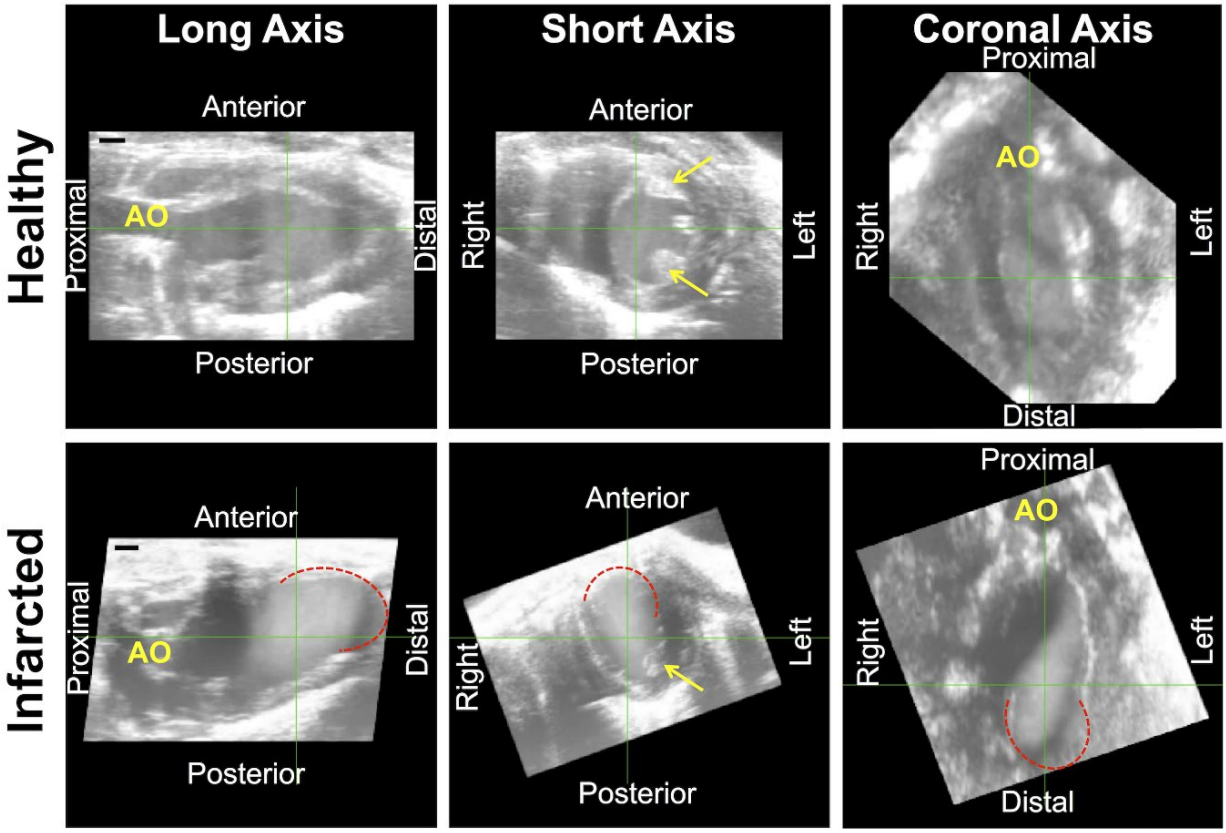

Fig. 4.2: Three axis views of a healthy **(top)** and infarcted **(bottom)** mouse left ventricle taken at end-diastole. Ultrasound images of the infarcted LV were obtained four-weeks post-LAD coronary artery ligation. Papillary muscles are clearly seen in the short-axis view as extensions into the LV lumen (yellow arrows). Infarcted myocardial tissue is outlined in red. Green crosshairs highlight the center of the visualized structure. AO = aortic outflow. Scalebar = 1mm.

4.4 Results

4.4.1 Assessment of Left Ventricular Function

Representative diastolic images of a healthy LV (top) and a LV with a four-week old anterior apical infarct (bottom) are shown in three-axis views in **Fig. 4.2**, with ultrasound and MRI cine loop data shown in **Figs A.2-A.3** respectively. The displayed data were rotated along its anterior-posterior axis to visualize true short-axis and long-axis views of the LV. Due to image registration, volumetric data can be spatially rotated; hence, any planar cut can be extracted to give both conventional (axial and sagittal) and unconventional (coronal) ultrasound views of the heart. Manually segmented 3D renderings of both the endocardial (red) and epicardial (blue) LV walls are illustrated in **Fig. 4.3** for both healthy and infarcted hearts at end-diastole and peak-systole. The asymmetrical anterior apical infarct is associated with wall thinning and dyskinesia of the necrotic myocardium at peak-systole. The unique geometries of all healthy and infarcted LVs at end-diastole and at peak-systole are summarized in **Figs A.4-A.5** respectively. The inclusion of papillary muscles as part of the LV lumen resulted to increases in LV volumes at end-diastole (7.6 μL) and at peak-systole (2.4 μL), contributing to an increase in ejection fraction values (3.11%) as shown in **Fig. A.6**.

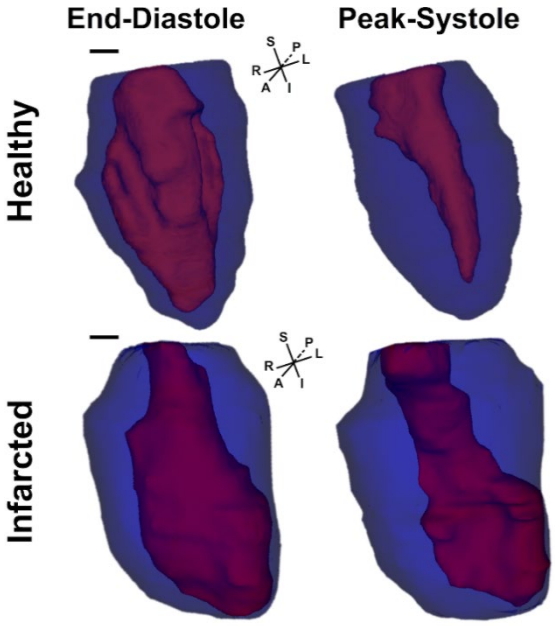

Fig. 4.3: 3D representations of the left ventricular lumen (red) and myocardial wall (blue) at end-diastole **(left)** and peak-systole **(right)** are shown for both healthy and infarcted mouse hearts. The asymmetrical anterior apical infarct is associated with wall thinning and dyskinesia of the necrotic myocardium at peak-systole. Scalebar = 1mm.

Bland-Altman percent difference analyses **(Fig A.7)** and correlation **(Fig. A.8)** of cardiac parameters calculated using the different techniques were conducted for both healthy and infarcted LVs. Although conventional 2D techniques performed similarly (within ±10%) to the direct 4D method in quantifying EF in healthy LVs, they performed significantly worse compared to both gold-standard MRI and the 4D method when evaluating EFs in infarcted LVs. Box-and-whisker plots showing percent difference for the different cardiac parameters between the 4D, 2D Simpson's, and 2D Teicholz techniques relative to MRI for infarcted LVs are shown in **Fig. 4.4**. **Table 4.2** shows the medians, as well as the 1st and 3rd quartile values [Q_1, Q_3] for the cardiac parameters calculated using the different techniques. Values of EF measured using the 2D Simpson's and Teicholz techniques deviated from that measured with MRI by 38.5% and 30.2% respectively. On the contrary, EF values obtained directly with the 4D technique only differed from that of MRI by 2.3%, with the 1st and 3rd quartile values confined between -10.9% and 17.3%.

4.4.2 Quantification of Dissecting AAA Regional Strain

A three-axis view of a mouse dissecting AAA acquired at diastole two-weeks post aneurysm formation is displayed in **Fig. 4.5**. The stratification of the aneurysm into the true and false lumen, as well as the formation of an intramural thrombus (black arrows), can be clearly seen in both the long and short-axis views. 3D masks of the dissecting AAA represent the vessel geometries during diastole (red) and systole (blue) and are shown in **Fig. 4.6A**. Increased wall stiffness, caused by the remodeling of the aneurysmal wall, accounted for the small distensibility observed within the aneurysm between diastole and systole [134-136]. Sections of the abdominal aorta proximal and distal to the aneurysm exhibited greater wall displacements as compared to those located in the middle of the aneurysms and its neighboring regions. Quantitative assessment of Green-Lagrange circumferential strain along the abdominal aortic wall is shown in **Figs. 4.6B-C** and **Fig. A.9**. The averaged circumferential strains of all seven mice plotted along normalized abdominal aorta positions illustrated that both proximal and distal regions have higher maximum strain values compared to regions within the aneurysm. Although wide variances in maximum strain persisted in proximal and distal regions, aneurysmal regions exhibited relatively low strain values of 1-2% with minimal variance. **Fig. A.10** further demonstrates the wall kinematics of a dissecting AAA two weeks following aneurysm formation.

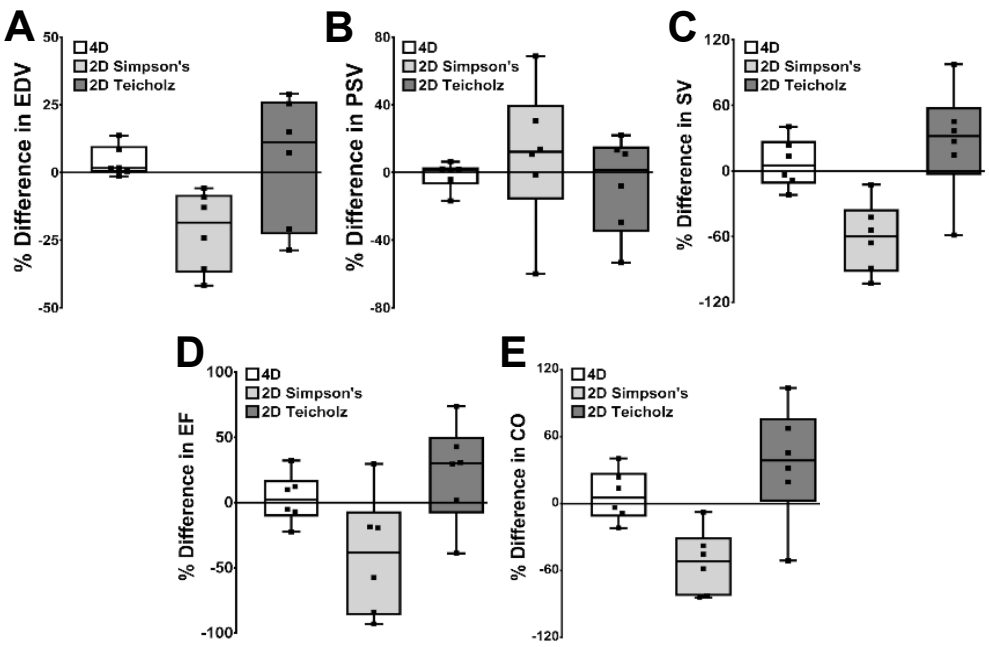

Fig. 4.4: Box-and-whisker plots showing percent difference in **A)** end-diastolic volumes (EDV), **B)** peak-systolic volumes (PSV), **C)** stroke volumes (SV), **D)** ejection fraction (EF), and **E)** cardiac output (CO) measured from the specified techniques with respect to those measured from MRI. The upper and lower boundaries of the box plots correspond to the first and third quartile values of the dataset. Note that compared to conventional 2D techniques, cardiac parameters measured directly using the 4D technique aligned more closely to those measured from gold-standard MRI.

Table 4.2: Summary of the Bland-Altman percent difference analysis of the 4D Ultrasound, Simpson, and Teicholz techniques with respect to MRI. EDV = end-diastolic volume, PSV = peak-systolic volume, SV = stroke volume, EF = ejection fraction, and CO = cardiac output.

Parameters		**Healthy**			**Infarcted**	
Cardiac	**Statistics**	**Simpson**	**Teicholz**	**4D**	**Simpson**	**Teicholz**
EDV (µL)	Median	-16.2	-6.8	1.6	-18.5	11.1
	$[Q_1, Q_3]$	[-21.8, -12.8]	[-24.0, 7.5]	[0, 9.7]	[-37.1, -8.3]	[-22.9, 26.3]
PSV (µL)	Median	-30.5	-22.1	1.5	12.2	1.5
	$[Q_1, Q_3]$	[-41.4, -16.5]	[-26.2, -9.4]	[-7.2, 3.1]	[-16.1, 40.0]	[-35.3, 15.5]
SV (µL)	Median	-14.0	-2.6	5.1	-59.9	31.9
	$[Q_1, Q_3]$	[-19.9, -7.8]	[-10.6, 12.6]	[-11.8, 27.7]	[-92.4, -34.9]	[-3.8, 58.3]
EF (%)	Median	5.3	4.3	2.3	-38.5	30.2
	$[Q_1, Q_3]$	[1.0, 8.9]	[1.2, 7.0]	[-10.9, 17.3]	[-86.4, -6.6]	[-8.4, 50.6]
CO (mL/min)	Median	-14.0	-2.6	5.2	-51.9	38.6
	$[Q_1, Q_3]$	[-19.9, -7.8]	[-10.6, 12.6]	[-11.8, 27.7]	[-82.8, -30.3]	[1.7,76.4]

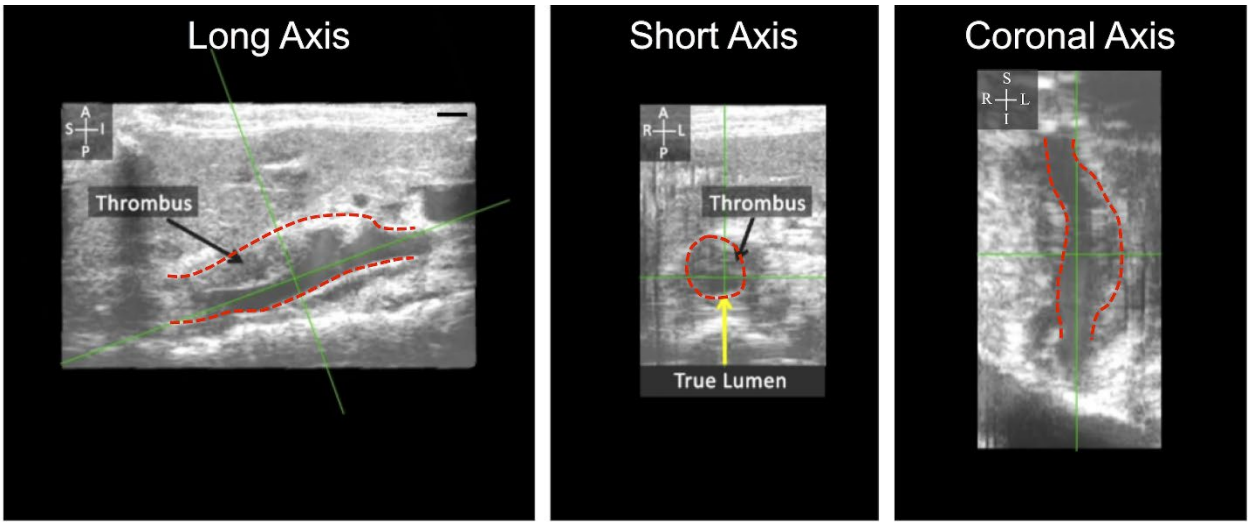

Fig. 4.5: Three-axis views of a representative mouse dissecting abdominal aortic aneurysm (AAA) at diastole. Black arrows point to the formation of intramural thrombus. Yellow arrow points to the true lumen, and dashed red lines outline the boundary of the AAA. Green crosshairs highlight the center of the visualized structure. Scalebar = 1mm.

4.5 Discussion

In this study, we presented a small animal ultrasound imaging technique to acquire gated volumetric datasets from both cardiac and vascular regions of interest. By employing cardiac-gating, respiration-gating, and image registration in conjunction with a high-frequency ultrasound transducer, we were able to collect volumetric data with both high spatial and temporal resolution. We used our 4D imaging technique to demonstrate that conventional echocardiographic methods perform unreliably in evaluating LV function in mice with myocardial infarction compared to direct volumetric assessment of LV function. We believe this is the first published report quantifying 4D echocardiography in small animals, revealing a better agreement with MRI data than standard 2D ultrasound. We also used our technique to show that Green-Lagrange circumferential strain decreased significantly within the aneurysmal region when compared to regions proximal and distal to the aneurysm. These results suggest that a 4D imaging approach may be advantageous when assessing cardiac and vascular function with complex geometries and kinematics.

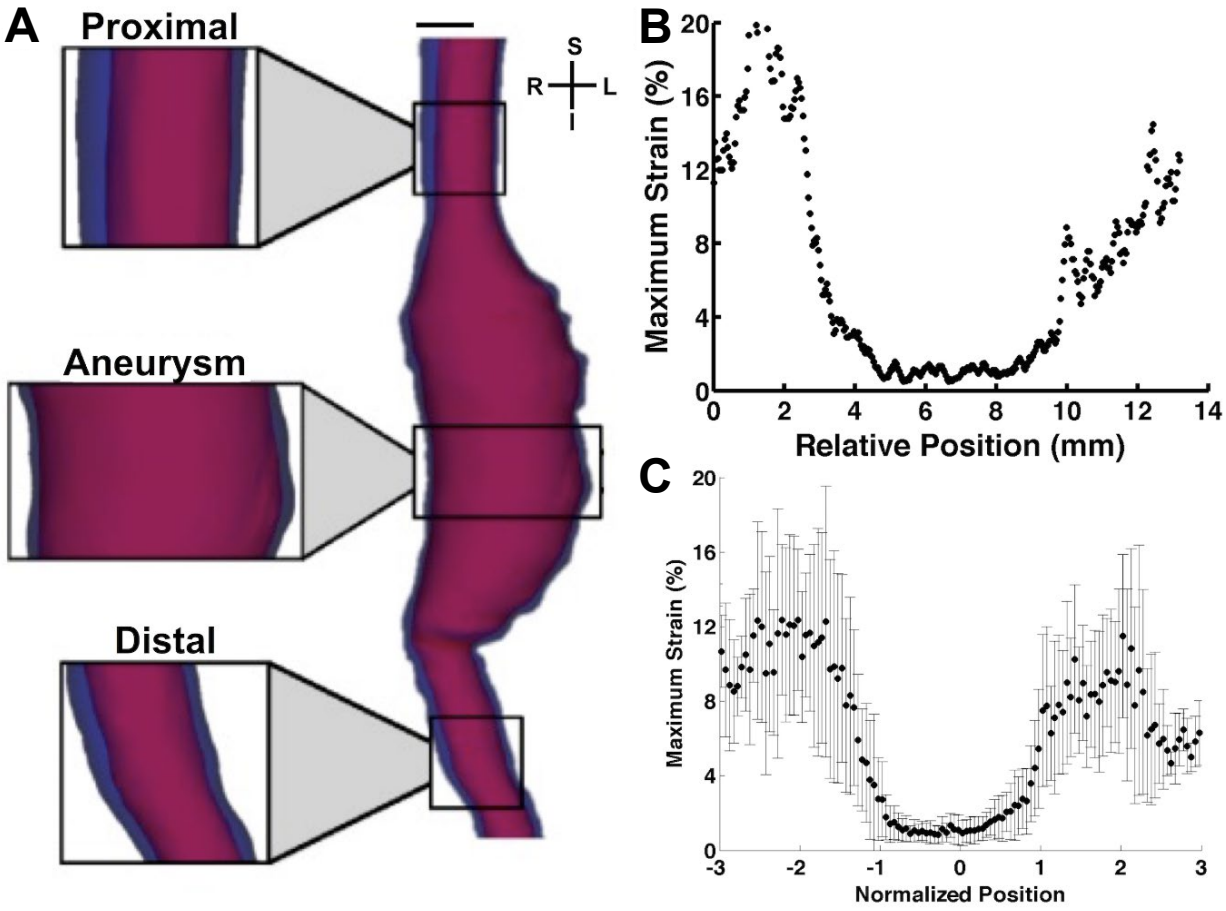

Fig. 4.6: A) 3D volume renderings of a representative mouse dissecting AAA during systole (blue) and diastole (red) are shown overlaid together, with the aneurysm positioned at the center. Enlarged subpanels demonstrate greater wall motion in the proximal and distal regions of the dissecting AAA, when compared to aneurysmal regions. **B)** Plots of Green-Lagrange maximum circumferential strain for the presented aorta, plotted relative to the abdominal aorta positions, highlight elastic walls located proximal and distal to the stiff aneurysm. **C)** Averaged Green-Lagrange maximum circumferential strain for dissecting AAAs (n=7) is plotted along normalized abdominal aorta positions, showing a stiffer aneurysmal region with reduced strain. Positions from the center of the aneurysms are normalized to half the aneurysm length so that the normalized position corresponding to the aneurysm falls within the -1 and 1 position. Data are shown as mean ± standard deviation. Scalebar = 1mm.

4.5.1 Conventional Echocardiographic Techniques Perform Unreliably in Evaluating Function in Diseased LVs

Conventional echocardiographic methods for evaluating cardiac health rely on geometrical assumptions from 2D B-mode slices to approximate LV volumes [130]. These techniques assume that LV cross-sections adopt circular shapes and can therefore be modeled as stacks of elliptical

discs. Unfortunately, these 2D techniques are susceptible to issues related to structural abnormalities not captured within the imaging plane, apical foreshortening, and large inter-observer variability [131,137]. Furthermore, these heuristic approaches are often violated when imaging patients or animals with complex cardiac pathologies that have regional dyssynchrony and ventricular dysfunction, leading to inaccurate estimations of LV volumes and ejection fractions [49,130,138]. Using the proposed 4D ultrasound technique described here, we can measure LV volumes and other parameters of LV function directly from complex 3D geometries, addressing these shortcomings.

Even in healthy hearts, the assumptions accompanying Simpson's rule may not accurately reflect the structure of the LV, due to the contribution of papillary muscles, as illustrated in **Figs. 4.2-4.3** and **Figs. A.4-A.6**. These assumptions prove to be especially problematic in the assessment of disease states, such as in hearts with asymmetrical apical infarcts **(Figs. 4.2-4.3** and **Fig. A.5)**. Depending on the transducer alignment relative to infarct geometry, 2D approximations of LV function may be grossly overestimated or underestimated, as reflected by the large observed percent difference between their values and that obtained from MRI **(Figs. 4.4, A.7,** and **Table 4.2)**, which we used as a gold-standard for this study. Comparisons of direct 4D ultrasound measurements with MRI, however, demonstrated that the 4D method performed similarly to MRI, as observed by the small percent difference depicted in **Fig. 4.4**. Furthermore, the interquartile ranges for all cardiac parameters obtained using the 4D approach were considerably narrower than those acquired from 2D Simpson's and Teicholz techniques, suggesting that the 4D method performed consistently compared to conventional techniques. Secondly, to compensate for dyskinesia in necrotic myocardial tissue and reduced contractility in regions neighboring the infarct zone, healthy regions of the left ventricle exhibit increased inotropy. This leads to LV geometries that depart from the assumed elliptical shape used in conventional 2D techniques. The data included here highlight the limitations of 2D ultrasound imaging, suggesting that gated volumetric approaches should be considered in studies of complex cardiac disease models with regional differences. It is important to note that the presented results were obtained from mice with large and asymmetrical infarcts. Further work will focus on studying how the performance of 2D techniques compares to the proposed method for less severe infarction models, such as the ischemia-reperfusion model [139], or in cases where cardiac remodeling has a uniform effect on heart structure. Taken together, the major advantage of the presented 4D technique is its ability to

capture exact LV geometry throughout the cardiac cycle, providing a more direct approach when evaluating LV function. This approach also opens the possibility of directly quantifying ventricular synchronicity and 3D strain maps of murine hearts using ultrasound.

4.5.2 Aneurysm Formation Reduces Green-Lagrange Circumferential Strain

The 4D ultrasound technique was also used to study regional differences in aortic wall kinematics. Although numerous ultrasound studies on murine dissecting AAAs have been conducted, many still rely on linear measurements of aortic diameter to characterize disease severity and quantify aortic wall strain [140,141]. Variations in aortic wall thickness, influenced by dissections and the presence of intramural thrombus **(Fig. 4.5)**, may lead to non-uniform distensibility and radial expansion of the aortic wall. In fact, performance comparison between planar-based ultrasound methods showed that the choice of imaging plane significantly affects the accuracy of the parameters such as aortic diameter and stiffness [142]. Using our 4D imaging technique, we were able to mitigate this problem by visualizing the pulsations of the AAA in 3D **(Fig A.10)** and characterizing circumferential aortic wall strain by measuring cross-sectional areas of the aorta. **Fig. 4.6** demonstrates that regions proximal and distal to the aneurysm exhibit high strain values as compared to the aneurysmal region, with the proximal regions showing higher strain values than the distal regions. The presence of branching vessels in distal regions of the abdominal aorta may contribute to the observed decreased strain values. This decrease in maximum Green-Lagrange circumferential strain in the aneurysmal region is likely due to an increase in vessel stiffness.

The results described here are consistent with previous reports showing an increase in vessel stiffness due to the degradation of elastin and increased collagen turnover [136,143]. This increase in vessel stiffness was also supported by previous reports demonstrating reductions in pulse-wave velocities along the aneurysmal wall [144-146]. Previous work using 2D M-mode ultrasound suggested that aneurysm formation typically decreased the Green-Lagrange circumferential strain from around 15% to 3% [136]. However, strain analysis using other imaging modalities, such as MRI, documented higher values of circumferential cyclic strain of 20% in healthy suprarenal aorta and 10% in AAAs [143,147]. This discrepancy is potentially due to inherent differences in imaging modalities since time-of-flight MRI has difficulty accurately assessing lumen size in regions of slow or complex flow that are often observed in dissecting

AAAs. Furthermore, MRI is subject to lower spatial and temporal resolution compared to ultrasound. Using our 4D technique, we have extended the analysis of Green-Lagrange circumferential strain from conventional 2D M-mode to diameters approximated from cross-sections of the 4D aneurysm data to take into account for non-uniform distensibility and radial expansion of the aortic wall. Applying a gated volumetric imaging technique to expand pulse wave quantification to 3D could further improve the characterization of mechanical factors that lead to aneurysm initiation, growth, and rupture.

4.5.3 Tradeoff Between Resolution, Acquisition Time, and Processing Time

One important concept to consider when acquiring 4D data is the tradeoff between image resolution and acquisition time. Depending on the region of interest location, size, and the disease model studied, the step size can be carefully selected to minimize acquisition and processing time while obtaining sufficient spatiotemporal resolution. In the presented work, we acquired data using small step sizes ranging from 80 μm to 200 μm and a sampling rate of 1,000 fps so that we were able to easily identify regional differences in the contractility of infarcted LVs and pulsatility of dissecting aneurysms. As such, the average imaging time ranged between 40 to 90 minutes for the cardiac and aneurysm data, respectively, with image reconstruction and analysis taking an additional 30 minutes. Although conventional 2D techniques can take on the order of 30 minutes for both acquisition and analysis combined, the need to obtain multiple 2D views at different positions when studying diseases exhibiting regional differences may significantly increase image acquisition times. Taken together, the results of this study suggest that acquiring 4D data with small step sizes and high sampling rates may not be necessary when assessing global cardiovascular function in healthy mice. The presented volumetric technique, however, allows for the visualization of regional differences that may be overlooked with conventional 2D approaches. Furthermore, the presented ultrasound technique opens the possibility of mapping 3D strain, quantifying ventricular synchrony/dyssynchrony, and estimating vascular pulse wave velocity with high spatiotemporal resolution.

4.5.4 Limitations and Future Work

A small animal ultrasound system capable of collecting 4D data has recently been made

commercially available (Vevo3100, FUJIFILM VisualSonics Inc. [44]). This newer imaging platform uses the same basic image acquisition process but has integrated software to automatically acquire 4D data, a maximum temporal resolution of 300 fps, and uses a dual-gating technology to accelerate image acquisition time. Still, the major factors influencing total imaging time are the choice of temporal resolution and step size. In this study, we chose a sampling rate of 1000 fps with small step sizes to allow for the collection of 4D data with both higher spatial and temporal resolution while acknowledging the tradeoff with longer acquisition times.

A limitation of the presented technique is the need to acquire data with minimal variations in heart rates. If large variations in heart rates are observed, temporal resampling and interpolation techniques should be implemented to ensure that images from successive spatial positions match in their cardiac cycle. Within an imaging session, data acquired when the mouse has a lower heart rate will have more time points representing a single cardiac cycle and may therefore need to be downsampled. 4D ultrasound imaging also faces several challenges in regards to data size and processing time. Our image data sizes reached magnitudes of 2-4 gigabytes depending on the dimensions of the structure of interest and step size between adjacent slices. While post-processing resampling of the compiled original resolution data could mitigate this problem, it sacrifices finer detail and requires data interpolation that may affect overall image quality. 4D imaging is also inhibited by long processing time primarily due to the manual segmentation process. Future studies into more robust and automated wall-tracking algorithms could reduce the segmentation time and improve its use of 4D imaging for other applications. Other future work will be needed to use 4D ultrasound data for computational fluid dynamic simulations and biomechanical modeling of blood flow.

4.6 Conclusion

The presented 4D ultrasound technique employs both cardiac and respiration gating to visualize the motion of three-dimensional structures with high spatiotemporal resolution, allowing for the study of complex cardiovascular kinematics in small animals. Specifically, we demonstrated the technique's ability to directly evaluate LV function and characterize Green-Lagrange circumferential strain in murine AAAs. Direct volumetric measurements of the LV from 4D cardiac data matched closely with gold-standard MRI results whereas 2D ultrasound techniques are sensitive to transducer alignment relative to infarct geometry. Strain analyses of

murine AAAs demonstrate that the aneurysmal region exhibited lower strain values when compared to proximal and distal sections, likely due to the remodeling of the extracellular matrix within the aortic wall. Given the current efforts in the field focused on studying regional differences in wall motion of mouse models with myocardial infarction and AAA, a 4D ultrasound approach could be beneficial for a wide variety of studies where direct volumetric measurements are important.

Ethical Approval

All procedures performed in studies involving animals were in accordance with the ethical standards of the Purdue Animal Care and Use Committee.

5. IMPLEMENTATION OF A 3D DIRECT DEFORMATION ESTIMATION STRAIN ALGORITHM

Now that we have established a novel ultrasound imaging technique capable of acquiring 4D cardiac data with high spatiotemporal resolution, the next step is to construct and optimize a reliable method for estimating 3D strain from image data. This chapter highlights our collaborative efforts in developing a regularization-free and noise-insensitive 3D strain algorithm. Specifically, we will discuss how direct estimation of deformation gradient fields from image warping functions leads to significant improvements in the accuracy and precision of the measured strain values compared to existing techniques. We will then highlight the application of our 3D direct deformation estimation (3D-DDE) strain algorithm in quantifying 3D strain of the left ventricle, both within the chordae tendineae and the myocardium. The content presented in this chapter is adapted from our previous work titled "Regularization-Free Strain Mapping in Three Dimensions, with Application to Cardiac Ultrasound," which was published in the *Journal of Biomechanical Engineering*. Significant modifications to the manuscript have been made to focus on the application of the 3D-DDE technique in quantifying myocardial strain and to highlight my scientific contribution to the published manuscript, of which I am a second author. Additional formatting edits have been made to produce a cohesive dissertation.

5.1 Abstract

Accurate quantification of dynamic strain fields from time-resolved volumetric medical imaging data is a pressing need in radiology. A critical limitation of all existing strain techniques is regularization. Because these volumetric images are inherently noisy, current strain mapping techniques must impose either displacement regularization and smoothing that sacrifices spatial resolution, or material property assumptions that presuppose a material model. Here, we present, validate, and apply the first three-dimensional (3D) method for estimating mechanical strain directly from 3D image stacks without regularization or assumptions about the material behavior. Specifically, we focus on its application in quantifying *in vivo* 3D myocardial strain from 4D

ultrasound data of both healthy and infarcted mouse left ventricles. We were able to verify high strain fields in healthy contractile tissue and low strain fields in diseased fibrotic scars, enabling the regional analysis of 3D myocardial strain. Taken together, the presented method shows promise for broad application to dynamic medical imaging modalities, including high frequency ultrasound, tagged magnetic resonance imaging, and confocal fluorescence microscopy.

5.2 Introduction

Quantifying deformation from time-resolved volumetric image data can significantly improve the study of diseases that alter the mechanical properties of biological tissues. For example, following a myocardial infarction (MI), fibrotic scar tissue gradually replaces the nonviable ischemic myocardium, leading to regional differences in stiffness that directly inhibit normal heart function. The ability to noninvasively quantify regional differences in myocardial contractility will provide significant information regarding the developing infarct scar, allowing for better characterization of post-infarction cardiac remodeling. However, *in vivo* assessment of spatially varying mechanical properties is challenging due to the limitations of existing image-based strain techniques. State-of-the-art digital image correlation (DIC) techniques, which match patterned features between pairs of images to estimate displacement fields over time, are only accurate when estimating two-dimensional (2D) displacement fields [82,148]. Accuracy suffers when three-dimensional (3D) motion causes image features to move into or out of the imaging plane [106,149], which is especially prominent in an organ like the left ventricle (LV) that undergoes significant 3D deformation [66,68]. As a result, 2D methods applied to 4D image data often yield strain measurements with significant errors and have limited clinical application.

Digital volume correlation (DVC) techniques can overcome this challenge by tracking displacement in 3D, but they still suffer from limitations on accuracy and precision. DVC techniques estimate displacement fields over time via a volumetric cross correlation approach that maximizes the similarity between groups of voxels in the initial reference volume and subsequent deformed volumes. Strain fields calculated from these estimated displacement fields suffer from the well-known challenge of taking numerical gradients of noisy data. This problem is exacerbated in DVC because volumetric image data often have higher resolution within the image acquisition plane or “slice” than between slices. Therefore, existing techniques must impose regularization, either by smoothing or by making guesses about the mechanical properties of the tissue being

imaged [148,150]. Even advanced regularization techniques, such as diffeomorphic smoothing [78,151], hyperelastic warping [152,153], or finite element based methods [80,154,155], have limitations. They either do not warp reference volumes when searching for their counterparts in deformed imaged volumes [78,151], require imposition of strain compatibility upon averaged fields [82], or require imposition of an assumed material model [78,152,153].

We therefore developed a novel 3D strain algorithm which reliably estimates strains within tissue volumes without material assumptions or regularization. The method, which we term 3D direct deformation estimation (3D-DDE), estimates deformation gradient fields directly from a novel warping function that maps targeted regions in the reference image volumes to their counterparts in the deformed image volumes without consideration of displacement fields, analogous to an earlier 2D implementation [106]. To validate and benchmark the method, the 3D-DDE algorithm was used to estimate strain fields from volumetric images that were deformed *in silico* with known deformation fields; its performance was then compared to other state-of-the-art 3D strain techniques. We then demonstrated the utility of 3D-DDE on 4D ultrasound data of both healthy and infarcted mouse LVs in performing the first full thickness strain mapping. We aim to show that spatial variations in strain are associated with both anatomical features and disease states of the LV. Taken together, the presented work demonstrate the feasibility of the 3D-DDE method in enabling the quantitative analysis of 3D strain from medical image data.

5.3 Methods

5.3.1 Acquisition of 4D Cardiac Ultrasound Data

We acquired *in vivo* ultrasound images of mouse LVs with a high-frequency small animal ultrasound system (Vevo2100, FUJIFILM VisualSonics Inc) and a 40 MHz linear array ultrasound probe (MS550D). We acquired 4D cardiac data from adult male C57BL/6J wild-type mice; to compare between disease states, images were acquired in both healthy mice (n=2) and mice with four-week old infarcts (n=2). Permanent ligation of the left coronary artery was performed to induce myocardial infarction. A detailed description of the 4D acquisition, data reconstruction, and surgical procedure can be found in **Chapter 4**. Linear interpolation was then used to resample the 4D data from its native voxel resolution (40μm x 90μm x 193μm; axial x lateral x elevational) to isotropic 60 μm voxels before implementation of the 3D-DDE strain algorithm.

5.3.2 Finite Strain Theory

In continuum mechanics, the deformation gradient tensor, **F**, describes the transformation of a material vector $d\mathbf{X}$ in the undeformed reference configuration at time t = 0 to the corresponding material vector $d\mathbf{x}$ in the deformed configuration (t ≠ 0). Mathematically, the relationship between the two configurations can be represented as **Eq. 5.1** below:

$$d\mathbf{x} = \mathbf{F}\, d\mathbf{X} \tag{5.1}$$

Once **F** is known, the Green-Lagrange strain tensor, **E**, can then be calculated as follows **(Eq. 5.2)**,

$$\mathbf{E} = \frac{1}{2}(\mathbf{F}^{\mathrm{T}}\mathbf{F} - \mathbf{I}) \tag{5.2}$$

where **I** is the second order identity tensor. Note that, although different forms of strain measures exist, we will only be focusing on the Green-Lagrange strain tensor in this dissertation.

When working with volumetric image data, 3D cross correlation (3D-XCOR) techniques are traditionally used to estimate displacement fields before calculating the deformation gradient tensor. Since XCOR calculates displacements, **u**, by maximizing the similarity between groups of voxels over time, these displacements are typically bounded to the centroids of matched image subregions. The displacements of the centroids can then be used to calculate **F** as follows:

$$\mathbf{F} = \frac{\partial}{\partial \mathbf{X}}(\mathbf{X} + \mathbf{u}) = \frac{\partial \mathbf{X}}{\partial \mathbf{X}} + \frac{\partial \mathbf{u}}{\partial \mathbf{X}} \tag{5.3}$$

3D-XCOR, however, has several notable limitations. First, as mentioned previously, displacement estimations are inherently noisy; numerical differentiation **(Eq. 5.3)** of these noisy data amplifies small errors, significantly impacting the accuracy of the measured strain fields. Second, since displacements at centroids, instead of the original image subregions, are used to estimate **F**, there is an inherent loss in the spatial resolution of the measured strain. For example, in the 3D-XCOR case shown in **Fig. 5.1A-B**, for every 8 image subregions analyzed, we only obtain one deformation gradient tensor. Even more sophisticated techniques like the 3D least square fit (3D-LSF) method, which improves upon 3D-XCOR by incorporating warping functions into the assessment of image similarities prior to displacement estimations, still suffer from this loss in resolution **Fig. 5.1C**.

An advantage of the 3D-DDE approach is that it does not rely on displacement field estimations to calculate strain. Instead, a novel spatially varying image warping function $\mathbf{W_{3D}}$ that best maps a single volumetric region in the template image, *T*, to its deformed image, *I*, was used to directly obtain the deformation gradient tensor **F**. This is possible because the warping function was carefully designed to model the affine transformation **A**, a 4x4 matrix with parameters **p**, of the undeformed image coordinates **X** to the deformed image coordinate **x**, as shown in **Eq. 5.4** below:

$$[\mathbf{x}\ 1]^T = \mathbf{W_{3D}}(\mathbf{X};\mathbf{p}) = \mathbf{A}(\mathbf{p})\ [\mathbf{X}\ 1]^T = \begin{bmatrix} 1+p_1 & p_4 & p_7 & p_{10} \\ p_2 & 1+p_5 & p_8 & p_{11} \\ p_3 & p_6 & 1+p_9 & p_{12} \\ 0 & 0 & 0 & 1 \end{bmatrix} \begin{bmatrix} X \\ Y \\ Z \\ 1 \end{bmatrix} \quad \textbf{(5.4)}$$

A simple way to conceptualize **Eq 5.4** is that the deformed image can be approximated by warping the undeformed image using affine transformation. Since the format $[\mathbf{x}\ 1]^T = \mathbf{A(p)}[\mathbf{X}\ 1]^T$ is analogous to $d\mathbf{x} = \mathbf{F}\ d\mathbf{X}$, the 3D deformation gradient tensor $\mathbf{F}_{3D}$ can be obtained directly from the affine transformation matrix, as shown in **Eq. 5.5**.

$$\mathbf{F_{3D}} = \begin{bmatrix} 1+p_1 & p_4 & p_7 \\ p_2 & 1+p_5 & p_8 \\ p_3 & p_6 & 1+p_9 \end{bmatrix} \quad \textbf{(5.5)}$$

To optimize the affine matrix parameter **p**, an iterative image registration technique called the Lucas Kanade (LK) inverse compositional algorithm was used. We will not go into detail regarding the LK optimization scheme, as this work has been widely published [156]. Briefly, the LK inverse compositional algorithm updates the warping parameter **p** by minimizing an energy function **(Eq. 5.6)**, which calculates the sum of squared error between the undeformed template image *T* and the deformed image *I* that has been warped back into the coordinate frame of the template image.

$$\sum [I(\mathbf{W}(\mathbf{X};\mathbf{p})) - T(\mathbf{X})]^2 \quad \textbf{(5.6)}$$

As described above, we can directly estimate $\mathbf{F_{3D}}$ during voxel intensity mapping by utilizing a novel warping function that maps image subregions in the reference configuration to its deformed state. Not only does this approach avoid the need to estimate strain from noisy displacement data, it also does not suffer from losses in resolution. As shown in **Fig. 5.1D**, the 3D-

DDE approach can independently calculate deformation fields from each image subregions without being constrained to the centroid of these subregions. **Fig 5.1** provides a detailed visual representation of how the different strain techniques, 3D-XCOR, 3D-LSF, and 3D-DDE, estimate $\mathbf{F_{3D}}$, highlighting the advantages and disadvantages of each approach.

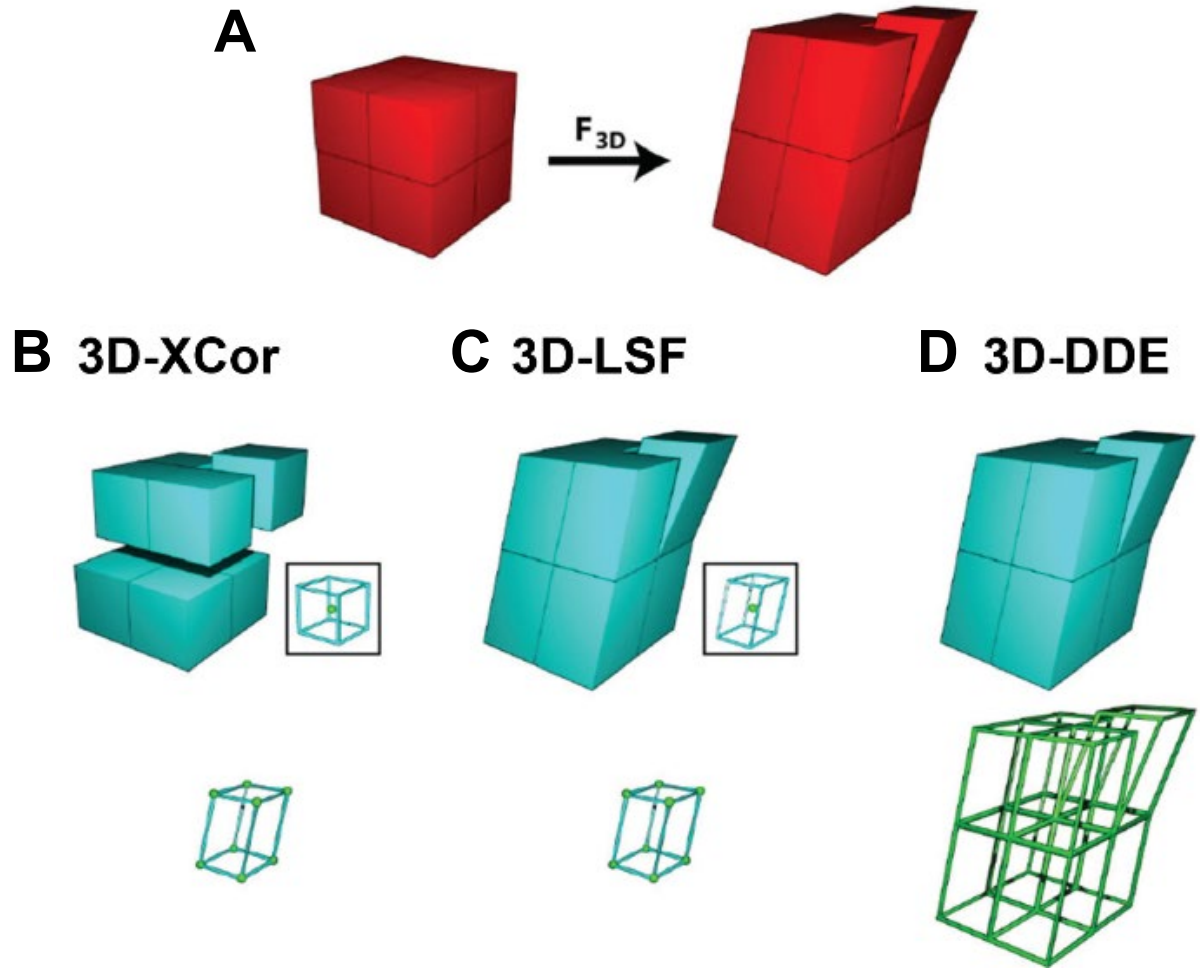

Fig. 5.1: Schematic representation of how 3D-XCOR, 3D-LSF, and 3D-DDE calculate 3D deformation gradient tensors, $\mathbf{F_{3D}}$. **(A)** Representation of a volumetric image divided into 8 volumes with original undeformed image **(left)** and deformed configuration **(right)**. **(B)** 3D-XCOR estimates how each reference volume maps to an equal number of voxels in the deformed image. Considering the centroid of each region (green spheres, inset and bottom), 3D-XCOR finds a best fit displacement. **(C)** The 3D-LSF method improves on 3D-XCOR by warping the reference regions before finding the best match in the deformed image. Like 3D-XCOR, it considers the displacements of the centroids of these regions when calculating deformation (inset and bottom row). **(D)** 3D-DDE accurately calculates the deformation of all eight regions independently (green outlines, bottom row).

5.3.3 *In Silico* Validation of 3D-DDE

Now that we have described the principles behind 3D-DDE and demonstrate how, in theory, it improves the estimation of 3D strain fields compared to traditional approaches, a thorough validation study is necessary. Our collaborators at Washington University in Saint Louis and Columbia University conducted all validation studies *in silico*. Briefly, artificially generated image volumes were subjected to different types of deformation, including a rigid body rotation, linear stretching, and non-linear stretching. More complicated strain fields, for which the exact solutions are known, were also applied to artificially generated image data. The performance of 3D-DDE in estimating strain fields from these test cases were then compared to results measured from 3D-XCOR and 3D-LSF. Specifically, the root mean square errors for all methods were compared to benchmark the accuracy and precision of the 3D-DDE technique. **Appendix B.1** of this dissertation describes in detail the methods and results of the validation work.

5.3.4 Implementation of 3D-DDE to 4D Cardiac Ultrasound Data

Before applying the 3D-DDE method to analyze strain from 4D cardiac ultrasound data, several key parameters need to be optimized to obtain meaningful results. These parameters, which include the size of the investigation region and grid spacing, should be appropriately chosen depending on several characteristics of the data. The pixel resolution of the image data, relative size of the structure to be analyzed, and the expected displacements that the structure undergoes between successive time steps are all important features that need to be considered when implementing the 3D-DDE strain algorithm.

As mentioned previously, the warping function maps a single volumetric region in the undeformed image to its deformed state by optimizing parameters in the affine transformation matrix. The size of this volumetric region, which we will herein refer to as the investigation region (red box, **Fig. 5.2A**), needs to be determined carefully based on the expected displacements of image features used to minimize the energy function. For ultrasound data, image intensities of the unique speckle patterns within the myocardium are used as image features. We need to ensure that with each incremental timestep, the displacements of these speckle patterns are sufficiently small to be captured within the vicinity of the investigation region. In practical terms, we want to avoid a scenario where these speckle features displace significantly far away (greater than 20% in each

dimension) from the size of the investigation region. In these cases, we observed that the LK method often fails to converge to reliably find accurate solutions. Another important aspect to consider when determining investigation region size is the dimensions of the structure to be analyzed. To ensure accurate estimations of strain, the investigation region needs to be sufficiently smaller than the analyzed structure. If the size of the investigation region is larger than the pixel dimensions of the structure, speckle features of the surrounding tissues will be inappropriately introduced into the calculation of the deformation gradient tensor, leading to inaccurate strain measurements.

A second key parameter to note is grid spacing, which refers to the spacing across which the investigation region is centered and constrained to (yellow grid lines, **Fig. 5.2B**). The 3D-DDE algorithm iteratively navigates through the 3D volume to estimate the optimal warping function for an investigation region centered at each of the grid intersections, before repeating this process across all time points. Since grid spacing corresponds to the position at which the deformation gradient tensor is evaluated, it controls the resolution of measured strain fields. To better resolve strains within a structure of interest, the grid spacing should be small enough to differentiate between tissues with different material properties. However, it is important to note that a tradeoff exists between small grid spacing (and therefore high strain resolutions) and computational time. Finally, since the 3D-DDE algorithm calculates strain from image pixel data, without consideration of physical dimensions, the size of the investigation region, grid spacing, and the interpretation of the strain results need to also reflect the resolution of each individual pixels.

To apply the 3D-DDE algorithm to our 4D ultrasound data, we first resampled the image data to 60 μm isotropic voxels so that we do not have to consider for direction-dependent sizes of the investigation region and grid spacing, simplifying the interpretation of the measured strains. We also defined end-diastole as the reference timepoint where the LV is in its undeformed configuration. From our ultrasound data, we observed that mouse LV wall thickness in its relaxed state (i.e. end-diastole) ranged from 1.1-1.3 mm, similar to previously published results [157]. Furthermore, we also measured that, on average, the endocardial wall of a healthy mouse LV displaced between 0.8-1.0 mm from diastole to systole. With this information, we tested several different parameters for investigation region size and grid spacing on test data sets to determine the optimal combination of these values. We found that a rectangular coordinate grid spaced 5 pixels apart with an 11x11x11 pixels^3 investigation region provided the best convergence ($\varepsilon <$

0.006) with reasonable computational times (~2-3 hours per dataset). **Table 5.1** summarizes the key characteristics of the 4D data and parameters of the 3D-DDE algorithm.

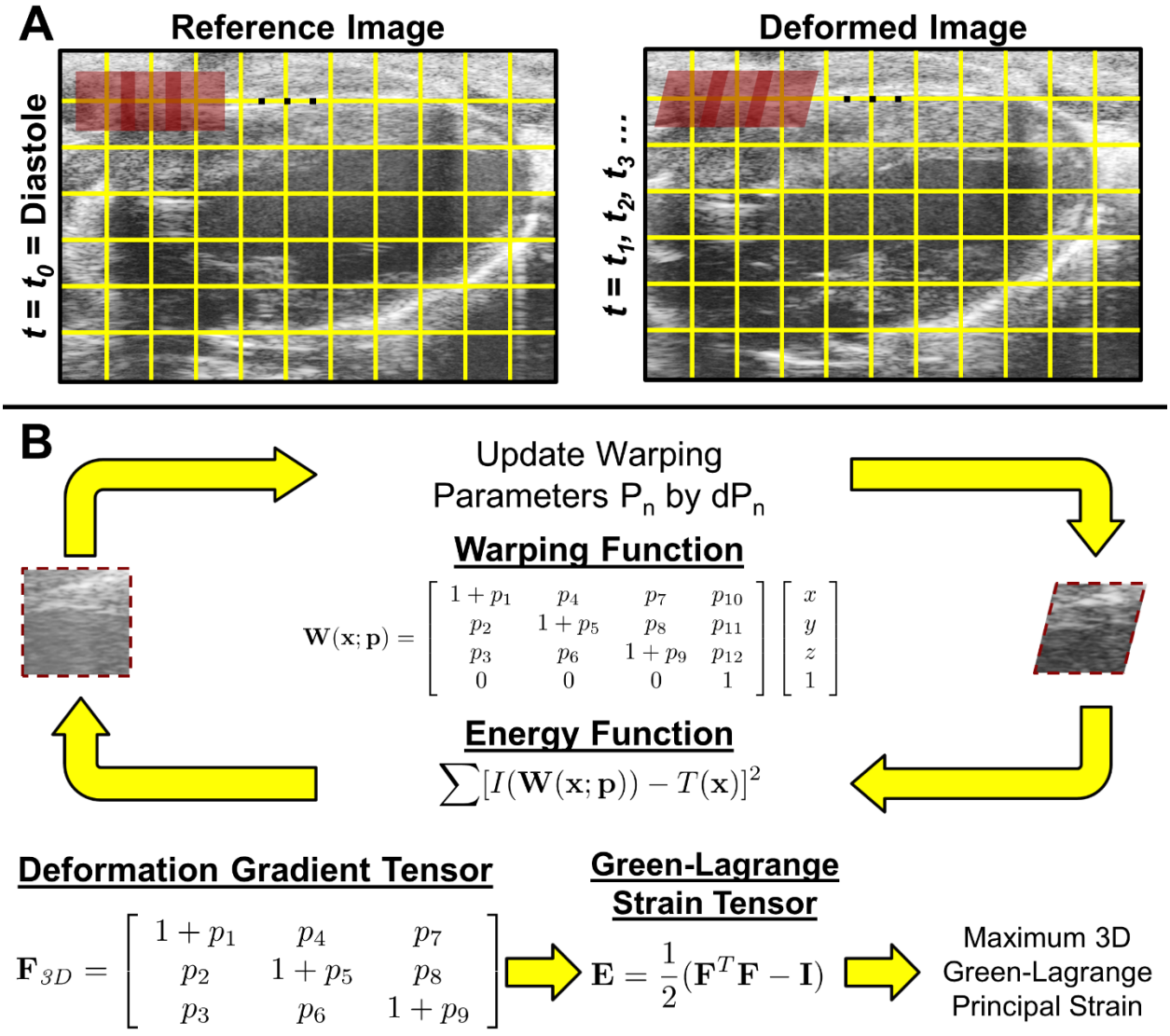

Fig. 5.2: (A) Two-dimensional representation of 3D-DDE implementation to 4D cardiac ultrasound data. Ultrasound images are divided into multiple investigation regions (red boxes) centered and constrained to gridlines (yellow lines). **(B)** Warping functions that map the corresponding investigation regions from the undeformed state at diastole to a deformed configuration at successive timepoints are calculated by the Lucas-Kanade inverse compositional algorithm. The 3D deformation gradient tensor $\mathbf{F_{3D}}$ is extracted directly from the optimized warping functions and used to calculate Green-Lagrange strains. Note that the size of the evaluation region and the grid spacing are not drawn to scale.

Table 5.1: Summary of key characteristics of the 4D data and the 3D-DDE algorithm

4D Ultrasound		3D-DDE	
Parameter	**Value**	**Parameter**	**Value**
Resampled Voxel Resolution	60 μm^3	**Size of Investigation Region**	11 x 11 x 11
Temporal Resolution	1 ms	**Grid Spacing**	5 x 5 x 5
Average Number of Frames in a Cardiac Cycle	100 ± 8	**Convergence criteria (ε)**	< 0.006

5.4 Results

5.4.1 3D-DDE Enabled the First Full 3D Strain Mapping of the Papillary Muscles

The 3D-DDE method was able to map, for the first time, full 3D strain fields of the papillary muscle, an important heart structure that assist in the opening and closing of the atrioventricular valves **(Fig. 5.3)**. Using end-diastole as a reference timepoint, the papillary muscle was manually segmented from the myocardium. Throughout systolic contraction, the first principal component of the 3D Green-Lagrange strain tensor continued to increase until it reached maximum strains on the order of 0.5 at peak-systole, just prior to the initiation of isovolumic relaxation **(Fig. 5.3C-E)**. As the LV began to relax during early ventricular filling, these high strain levels gradually decreased, approaching baseline values after late ventricular filling **(Fig. 5.3F-G)**. One important finding that we observed was that the chordae tendineae, which connect the papillary muscle to the atrioventricular valves, underwent lower straining throughout the entire cardiac cycle (yellow arrows, **Fig. 5.3C-G**) when compared to the apical regions of the papillary muscles that attach to the LV myocardium (white arrows, **Fig. 5.3C-G)**. Furthermore, in the vicinity of the chordae tendineae to papillary muscle insertion site, a substantial change in strain was noted, with a transition from the highest to lowest tensile principal strains evident **(Fig. 5.3)**. These regional variations in strain could not be appropriately captured using traditional techniques such as 3D-XCOR.

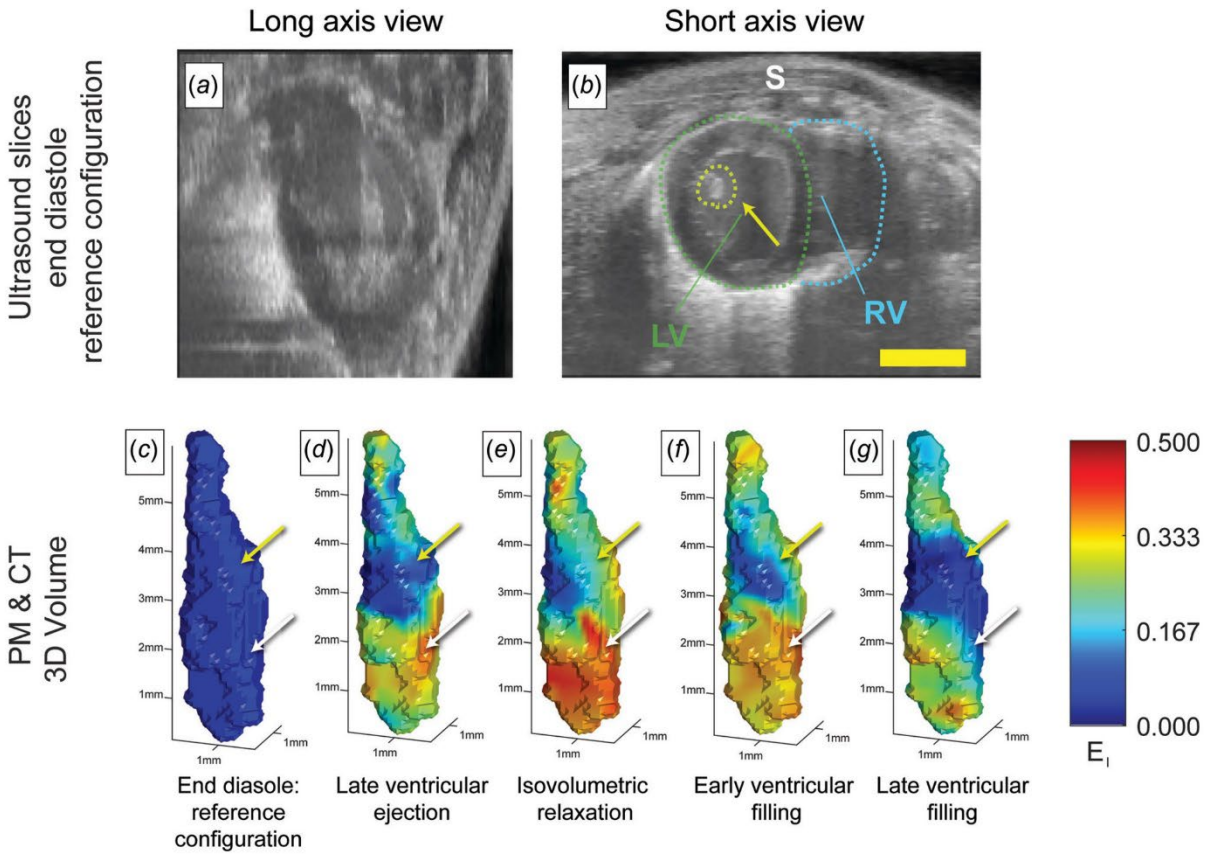

Fig. 5.3: Peak principal strain fields estimated from 4D ultrasound imaging of a beating mouse heart, showing spatial variations associated with the structure of the papillary muscle. **(A-B)** Volumetric ultrasound data were acquired over several cycles of a beating mouse heart and then analyzed using 3D-DDE to detect spatial variations in maximum principal 3D Green-Lagrange strain fields. **(C-G)** Manual segmentation was performed to map 3D strains onto the surface of the LV papillary muscle and to demonstrate how 3D strain fields varied near the insertions of the chordae tendinae. **(C)** End diastole was taken as a reference configuration. **(D)** The heart developed strains in the left ventricle as it contracted and blood was ejected from the heart, while the papillary muscles remained unstretched. **(E)** As the heart cycle reached peak-systole and entered isovolumetric relaxation, principal strains in the heart wall reached maximum levels on the order of 0.5. **(F)** As the heart relaxed during early ventricular filling, strain levels reduced, approaching baseline levels after **(G)** late ventricular filling. Throughout the cardiac cycle, strains in the papillary muscles (yellow arrows) were lower than those in the surrounding myocardium in the apex (white arrows). LV: left ventricle, RV: right ventricle, S: skin. Scalebar: 3mm.

5.4.2 Regional Differences in LV Mechanics Can be Characterized with 3D-DDE

Regional differences in myocardial mechanics were observed between healthy mice and mice with four-weeks old infarcts. At peak-systole, healthy LVs exhibited uniform contraction with peak strains on the order of 0.4-0.45 **(Fig. 5.4A)**. Regional analysis of maximum principal

3D Green-Lagrange strains, $\mathbf{E_I}$, at select markers throughout the myocardium confirmed this behavior, as strain peaks across the different regions of the LV overlapped at the same phase of the cardiac cycle **(Fig. 5.4C)**. On the contrary, in infarcted LVs, significant reductions in strain were detected at the apex of the LV ($\mathbf{E_I} < 0.1$), where the stiff, non-contractile infarct scar tissue resulted in long-term thinning of the LV wall and chamber dilation (yellow dashed lines, **Fig. 5.4B**). Interestingly, regions of the myocardium located at the base of the LV maintained healthy levels of strain, which appeared to be slightly but not significantly lower than healthy controls. We also noted non-uniform contractile patterns in the infarcted LVs. Regions of the myocardium closer to the infarcted tissue appeared to exhibit delayed contraction, as the strain peaks emerged at a later phase in the cardiac cycle **(Fig. 5.4D)**.

5.5 Discussion

5.5.1 3D-DDE Outperforms Displacement-Based Methods in Estimating Strain Fields

3D-DDE provided accurate and precise local estimates of complex, non-uniform strain fields **(Appendix B.1)**. The algorithm was insensitive to noise compared to both 3D-XCOR and 3D-LSF, as observed by its small root mean square errors **(Appendix B.1)**. Although other technologies could be tailored through regularization, smoothing, or imposition of a hyperelastic constitutive law, 3D-DDE provided improvements in strain accuracy and precision without such *ad hoc* constraints or *post hoc* regularization. The key feature of 3D-DDE that enabled this are unique from other cross-correlation techniques: 1) optimal 3D warping of images using the established Lucas-Kanade algorithm [156] and 2) direct calculation of the deformation gradient tensor without taking the numerical gradients of noisy displacement fields. The latter allowed for robust identification of strain concentrations and strain gradients.

Out-of-plane motion and deformation are challenges for all 2D and 3D imaging modalities. In 2D, such motion and deformation are impossible to track in the absence of additional information [82,151-153]. In 3D, reduced resolution in the out-of-plane direction leads to reduced resolution in displacements, which increases the error in strain estimation when the gradients of these displacement fields are calculated. By eliminating the need for these numerical derivatives, the current method eliminates this source of error. Taken together, the method outperforms state-of-the-art techniques, especially when strain concentrations and gradients existed.

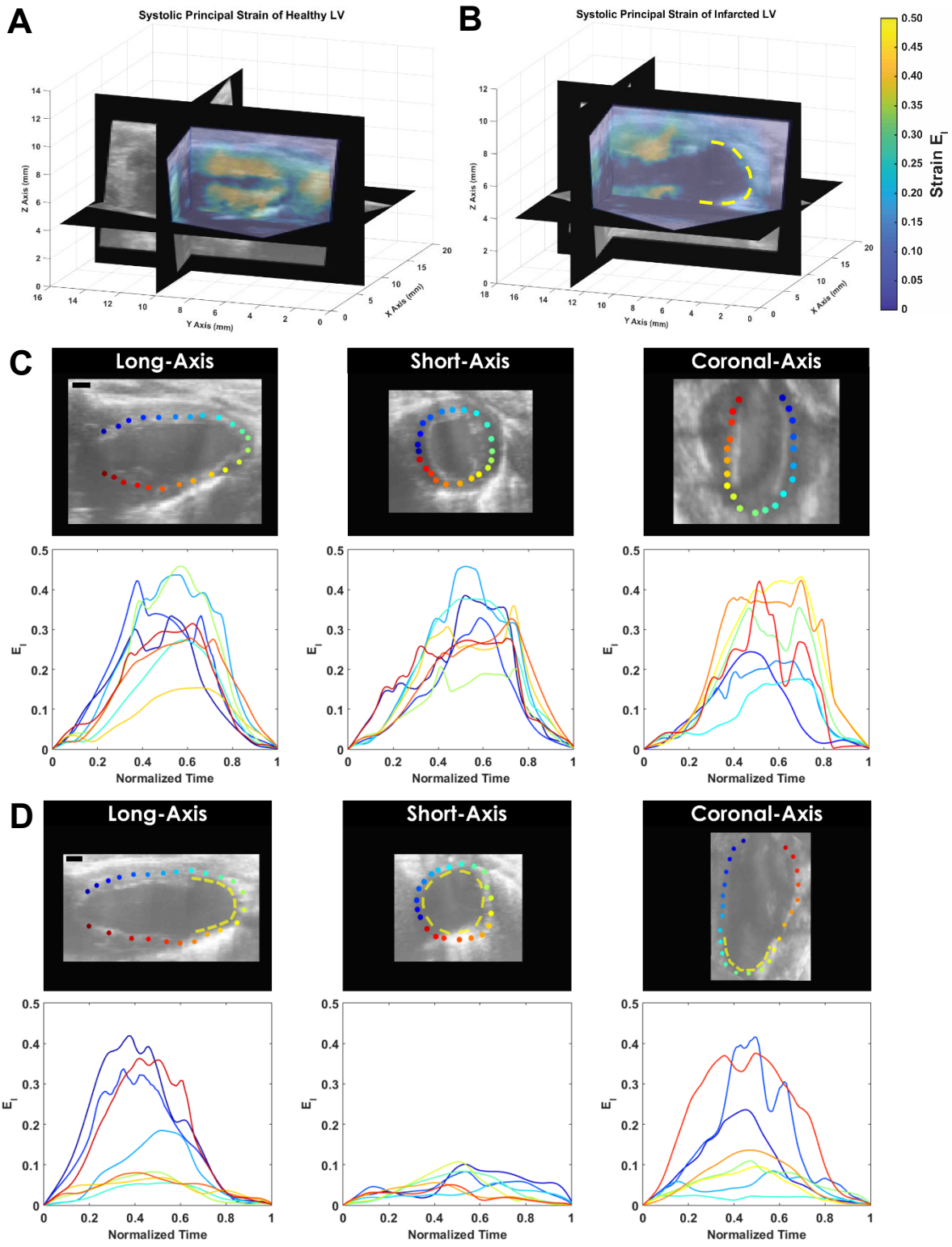

Fig. 5.4: Maximum principal 3D Green-Lagrange strain maps of mouse LVs **(A)** before and **(B)** four-weeks post-infarction surgery showed strain reductions in infarcted tissues (yellow dashed line). **(C,D)** Temporal strain plots at select markers highlighted a decrease in strain from 0.4 to 0.1 between healthy and infarcted myocardium, respectively.

5.5.2 3D-DDE Enables Regional Assessment of Strain from 4D Ultrasound Data of Mouse Left Ventricles

The noise-insensitivity of 3D-DDE enabled the analysis of noisy, volumetric, high frequency ultrasound images of a beating mouse heart, resolving for the first time the local strain patterns throughout the cardiac cycle without resorting to *post hoc* regularization schemes. The peak principal strains, which in general corresponded to radial strains fields, were on the order of those reported in a recent meta study [158].

This study presented the first analysis of strain fields associated with the insertion of the chordae tendineae into the papillary muscle of the myocardial wall. This is a compelling application because no other technology exists for assessing the risk of chordae tendineae rupture, which is often lethal [159]. The low principal strains of the chordae tendineae obtained *in vivo* from the 3D-DDE method yielded similar results to a previous *ex vivo* study, which reported a maximum strain of 4% in a porcine chordae tendineae under physiological loading [160]. Because the chordae tendineae are more than an order of magnitude stiffer than the papillary muscles [160,161], this insertion site is susceptible to elevated strains. Indeed, the most common site of papillary muscle rupture observed clinically in the setting of acute myocardial infarction is the site where we observed a substantial transition from highest to lowest strain [162].

3D-DDE also captured strain differences between the healthy and infarcted myocardium. The infarcted myocardium exhibited significantly attenuated strain magnitudes relative to the healthy contractile myocardium. These attenuated strain fields indicated that the local remodeling following myocardial infraction [163-165] produced scar tissue that was significantly stiffer than the surrounding healthy tissue. The non-contractile scar tissue ($\mathbf{E}_\mathbf{I} < 0.1$) was relatively resistant to extension as the surrounding myocardium maintained healthy levels of contractility ($\mathbf{E}_\mathbf{I} > 0.4$). Standard techniques such as 3D-XCOR could not reproducibly resolve these features. We note that the choice of reference configuration would affect the magnitudes of strains but not the qualitative trends, as the deformation gradients calculated using any reference configuration over the cardiac cycle can be calculated as a linear transformation of those calculated here. The current study demonstrates that mechanical damage due to myocardial infarction can be quantified noninvasively using high frequency ultrasound as a diagnostic tool.

The presented results provide one of the first *in vivo* regional quantifications of 3D strain in tissues with both healthy and diseased components, while demonstrating that our technique can

readily resolve small structural differences effectively. Although no gold standard exists for comparison, the strain fields measured by 3D-DDE are qualitatively as expected. High strains in the ventricular wall correlated with healthy ventricular contraction, and relatively small strains were observed in the stiff chordae tendineae. These results were expected due to the high stiffness mismatch of the chordae tendineae and the more compliant myocardium. Our results demonstrate that mechanisms appear to be in place to limit elevations of strain at the insertion of chordae tendineae into the papillary muscle in the wall of the heart. The absence of local strain concentrations at the points of insertion, where gross wall strains change substantially, suggest a future target for mechanically based diagnosis of structural pathologies related to valve function.

5.6 Conclusion

In this chapter, we have presented a reliable and accurate direct deformation estimation approach for quantifying 3D strain from 4D image data. The method, which we termed 3D-DDE, is an improvement to traditional image-based strain estimation techniques as it does not impose *ad hoc* constraints or *post hoc* regularization. By calculating deformation gradient fields directly from a novel warping function that maps targeted regions in the reference image volumes to their counterparts in the deformed image volumes, we can circumvent the need to take numerical gradients of noisy displacement fields before estimating strain fields. This implementation makes the 3D-DDE method insensitive to noise compared to conventional 3D strain techniques, as demonstrated *in silico* from test cases with known analytical solutions. We demonstrate the application of the technique in mapping, for the first time, the full 3D strain fields of the papillary muscles and LV myocardium. Specifically, we can detect regional differences between the mechanical properties of healthy and infarcted myocardial tissues in mice subjected to infarction surgeries. Although here we only demonstrate the application of 3D-DDE in analyzing 4D cardiac ultrasound data, this robust strain algorithm holds tremendous potential for a variety of application where local strain fields need to be estimated from image data.

Acknowledgement

We would like to acknowledge Drs. John Boyle, Roger Rowe, Robert Pless, Stavros Thomopoulos, and Guy Genin for developing, validating, and benchmarking the 3D-DDE algorithm.

6. LONGITUDINAL CHARACTERIZATION OF 3D MYOCARDIAL STRAIN

Now that we have developed the necessary tools to acquire 4D cardiac data and quantify 3D strain, we will demonstrate how integrating both techniques enable us to better characterize the role of regional myocardial strain in driving post-infarction remodeling. This chapter highlights one of the first reports investigating longitudinal changes in the spatial distribution of 3D myocardial strain in murine models of acute MIs. By mapping strain profiles to animal-specific 3D geometries of the remodeling LVs, we can visualize how early changes in mechanical strain precede structural remodeling. Furthermore, since we identified unique strain patterns between mice with varying infarct severities, we demonstrate the feasibility of the presented strain analysis technique in the early prediction of LV remodeling outcomes. The content presented in this chapter is adapted from our work titled "3D Myocardial Strain Correlates with Murine Left Ventricular Remodeling Severity Post-Infarction," which was recently accepted for publication in the *Journal of the Royal Society Interface*. Minor edits to the formatting and wording have been made to construct a cohesive dissertation.

6.1 Abstract

Heart failure continues to be a common and deadly sequela of myocardial infarction (MI). Despite strong evidence suggesting the importance of myocardial mechanics in cardiac remodeling, many MI studies still rely on 2D analyses to estimate global left ventricular (LV) function. Here, we integrated 4D ultrasound with 3D strain mapping to longitudinally characterize LV mechanics within and around infarcts in order to study the post-MI remodeling process. To induce infarcts with varying severities, we separated fifteen mice into three equal-sized groups: 1) sham, 2) 30-minute ischemia-reperfusion, and 3) permanent ligation of the left coronary artery. 4D ultrasound from a high frequency small animal system was used to monitor changes in LV geometry, function, and strain over 28 days. We reconstructed 3D myocardial strain maps and showed that strain profiles at the infarct border followed a sigmoidal behavior. We also identified that mice with mild

remodeling had significantly higher strains in the infarcted myocardium when compared to those with severe injury. Finally, we developed a new approach to noninvasively estimate infarct size from strain maps, which correlated well with histological results. Taken together, the presented work provides a thorough approach to quantify regional strain, an important component when assessing post-MI remodeling.

6.2 Introduction

Coronary artery disease remains the leading cause of death in the United States, with over 1 million acute coronary events predicted to take place in 2019 [3]. Despite recent advances in percutaneous coronary intervention technologies, which have improved patient survival rates, heart failure continues to be a common long-term complication of acute myocardial infarction (MI) with high morbidity and mortality [166]. Cardiac remodeling post-MI encompasses a series of complex molecular, structural, and functional changes in the left ventricle (LV) driven by inflammation, neurohormonal, and mechanical factors [4,21]. Although the short-term effects of remodeling are vital in repairing the damaged myocardium, sustained imbalance between increased hemodynamic load, compromised myocardial mechanics, and impaired cardiac function feeds a pathological response that results in LV dilation and eventual heart failure [4,21]. Specifically, changes in the mechanical microenvironment regulates myofibroblast proliferation and subsequent collagenous scar formation at the infarct border zone, providing the heart with the structural rigidity necessary to minimize infarct expansion and prevent ventricular rupture [4,167]. The developing myocardial scar, although beneficial early in remodeling, reduces LV compliance over time, directly inhibiting LV pumping function [14]. Taken together, the time course, mechanical properties, and size of the myocardial scar tissue are all critical components that determine the fate of the remodeling LV.

Despite strong evidence supporting the importance of myocardial mechanics in remodeling post-MI [14,167,168], longitudinal assessment of regional LV mechanics proves to be challenging. The majority of *in vivo* infarction studies still rely on 2D image analyses to estimate global metrics of LV function such as ejection fraction and global longitudinal strain [169-171]. These metrics, while valuable in evaluating the overall impact of ischemic injury on cardiac health, do not capture regional differences in myocardial contractility. Furthermore, strain measurements derived from 2D images are sensitive to through-plane motion caused by LV twisting during contraction [90].

Irrespective of these limitations, 2D maps highlighting regional strain differences still provide important spatial and temporal information regarding changes in LV contractility throughout remodeling [89,172].

Recent developments in noninvasive 4D imaging techniques have made it possible for researchers to reconstruct volumetric maps of patient- or mouse-specific LV geometries throughout a cardiac cycle [104,173,174], opening the possibility for 3D strain mapping of the heart. Indeed, several groups have quantified regional differences in 3D strain in both healthy [175,176] and ischemic LVs [177-179], with results revealing significant strain reductions within infarcted tissue. However, these studies either evaluated strain at only sparse timepoints [177,178] or relied on contrast agents to quantify strain in the remodeling infarct [179]. The reported strain difference between the infarcted and remote myocardium suggests the presence of a strain gradient near infarct border zones that may play an important role in infarct expansion.

A thorough longitudinal study investigating changes in the spatial distribution of 3D myocardial strain in a murine model of acute MI has not yet been conducted. Here, we integrated high resolution 4D ultrasound imaging [173] with 3D strain mapping [177] to monitor cardiac remodeling over 28 days. By employing two surgical mouse models to induce ischemic damage with varying severities, we identified unique remodeling patterns that differed between ischemia-reperfusion and permanent ligation models. By expanding ultrasound strain studies to 3D, we aim to provide further evidence that the mechanical behavior of the LV near infarct border zones contribute to infarct expansion and ventricular remodeling.

6.3 Materials and Methods

6.3.1 Coronary Artery Ligation

We randomly assigned fifteen male, wild-type, C57BL/6J mice (age = 14±1 weeks; weight = 27±3 grams; The Jackson Laboratory, Bar Harbor, ME) into three surgical groups: 1) sham (n=5), 2) ischemia-reperfusion (I/R; n=5), and 3) permanent ligation (PL; n=5). For surgery, each mouse was anesthetized with 1-3% isoflurane and endotracheally intubated to a small animal ventilator (SomnoSuite, Kent Scientific, Torrington, CT). Pressure-controlled ventilation supplied air to the lungs with a target inspiratory pressure between 16-18cm H_2O and a peak-end expiratory pressure between 3-5cm H_2O. We secured the mouse to a heated surgical stage and coupled a rectal

temperature probe to a homeothermic control module to maintain body temperatures between 36-37°C (RightTemp, Kent Scientific, Torrington, CT). We made a small incision in the 3rd intercostal space of the left thorax and retracted the ribs to expose the LV. The pericardium was dissected to visualize the left coronary artery (LCA). In the sham-operated controls, an 8-0 nylon suture was looped around the LCA without ligating the vessel. In the I/R group, we used a PE-10 tubing in combination with a suture, to temporarily ligate the LCA for 30-minutes before restoring blood flow to the ischemic myocardium (reperfusion) as described previously [180]. In the PL group, the LCA was permanently ligated to induce an infarct [180]. At the end of the procedure, we sutured the incision site and recovered the mouse. All surgical procedures were performed aseptically, and buprenorphine (0.05 mg/kg; ip) was administered as an analgesic. All procedures were approved by the Purdue Animal Care and Use Committee.

6.3.2 Longitudinal Ultrasound Imaging

All ultrasound images were collected with a Vevo2100 small animal ultrasound system (FUJIFILM VisualSonics Inc., Toronto, Canada) and a 40MHz center frequency linear array transducer (22-55MHz; MS550D). Ultrasound images of the LV were acquired at baseline and on days 1, 2, 3, 5, 7, 14, 21, and 28 post-surgery. **Fig. 6.1A** summarizes the study design for the presented work. We acquired 4D ultrasound data as described previously [173]. Briefly, successive cardiac and respiratory-gated 2D cine loops were obtained at 1000Hz in short-axis from the apex to the base of the heart by utilizing a linearly translating 3D motor (step size = 0.2mm; **Fig. 6.1B**). Respiratory waveforms obtained during imaging were used to ensure that ultrasound images were only acquired in between breaths to minimize breathing motion artifacts. Sequential 2D images were then spatially registered, temporally matched based on their relative time in the cardiac cycle, and resampled to isotropic 60μm voxels in MATLAB (MathWorks Inc., Natick, MA). Additionally, we measured mitral valve inflow velocities from the four-chamber view of the heart with pulsed-wave Doppler.

6.3.3 Ultrasound Image Analysis

6.3.3.1 Segmentation of Left Ventricular Boundaries

Reconstructed 4D ultrasound data were matched spatially with a custom MATLAB script by utilizing anatomical landmarks such as the sternum, apex, and heart valves. The reoriented 4D data were then loaded into SimVascular for segmentation [181]. First, we created a centerline path from the aortic valve to the apex of the LV and manually segmented the endocardial and epicardial boundaries. 2D segmentations were created at least every 1mm apart, with smaller spacing for regions showing significant changes in geometry. This process was performed at both end-diastole and peak-systole. We also segmented sternal shadowing artifacts to identify regions where strain could not be reliably calculated. Finally, 3D surface models of the endocardial, epicardial, and sternal artifact boundaries at both end-diastole and peak-systole were rendered with uniform meshing **(Fig. 6.1C)** and exported as STL files for further MATLAB analysis.

6.3.3.2 Assessment of Global Cardiac Function

The 3D surface models were converted to solid, volumetric meshes and spatially registered to the 4D ultrasound data. We calculated end-diastolic volume (EDV) and peak-systolic volume (PSV) by multiplying the number of voxels in the endocardial solid mesh at the corresponding time point by the isotropic voxel dimensions of the 4D data. These volumes were then used to evaluate global metrics of LV systolic function including stroke volume (SV), ejection fraction (EF), and cardiac output (CO), which were calculated as mentioned previously **(Eqs. 4.1-4.3)**. LV diastolic function was also assessed using transmitral flow velocity waveforms obtained from pulsed-wave Doppler. E- and A-wave peak velocities from five different cardiac cycles were measured, and their corresponding averages were used to calculate E/A ratio. We used the E/A ratio to identify whether blood flow into the LV was primarily driven by passive filling (pressure gradient caused by LV relaxation; E-wave) or active filling (atrial contraction; A-wave).

6.3.3.3 Estimation of 3D Maximum Principal Green-Lagrange Strain

We implemented a direct deformation estimation (DDE) algorithm in MATLAB to estimate the 3D deformation gradient tensor as described previously **(Fig. 6.1D**; [177]**)**. Briefly, we defined a rectangular coordinate grid spaced 5 pixels apart on the 4D ultrasound data. At each

grid intersection, an 11x11x11 investigation region was assigned. Using the image at end-diastole as a reference template, we iteratively optimized a warping function that best mapped the affine transformation of this region from the template image to a deformed image at the next timepoint. The warping function was optimized by best matching voxel intensities between the template and deformed image. The warping function was designed to be analogous to the 3D deformation gradient tensor, $\mathbf{F}_{3D}$, such that we could directly estimate $\mathbf{F}_{3D}$ during voxel intensity mapping. This process was repeated until $\mathbf{F}_{3D}$ was determined at each grid intersection *(i,j,k)* across all time points in the cardiac cycle. We then calculated the 3D Green-Lagrange (GL) strain tensor, $\mathbf{E}_{3D}$, as shown in **Eq. 6.1**, where **I** is the second order identity tensor.

$$\mathbf{E}_{3D}^{(i,j,k)} = \frac{1}{2}\left(\mathbf{F}_{3D}^{(i,j,k)^T}\mathbf{F}_{3D}^{(i,j,k)} - \mathbf{I}\right) \quad \textbf{(6.1)}$$

Finally, the maximum principal component of the 3D GL strain tensor was calculated and superimposed onto the 4D ultrasound data. 3D interpolation was performed to approximate strain values in regions between the coordinate grid points.

6.3.3.4 In Vivo Strain Comparison to Vic2D

In one animal, we compared strain values calculated from the 3D-DDE technique to those measured from Vic2D, a commercially available digital image correlation (DIC) software that has been previously used to quantify tissue strains from clinical images [182,183]. Briefly, representative short-axis slices of the LV were obtained from the isotropic 4D data at baseline and on days 1, 7, and 28 post-permanent ligation of the LCA. Myocardial strains were evaluated with Vic2D by manually selecting a region of interest around the LV wall (ring geometry; 21x21 investigation window, step = 1 pixel). The end-diastolic image was used as the reference configuration. The top 10% of the maximum principal strains were then averaged and compared between the Vic2D and 3D-DDE methods along the anterior and posterior walls of the LV.

6.3.3.5 Bullseye Mapping of Myocardial Strain

We created volumetric meshes of the myocardial wall by subtracting the rendered endocardial volumes from the epicardial volumes in order to visualize strain within the myocardium **(Fig. 6.1E)**. The mid-surface of the myocardium was obtained by calculating the midpoints between paired endocardial and epicardial boundary points located in a plane normal to

the centerline of the LV. We defined paired endocardial and epicardial boundary points as points aligned radially from the centerline of the LV. Myocardial strain values between paired endocardial and epicardial boundary points were averaged together to create a representative mean strain metric. The mid-surface of the myocardium was then unwrapped to polar coordinates, relative to the apex of the LV, to represent the averaged strain values as a bullseye map in accordance with the American Heart Association's 17-segment model **(Fig. 6.1F,** [184]**)**.

6.3.3.6 Noninvasive Estimation of Infarct Size

Two approaches to noninvasively estimate infarct size were performed. First, we used myocardial wall thickness at peak-systole as a criterion for determining infarct size. Wall thickness was calculated by measuring the distance between paired endocardial and epicardial boundary points along the LV. Regions with thickness values smaller than 0.5mm were defined to be infarcted as used by others [185]. We then quantified infarct size as the percentage of the myocardium with systolic thickness values below 0.5mm. Infarct size was reported as a percent of LV size to take into account ventricular dilation. This infarct sizing method was only applicable for mice with transmural infarcts (PL) and not for subepicardial infarcts (I/R).

In the second approach, strain profiles were used to estimate infarct size. We first plotted bullseye maps of principal 3D GL strain throughout the cardiac cycle. The maximum strain values at each spatial position were then extracted across all timepoints to construct a representative bullseye map. This step was implemented to account for dyssynchrony in LV contractile patterns in mice with ischemic injury. An initial estimate for infarct center was obtained from the center of the wall-thinned myocardium in the PL group. In the I/R group, which did not exhibit significant wall-thinning, we manually identified the center of low strain regions to identify the infarct center. Strain profiles were then plotted radially from the infarct center, and a sigmoidal fit was implemented across every 30° region **(Fig. 6.2A-B)**. The location of the inflection point was determined to be the boundary of the infarct zone, and spatial strain gradient at the infarct boundary was calculated from the slope of the linear portion of the sigmoidal curve fit. In regions with significant sternal artifacts where the inflection points could not be identified, infarct boundaries were approximated by interpolating adjacent infarct boundaries in polar coordinates. **(Fig. 6.2C)**. Infarct size was then reported as an area percentage in the myocardium that fell within the strain-estimated infarct boundary.

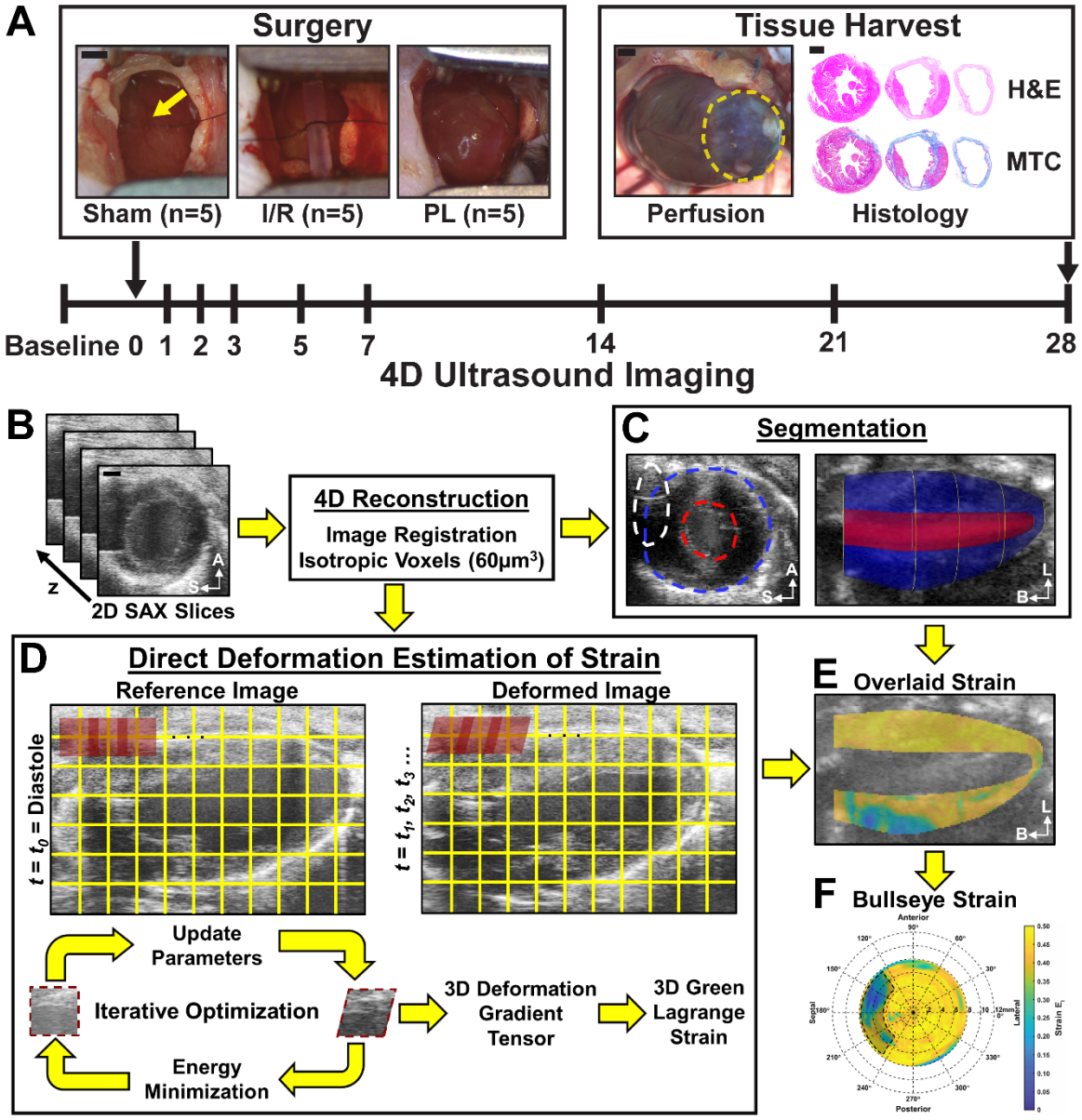

Fig. 6.1: Study design. **(A)** Fifteen adult, male mice were randomly assigned into 3 surgical groups: 1) sham-operated controls, 2) 30-min ischemia-reperfusion (I/R), and 3) permanent ligation (PL) of the left coronary artery (yellow arrow). A Vevo2100 ultrasound system was used to acquire 4D ultrasound data and flow information of the LV at baseline and on days 1, 2, 3, 5, 7, 14, 21, and 28 post-surgery. At the end of the study, the heart was stained with hematoxylin-eosin (H&E) and Masson's trichrome (MTC). Yellow dashed outlines highlight the infarcted myocardium. **(B)** We reconstructed 4D ultrasound data from ECG and respiratory-gated 2D short-axis ultrasound images of the LV. **(C)** 3D endocardial (red), epicardial (blue), and sternal artifact (white) boundaries were segmented at end-diastole and peak-systole. **(D)** Maximum principal 3D Green-Lagrange strain (E_1) was calculated using a direct deformation estimation technique. **(E)** Strain was then localized within the myocardium using segmented boundaries and presented as bullseye maps **(F)**. A: anterior, S: septal, L: lateral; B: base. Scalebar: 1mm.

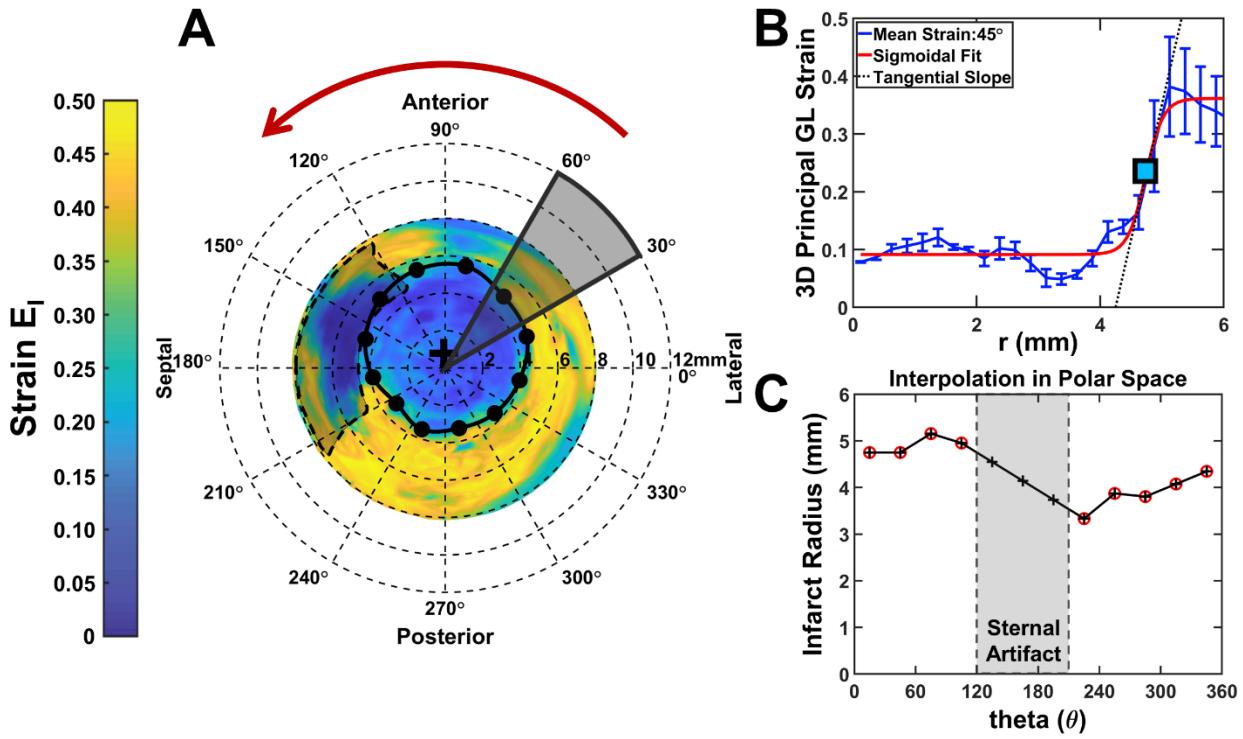

Fig. 6.2: Strain estimation of infarct size. **(A)** We extracted myocardial strain profiles radially from the infarct center (black crosshair) and performed sigmoidal fitting on strain profiles averaged across every 30° region. **(B)** The spatial positions of the inflection points (square box and black dots) are defined as the infarct border and unwrapped from the infarct center to estimate infarct boundaries in regions with sternal artifacts **(C)**. Infarct size is defined as the percentage of the myocardium that lies within the strain-estimated infarct boundary.

6.3.4 Histological Analysis

6.3.4.1 Tissue Preparation for Staining

At the end of the study, we euthanized the mice and perfused 30mM KCl solution to arrest the heart in diastole. Harvested hearts were then sliced to 3-4 uniform segments in short-axis and fixed in 4% paraformaldehyde for 7 days at 4°C before being sent for histology. Briefly, cardiac segments were paraffin-embedded, thin-sectioned (5µm), and stained with hematoxylin-eosin (H&E) and Masson's trichrome (MTC). MTC stain was used to differentiate muscle fibers (red) from collagen-rich scars (blue). We imaged stained tissues in segments at 10x magnification with a LEICA ICC50W stereomicroscope (Leica Microsystems Inc., Buffalo Grove, IL) and quantified collagen content and infarct size using ImageJ [186].

6.3.4.2 Collagen Quantification and Infarct Sizing

We stitched adjacent cardiac images from a representative slice using MosaicJ [187] and removed image background from the rendered image. MTC images were then separated into their RGB channels to isolate red pixels corresponding to muscle fibers from blue pixels representative of collagen-rich scars. Percent collagen was then calculated as shown in **Eq. 6.2**.

$$\% \text{ Collagen} = \frac{\text{\# blue pixels}}{\text{total \# of pixels}} \text{ x } 100 \quad \textbf{(6.2)}$$

We calculated infarct size from MTC images using a midline length approach [103]. The LV myocardial midline was traced in ImageJ by identifying the midpoints between the endocardial and epicardial boundaries. The midline circumference corresponds to the total midline length. The midline infarct length was measured as the midline arc length in regions where the collagen scar encompassed more than 20% of the myocardial thickness. This 20% threshold was used to represent infarct size in LVs with subepicardial infarcts in the I/R group. Infarct size (IS) was then calculated by dividing the sum of the midline infarct lengths, $l_{infarct}$, by the sum of the total midline length, $l_{total,}$ from all cross-sectional slices of the LV, n **(Eq. 6.3)**.

$$\text{IS} = \frac{\sum_{i=1}^{n} l_{infarct}}{\sum_{i=1}^{n} l_{total}} \text{ x } 100 \quad \textbf{(6.3)}$$

6.3.5 Statistical Analysis

All data were reported as mean ± standard deviation and tested for normality using the Shapiro-Wilk test. We implemented a log transformation on non-normal and heteroscedastic data before running statistical tests. A repeated measures analysis of variance (ANOVA) with post-hoc Tukey's test was performed to study the effects of surgery on cardiac function at the different time points. Similarly, we ran a two-way ANOVA with post-hoc Tukey's test to study the effects of spatial position and surgery on both maximum principal 3D GL strain and collagen content. Lastly, linear regression analyses comparing the different methods of infarct sizing were conducted. All statistical analyses were performed using GraphPad Prism version 8.1.1 (GraphPad Software, San Diego, CA) with $p<0.05$ representing statistical significance.

6.4 Results

6.4.1 Longitudinal Assessment of Cardiac Function

Long-axis ultrasound images of the LVs from three representative mice are presented at peak-systole in **Fig. 6.3A**, highlighting geometrical differences between surgical groups. A video of LV motion throughout the cardiac cycle is provided as supplemental material **(Fig. B.1)**. **Fig. 6.3A** shows that LV geometry was preserved in the sham group, while myocardial damage was evident in the I/R and PL groups as early as day 1. Akinetic regions, marked in dashed yellow lines, indicated that ischemic injury was primarily localized to the apex of these LVs. A closer inspection revealed that mice in the PL group experienced significant wall thinning and chamber dilation by day 7 post-surgery. We did not observe this trend in mice in the I/R group.

These findings reflected longitudinal changes in global cardiac function **(Fig. 6.3B-G)**. Although all cardiac parameters remained unaffected in the sham group over the course of 28 days, we identified detrimental changes in LV function in the I/R and PL groups. The LVs of mice in the PL group progressively dilated post-surgery until they reached EDVs close to triple that of the sham group at day 28 (EDV_{Sham} = 53±2µL vs. EDV_{PL} = 151±39µL, p<0.01). Interestingly, minimal dilation was observed in the I/R group when compared to the sham group ($EDV_{I/R}$ = 68±8µL, p=0.02). Reductions in LV contractile function due to ischemic injury were detected from day 1 as increases in PSVs that either remained stable in the I/R group or increased proportionally to LV dilation in the PL group (PSV_{Sham} = 18±2µL vs. $PSV_{I/R}$ = 34±9µL, p<0.01; vs. PSV_{PL} = 119±46µL, p<0.01). These resulted in immediate and significant decreases in EFs that remained depressed throughout the study (EF_{Sham} = 66±3% vs. $EF_{I/R}$ = 50±7%, p<0.01; vs. EF_{PL} = 23±12%, p<0.01). Surprisingly, we noticed transient reductions in SV and CO 7 days post-surgery before both returned to baseline values. In addition to compromised systolic function, we also observed significant diastolic dysfunction in the PL group that was not seen in the I/R group (E/A_{Sham} = 1.5±0.3 vs. $E/A_{I/R}$ = 1.3±0.2, p=0.59; vs. E/A_{PL} = 0.5±0.4, p=0.04). Taken together, these results revealed that mice exposed to I/R injuries exhibited smaller degrees of LV remodeling than those subjected to permanent LCA ligation.

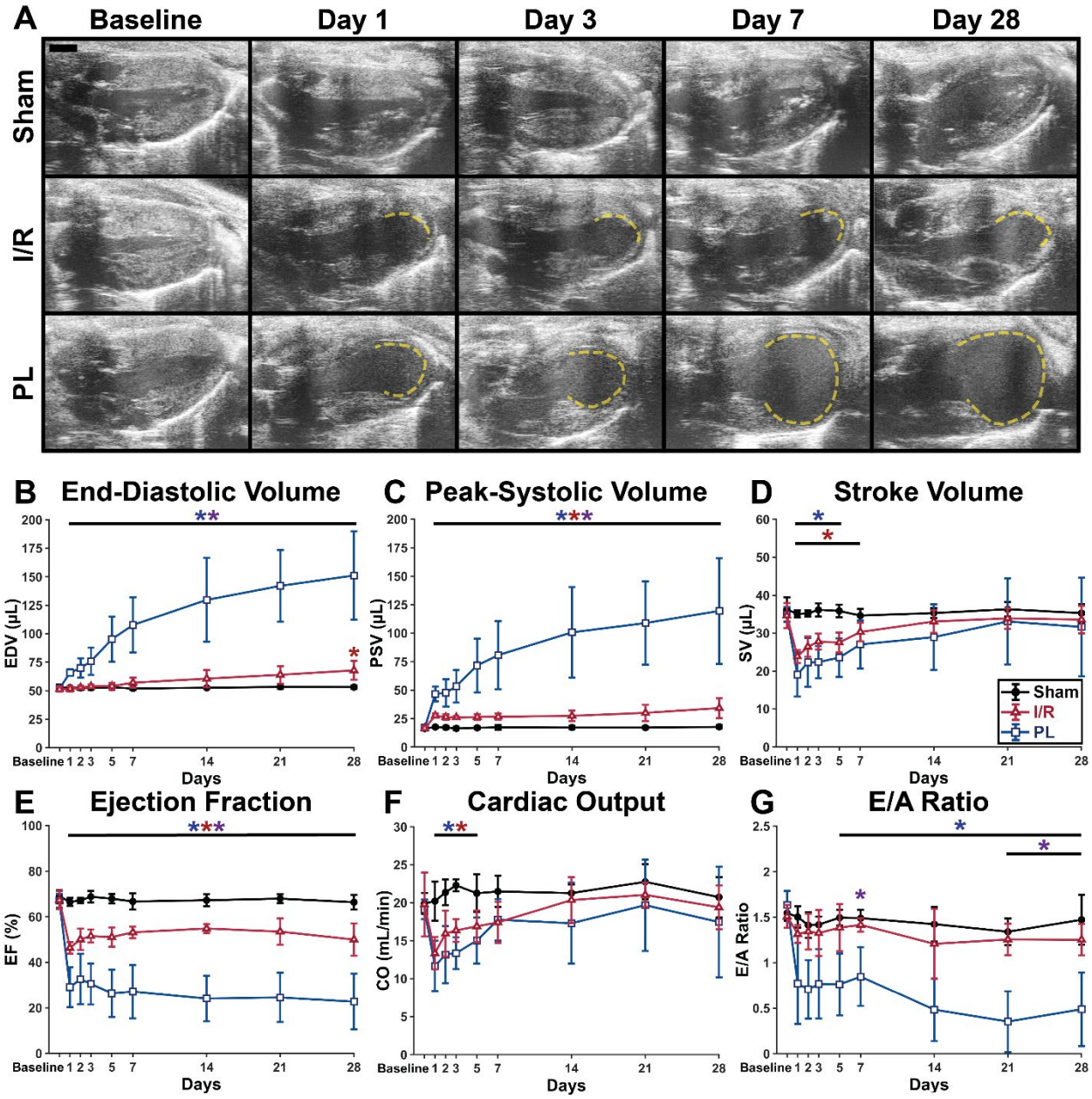

Fig. 6.3: LV remodeling post-infarction. **(A)** Representative long-axis ultrasound images of mouse LVs taken at peak-systole. Akinetic myocardial walls, indicative of ischemic damage, are outlined in dashed yellow lines. Global metrics of LV function **(B-G)** showed that mice in both I/R and PL groups exhibited significant reductions in LV contractile function post-surgery, but significant dilation and diastolic dysfunction were only consistently measured in the PL group. Taken together, mice in the PL group experienced greater degrees of cardiac remodeling when compared to those in the I/R group. Data are shown as mean ± standard deviations (*p<0.05). I/R: ischemia-reperfusion, PL: permanent ligation. Blue asterisks: PL vs. Sham; Red asterisks: I/R vs. Sham; Purple asterisks: PL vs. I/R. Scalebar: 1mm.

6.4.2 Spatial Distribution of 3D Myocardial Strain

Longitudinal changes in peak-systolic LV geometries and endocardial wall strains from three representative mice are shown in **Fig. 6.4**. Maximum principal 3D GL strain ($\mathbf{E_I}$) of the endocardial wall was visualized along the anterior and posterior walls of the LV to highlight regional differences in strain, with yellow and blue regions corresponding to areas of high and low strains respectively. Bullseye plots mapping the peak myocardial strain profiles of the unwrapped LV surface are shown in **Fig. 6.5**, with video representations of day 28 LVs portrayed throughout the cardiac cycle in supplemental material **Fig. B.2**. Sternal shadowing artifacts, commonly found near the base of the LV and marked as dashed black lines, artificially lowered strain values in these regions and were excluded from our analysis. Taken together, **Figs. 6.4-6.5** illustrate that regions of low strains near the LV apex remained localized in the I/R group but continued to expand proportionally to chamber dilation in the PL group. Furthermore, LV wall thinning was only observed in the PL group, and wall-thinned boundaries continued to expand throughout remodeling, approaching infarct boundaries estimated from the strain profile inflection points.

Representative day 28 long-axis ultrasound images, 3D surface strains, and bullseye strain maps of the remodeled LVs for all mice in the I/R and PL groups are included as supplemental figures **(Figs. B.3-B.4)**. Day 28 strains along the entire thickness of the LV wall are also provided for one representative mouse in each surgical group in supplemental **Fig. B.5**. These supplemental figures highlight substantial heterogeneity in LV remodeling across mice both within and between groups. However, clear patterns are present, and we noticed that most mice exhibited asymmetrical infarcts skewed towards the anterior wall. Lastly, a comparison of maximum principal strain values between the 3D-DDE and Vic2D methods is summarized in supplemental **Fig. B.6** for a representative LV with an asymmetrical anterior infarct. Although both techniques successfully captured strain reductions along the infarcted anterior wall when compared to the contractile posterior wall, the 3D-DDE algorithm more appropriately tracked changes in LV boundaries throughout a representative heartbeat, as strain values returned to 0 at end of the cardiac cycle.

Interestingly, we identified significant differences in maximum principal 3D GL strain values within the infarcted myocardium between mice in the I/R and PL groups. Strain profiles averaged across all five mice in each surgical group are shown in **Fig. 6.6A-E**. Throughout the 28 days following surgery, we consistently observed a sigmoidal strain profile at the interface between infarcted and remote myocardium. We also detected significantly higher strain values

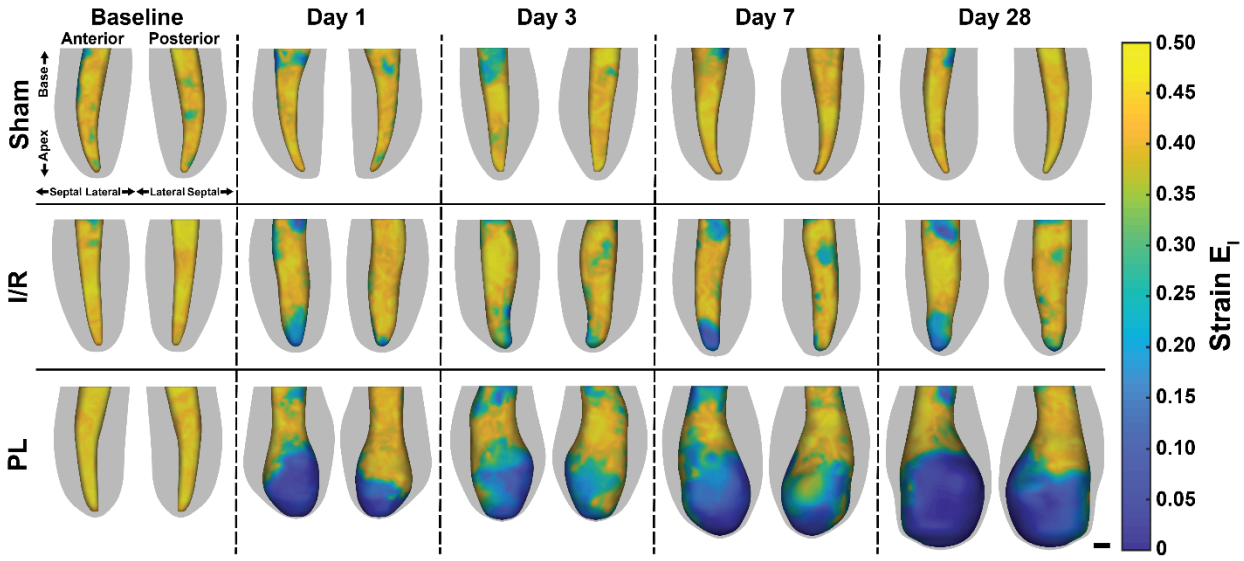

Fig. 6.4: Longitudinal 3D representations of peak-systolic LV boundaries with maximum principal 3D Green-Lagrange myocardial strains (E_I) overlaid onto the endocardial wall. Epicardial boundaries are shown in gray. Dark blue areas highlight akinetic regions of the myocardium. Scalebar: 1mm.

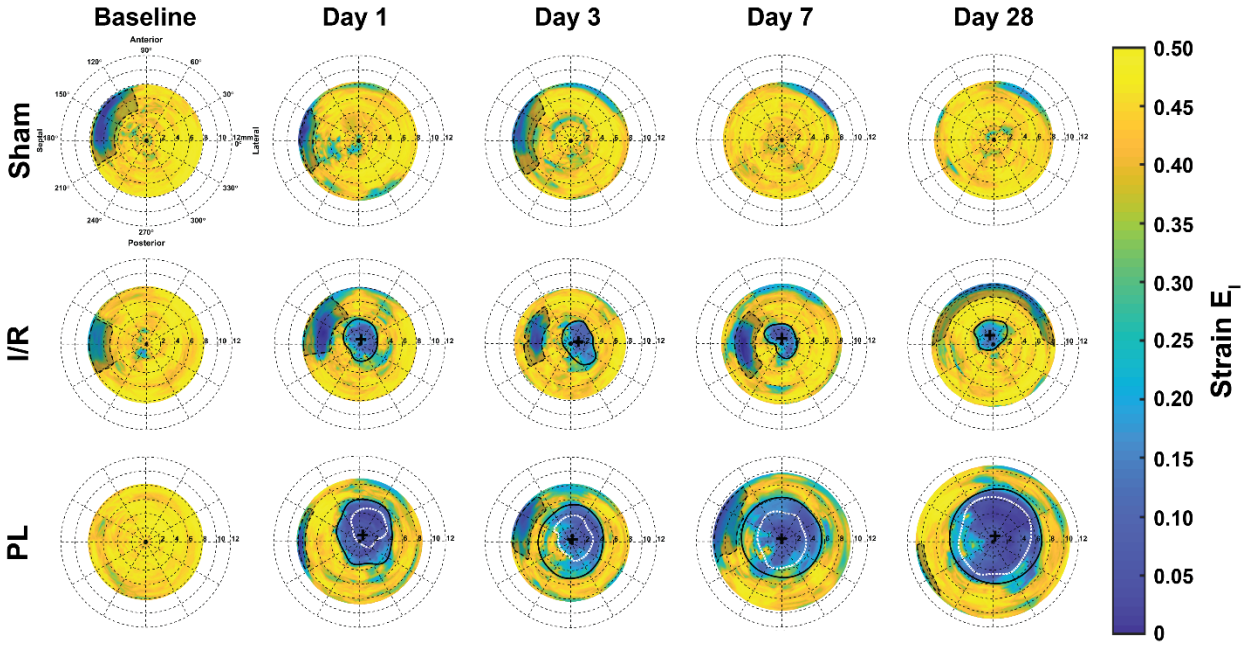

Fig. 6.5: Longitudinal bullseye maps of the maximum principal 3D Green-Lagrange strain (E_I) within the myocardium. Strain-estimated infarct boundaries are outlined in solid black lines with infarct centers marked as black crosshairs. Wall-thinned infarct boundaries measured from segmentation are outlined as white dotted lines, while sternal artifacts are outlined as black dashed lines.

within the infarcted myocardium of mice in the I/R group when compared to those in the PL group (Day 28: $E_{Infarct,I/R}$ = 0.22±0.10 vs. $E_{Infarct,PL}$ = 0.09±0.03, p=0.01), while sham-operated mice maintained healthy strain values in the LV apex ($E_{Apex,Sham}$ = 0.40±0.03). Conversely, no differences in strain were seen in the remote myocardium between the three groups ($E_{Base,Sham}$ = 0.41±0.03 vs. $E_{Remote,I/R}$ = 0.42±0.02, p=0.97; vs. $E_{Remote,PL}$ = 0.40±0.02, p=0.95). We observed no differences in the spatial strain gradient at the infarct boundary between the I/R and PL groups across all time points **(Fig. 6.6F)**.

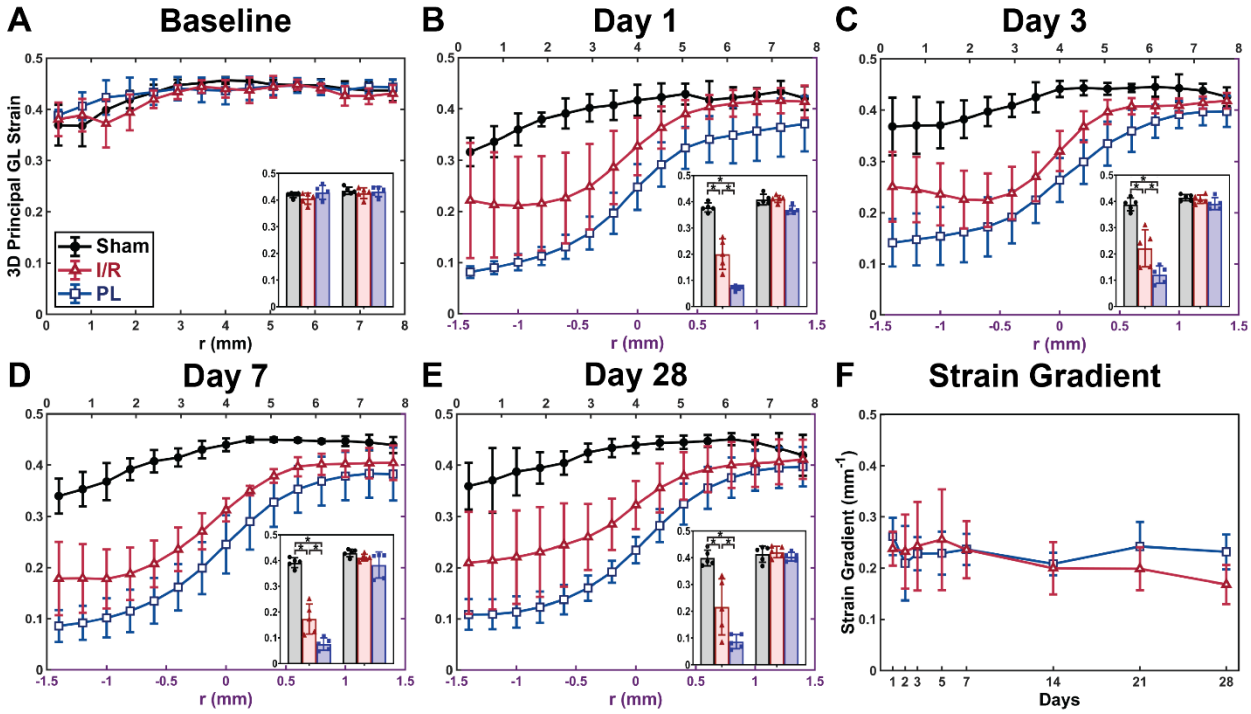

Fig. 6.6: Myocardial strain profiles of the remodeling LVs averaged across mice in each group and plotted at **(A)** baseline and **(B-E)** on days 1, 3, 7, and 28 post-surgery. Strain profiles in nonischemic mice (baseline and sham) are plotted radially away from the LV apex (black x-axis). In ischemic mice, strain profiles are plotted only in regions near infarct boundaries (r = 0; purple x-axis). Strain values averaged within the infarcted and remote myocardium are shown as the left and right inset bar graphs respectively. **(F)** Strain gradients, calculated within the linear component of the sigmoidal fit from the strain profiles, did not show significant changes between surgical groups over the 28-day period. Data are shown as mean ± standard deviations (*p<0.05).

6.4.3 Histological Analysis of Collagen Content and Infarct Size

Representative histology images of mouse LVs stained with MTC revealed varying distributions of collagen-rich, fibrotic (blue) tissues between surgical groups **(Fig. 6.7A-B)**. The absence of fibrosis within the myocardium of sham-operated mice demonstrated that sham surgeries contributed little to no myocardial damage. Significant scarring, however, was observed in both the I/R and PL groups (percent collagen: $Sham_{Apex}$ = 3±2% vs. I/R_{Apex} = 15±8%, p<0.01; vs. PL_{Apex} = 38±17%, p<0.01). While mice in the PL group developed transmural infarcts, as shown by the presence of collagen spanning the entire thickness of the myocardium, mice in the I/R group interestingly only developed subepicardial scarring. We also noticed an increase in interstitial collagen percentage towards the infarcted apex (percent collagen: $base_{PL}$ = 7±3% vs. $mid\text{-}papillary_{PL}$ = 23±6%, p<0.01; vs. $apex_{PL}$ = 38±17%, p<0.01). Finally, we compared infarct sizes estimated from 3D strain maps with those calculated from histology and discovered a strong correlation between the two approaches (**Fig. 6.7C**; R^2 = 0.93, p<0.01).

6.4.4 Correlation of Infarct Size

Correlation plots comparing infarct sizes (IS) estimated from three different approaches are summarized in **Fig. 6.8A-C**. Although we found a strong positive correlation between all methods (R^2 > 0.80, p<0.05), infarct sizes evaluated from histological staining at day 28 were better correlated with strain-estimated infarct sizes (R^2 = 0.95) than those measured from wall-thinning (R^2 = 0.83). Similarly, a stronger negative correlation between strain-estimated infarct size and ejection fraction (R^2 = 0.69; **Fig. 6.8D**) was observed, while infarct size approximated from wall-thinned regions exhibited only moderate correlation with ejection fraction (R^2 = 0.41; **Fig. 6.8E**). Interestingly, we identified significant differences in measured infarct size between the strain-estimated and wall-thinned approaches between days 1-3 post-surgery (p<0.05) which appeared to converge throughout cardiac remodeling **(Fig. 6.8F)**.

6.5 Discussion

We have demonstrated in two mouse models of myocardial infarction that DDE, in conjunction with 4D ultrasound, provides regional *in vivo* estimates of 3D myocardial strain. Unlike 2D techniques, regional strain mapping not only helps explain the observed decrease in

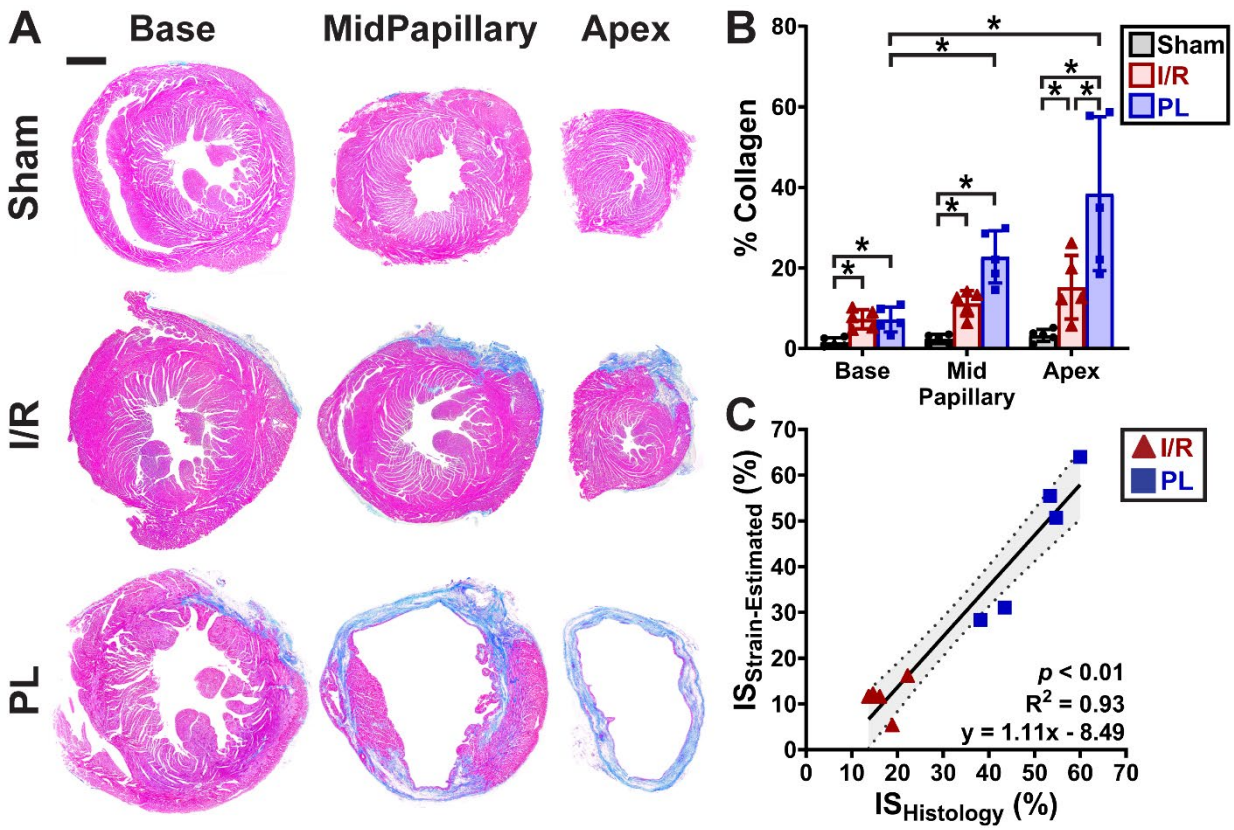

Fig. 6.7: Histological analysis of collagen content and infarct size. **(A)** Histology images of mouse LVs, obtained 28 days post-surgery and stained with Masson's Trichrome, revealed subepicardial scarring in the I/R group and transmural infarcts in the PL group. Muscle fibers are stained red while collagen-rich scars are stained blue. **(B)** Bar graphs showing percent collagen highlighted spatial variations in collagen content relative to infarct location. **(C)** Strain-estimated infarct size strongly correlated to infarct size measured from the histological midline length approach. Data are shown as mean ± standard deviations (*p<0.05). Scalebar: 1mm.

global LV function post-injury, but also reveals the importance of strain profiles in driving infarct expansion. Specifically, mice exhibiting higher strain values within infarcted tissue experienced smaller degrees of LV remodeling. Furthermore, our initial myocardial 3D maximum principal strain maps predicted final infarct size four weeks after ischemic injury. Taken together, these strain data help characterize the role that mechanical strain plays in LV remodeling post-infarction.

6.5.1 Advantages of Direct 3D Strain Estimation

A significant advantage of the 3D-DDE technique is its ability to capture regional strain differences along the entire thickness of the myocardium **(Fig. B.5)**. Most preclinical [169,171,172]

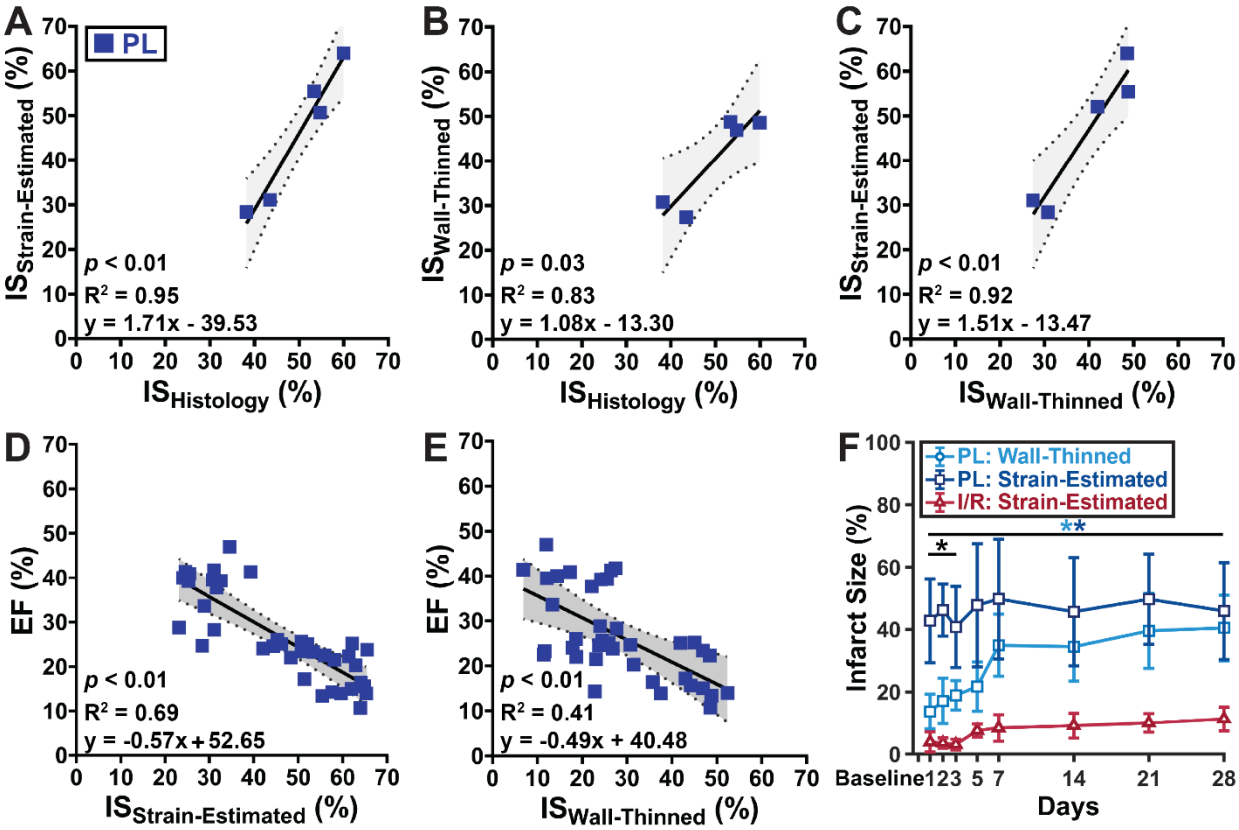

Fig. 6.8: Correlation of varying infarct sizing techniques with cardiac function. **(A-C)** Correlation plots comparing three different infarct sizing methodologies showed that the proposed strain-estimation technique best correlated with gold-standard histological estimation of infarct size. Correlation of **(D)** strain-estimated and **(E)** wall-thinned infarct size with ejection fraction. Linear regression lines are shown as solid black lines with 95% confidence intervals shaded in gray. **(F)** Line graphs summarizing infarct size growth throughout cardiac remodeling. Data are shown as mean ± standard deviations (*p<0.05). Light blue asterisks: wall-thinned PL vs. strain-estimated I/R; Dark blue asterisks: strain-estimated PL vs. strain-estimated I/R; Black asterisks: wall-thinned PL vs. strain-estimated PL.

and clinical [90,175] ultrasound studies to date rely on commercially available ultrasound software packages to estimate 2D myocardial strain (ε) as mentioned previously in **Eq. 2.1**. The observed change in length, either in the circumferential, longitudinal, or radial direction, is measured by tracking the endocardial and epicardial LV boundaries throughout the entire cardiac cycle using speckle-tracking algorithms. Since a simple change in length is used to approximate strain within large subregions, this approach cannot resolve regional strain differences within the myocardium. This linear approximation also does not consider the nonlinear components of strain and is only appropriate when estimating small deformations less than 5% [66]. This is not the case in many

soft tissues, such as the heart, where large deformations are observed *in vivo*. Finally, as the heart undergoes twisting during systolic contraction, 2D techniques are negatively impacted by through-plane motion [90]. By directly estimating 3D deformation gradient tensor from small image subregions within 4D ultrasound data, these issues can be mitigated.

Another advantage of the presented technique lies in its ability to yield reproducible measures of 3D strain. Unlike existing techniques, which often rely on displacement regularization prior to strain estimation, the DDE method estimates 3D deformation gradient tensor directly during voxel intensity mapping as reported previously [177]. This results in a noise-insensitive algorithm that provides a more accurate and precise strain field estimation when compared to displacement-based methods, as supported by *in silico* validation [177]. We demonstrate the reproducibility of our 3D strain measurements in supplemental **Fig. B.7**, which highlights similarities in the bullseye strain maps of all 15 healthy mice imaged at baseline. In all cases, we found high strain values ranging between 0.40-0.45 throughout the LV myocardium, except in regions with prominent sternal artifacts. This suggest that across animals, we are consistently obtaining reproducible values of strain. Additionally, the fact that we observed 1) a consistent sigmoidal behavior between the infarct and remote regions with similar strain values in these regions **(Fig. 6.6)** and 2) reported a consistent strain-estimated infarct size for each animal at the same location **(Fig. 6.5** and **Fig. 6.8F)** throughout disease progression further demonstrate the reproducibility of the technique. Taken together, these data suggest that if sternal artifacts are minimized or avoided during image acquisition, 3D myocardial strain in remodeling LV can be reliably quantified.

6.5.2 3D Strain Map Reveals Myocardial Tissue Heterogeneity

Through our 3D approach, we can identify regional variations in strain values and profiles that compare well to previously published results. Many 2D ultrasound studies have reported significant decreases in global myocardial strains in mice subjected to infarction, with the remote myocardium exhibiting significantly higher strains than the infarcted tissue [89,169,171]. In the radial direction, where the largest deformation is observed [68], strain values range between 25-40% in the healthy myocardium but drop to less than 15% within the infarct [169,171]. Our 3D strain results are consistent with these findings **(Figs. 6.6A-E)**. Furthermore, a short-axis

comparison of maximum principal strains between the presented 3D-DDE technique and Vic2D yielded similar ranges of strain values **(Fig. B.6)**.

Although LV kinematics in the remote and infarct zones have been widely studied, the interface between these regions remains to be fully characterized as previous work has only described intermediate strain values in this vulnerable border zone [89,172]. Unsurprisingly, given the original ultrasound data, heterogeneity in border zone strain patterns can be identified in the reconstructed 3D strain maps **(Figs. 6.4-6.5, B.2-B.5)**. These strain patterns are correlated with complex, nonuniform deposition of collagen along LV wall, clearly visualized from histological staining of the midpapillary level of the LV in the PL group **(Fig. 7A)**. Indeed, collagen fiber orientations are remarkably heterogeneous in the healing myocardial scar and likely influence the mechanical properties of the infarct border zone [188,189]. Taken together, capturing strain heterogeneity within the infarct border zone early in remodeling may provide important insights into the role of strain in infarct expansion and LV remodeling.

6.5.3 Correlation Between Strain Profiles and LV Remodeling Severity

Strain profiles near infarct border zones exhibit a unique sigmoidal behavior **(Fig. 6.6A-E)**, likely caused by a spatial decrease in collagen content away from the infarct **(Fig. 6.7A-B)**. Interestingly, throughout the 28 days post-infarction, we found significantly higher strain values within the infarcted myocardium of mice in the I/R group when compared to those in the PL group **(Fig. 6.6B-E)**. A sustained increase in strain within the infarct zone may suggest either a higher percentage of viable cardiomyocytes or an improved scar contractile function attributed to the mechanoregulation of myofibroblast activity [167,190]. Within the damaged myocardium, these elevated strains may be a unique characteristic of small infarcts, but further investigation is necessary to determine its role on infarct expansion during early remodeling. Indeed, we measured significant improvements in both systolic and diastolic LV functions **(Fig. 6.3B-G)**, as well as significantly smaller final infarct sizes **(Fig. 6.7C)**, in the I/R group compared to the PL group. Although direct regional strain comparisons between mice subjected to I/R and PL surgeries have yet to be conducted within a single study, our results closely match findings from existing ultrasound studies, which report a significant increase in infarct size and worse remodeling outcomes with prolonged ischemic durations [191,192].

6.5.4 Strain Profiles Provide Early Estimates of Infarct Size

A key discovery from this study is the propensity for wall-thinned myocardial regions at early stages to expand towards the strain-estimated infarct boundaries **(Fig. 6.5** and **Fig. 6.8F)**. Wall thinning is generally accepted to be the final product of infarct healing, and although the majority of wall thinning in murine models occurs within the first week, this gradual process may continue to take place up to a month post-infarction [14,193]. Additionally, wall thinning is often used to monitor infarct expansion *in vivo* [14], is primarily responsible for LV rupture [193], and directly impacts both systolic and diastolic function [167]. Thus, the ability to early predict the extent of wall thinning noninvasively may provide critical insights into LV remodeling and progression to heart failure.

Our data suggest that the damaged area with compromised 3D maximum principal strain values is predictive of final infarct size as early as day one. As the strain-estimated infarct size in the PL group remained unchanged throughout ventricular remodeling, rapid expansion of wall-thinned regions was prevalent within the first week before converging with the strain-estimated infarct border **(Fig. 6.8F)**. Other previous work similarly reported that changes in 2D myocardial principal strain also precede LV wall thinning in a genetic mouse model of dilated cardiomyopathy [194]. A potential explanation for this observation may be related to the creation of a stiff provisional matrix in the ischemic region early in remodeling which facilitates the gradual formation of collagen-rich scars. As nonviable cardiomyocytes are resorbed, a provisional granulation tissue rich in fibrin, laminin, and glycosaminoglycans are quickly formed to provide the LV with temporary structural support [14]. In the presence of a stiff extracellular matrix (ECM), transforming growth factor beta (TGF-β) is released from the latent-associated peptide complex due to increased mechanical resistance to cell tension [23]. TGF-β then promotes the differentiation of cardiac fibroblasts to myofibroblasts, which gradually replace the provisional structure with collagen-rich infarct tissue [14,23]. Thus, the presence of necrotic cardiomyocytes and a stiff provisional structure are likely detected as an immediate decrease in strain values one day after infarction **(Figs. 6.4-6.5)**. As these regions eventually become collagen-rich scars, a process that take several days or weeks to fully develop, the initial changes in myocardial ECM may explain why early strain-estimated infarct size remains unchanged throughout disease progression and is predictive of final infarct size **(Fig. 6.8F)**.

Our comparison of day 28 infarct sizes calculated from three different approaches revealed that gold-standard histology infarct size is best correlated to strain-estimated infarct size **(Fig 6.8A-C)**. Furthermore, we observed a better correlation with ejection fraction for the strain-estimated infarct size when compared to the wall-thinned approach ($R^2 = 0.69$ vs. $R^2 = 0.41$). These findings indicate that 3D principal strain profiles can be used to accurately predict final infarct size in rodents and may have similar utility in humans. This discovery is impactful because it presents a novel noninvasive method of estimating infarct size without the use of contrast agents or tissue collection. Previously, infarct size can only be reliably estimated using late-gadolinium enhanced MRI [179] or *ex vivo* histological staining [103].

6.5.5 Limitations

One major limitation of this study is the impact of image quality on strain estimation. Since the 3D-DDE algorithm is a direct image-based approach, shadowing artifacts can affect the measured strain values. As mentioned previously, sternal shadowing artifacts commonly found near the base of the LV resulted in underestimation of strains. Although we addressed this problem by removing these regions from our final strain analysis, care during data acquisition to minimize shadowing artifacts is needed. Another limitation is the computational time needed for the strain analysis. Due to the large number of investigation regions and need to spatially resolve small differences between timepoints, the strain analysis requires 2-3 hours to complete per dataset. It is important, however, to note that a tradeoff exists between processing times and the desired spatial resolution of the analyzed strain. In other words, if less refined strain maps are needed, the computational costs would be reduced dramatically. Lastly, surgical inductions of myocardial ischemia in mice are not true reflections of the gradual series of events leading up to a heart attack in humans. Mice experience smaller increases in collagen content post-MI [193] and undergo substantially faster infarct healing than typically observed in patients [14], which may lead to species-differences in the LV remodeling process. Beyond mice, however, similar strain mapping and profiling techniques could be applied to 4D ultrasound data acquired from other rodents, large animals, and humans.

Although the presented study focused on characterizing changes in 3D maximum principal strain, it is important to note that other metrics including the 2nd and 3rd principal strains, as well as principal strain direction, may provide additional insights into the remodeling process. A

previous study using tagged MR imaging of the porcine LV showed significant reductions in all three components of principal strains post-infarction [195]. Regional differences in principal strain directions were also detected; notably, maximum principal strain angles rotated away from the radial direction within the infarcted myocardium and its surrounding region. Future work will be needed to fully characterize the relationship between infarct expansion, principal strain directionality, and other components of the 3D strain tensor.

6.6 Conclusion

In summary, we have demonstrated a novel and robust approach to noninvasively quantify 3D myocardial strain. By integrating 4D ultrasound with a 3D-DDE technique, we expanded existing 2D ultrasound strain studies to 3D to better characterize the role of myocardial mechanics in disease progression. To the best of our knowledge, this study is the first demonstration of the use of 4D ultrasound to quantify 3D strain in order to characterize regional differences, instead of global changes, between two murine models with different infarct severities. By reconstructing 3D strain maps of the LVs, we were able to capture strain heterogeneity and characterize the sigmoidal strain profile at infarct border zones. We discovered that mice undergoing mild LV remodeling had significantly higher strain values within the infarcted tissue when compared to those with severe remodeling, suggesting that a more contractile infarct scar may be a unique characteristic of small infarcts. Finally, we described a new method to noninvasively estimate and predict final infarct size, without the use of contrast agents, at an acute phase based on 3D strain maps. Taken together, the findings presented in this study highlight the importance of 3D strain when studying how the mechanical behavior of the LV near infarct border zones contributes to post-infarction remodeling. Future work will be needed to investigate if the presented technique can be used to better characterize the role of 3D strains in infarct expansion, infarct extension, and in cases of multiple infarcts.

Ethics. The presented study was conducted in accordance with Purdue University's ethical guidelines regarding the use of animals in research. All surgical procedures have been approved by the Purdue Animal Care and Use Committee under protocol number 1505001246.

Acknowledgements. The authors would like to thank Drs. John Boyle, Guy Genin, and Stavros Thomopoulos for their feedback on the strain code development. We would also like to thank Dr. Kristiina Aasa, Stephen Buttars, and Andrew Needles at FUJIFILM VisualSonics Inc. for their technical assistance with the Vevo2100 ultrasound system.

7. CONTRIBUTIONS TO SCIENTIFIC KNOWLEDGE

7.1 Overview and Impact of Research Findings

In this dissertation, we have demonstrated that the development of 4D ultrasound is invaluable in monitoring patient-specific LV remodeling post-infarction, as these data provide full information on the geometries and kinematics of the continuously remodeling structure. By building 3D models of the LV, we can directly evaluate cardiac function without the need for geometrical assumptions and identify features that may go unnoticed with conventional 2D techniques. In fact, we have shown through a rigorous analysis that our 4D measurements significantly improved the assessment of cardiovascular health.

We also discussed how our 3D-DDE algorithm outperforms commonly used displacement-based strain methods. By calculating deformation gradient tensors directly from optimized image warping functions, we can circumvent the need to take numerical gradients of noisy displacement fields before estimating strain, improving the accuracy of the 3D-DDE method as validated *in silico*. The ability to accurately quantify and detect regional strain differences *in vivo* is a pressing need in the study of LV remodeling, where the mechanical properties of infarcted tissue contribute to its expansion and remodeling outcomes.

Therefore, by integrating our two recently developed technologies, we can now explore the role that myocardial mechanics play in LV remodeling post-infarction. To the best of our knowledge, this dissertation presents the first thorough longitudinal study where 4D ultrasound data is used to quantify regional differences, instead of global changes, in 3D myocardial strain between two murine models with different infarct severities. By spatially mapping the maximum principal 3D Green-Lagrange strain fields to animal-specific LV geometries, we were able to investigate how early changes in myocardial strain correlated with structural remodeling outcomes, such as wall-thinning, LV dilation, and final infarct size. Notably, we were able to capture significant strain heterogeneity and characterize the sigmoidal strain profile at infarct border zones. We discovered that mice undergoing mild LV remodeling had significantly higher strain values within the infarcted tissue when compared to those with severe remodeling, suggesting that a more contractile infarct scar may be a unique characteristic of small infarcts. Finally, we described a new method to noninvasively estimate and predict final infarct size, without the use of contrast

agents, at an acute phase based on 3D strain maps. Taken together, the findings of this dissertation have significant impact to the scientific community, as the ability to establish early metrics for the prediction of post-infarction remodeling outcomes may allow physicians to identify patients at high-risk of developing heart failure and better manage treatment.

7.2 Directions for Future Research

Future work can expand upon the technologies and findings presented in this dissertation to better understand the LV remodeling process post-infarction. The first principal component of the 3D Green-Lagrange strain tensor reported here is certainly an important but nonetheless simplified perspective of LV mechanics. An in-depth analysis investigating other strain components, such as the shear, 2^{nd}, and 3^{rd} principal components of strain, may provide further insight into the role of mechanics in infarct expansion. A study looking at how the heterogeneity of collagen orientation in the healing infarct scars influence its development and impact strain measurements may also be interesting. Finally, although this dissertation focuses on characterizing the role of myocardial mechanics, many other properties of the myocardium can influence LV remodeling outcomes post-infarction. An investigation into the oxygenation state of the myocardium to monitor collateral vessel formation, or perhaps understanding how spatial variations in the electrical activity of the infarcted LV affects contractility may provide more insights into the complex remodeling process that occur post-infarction.

APPENDIX A. SUPPLEMENTAL DATA TO CHAPTER 4

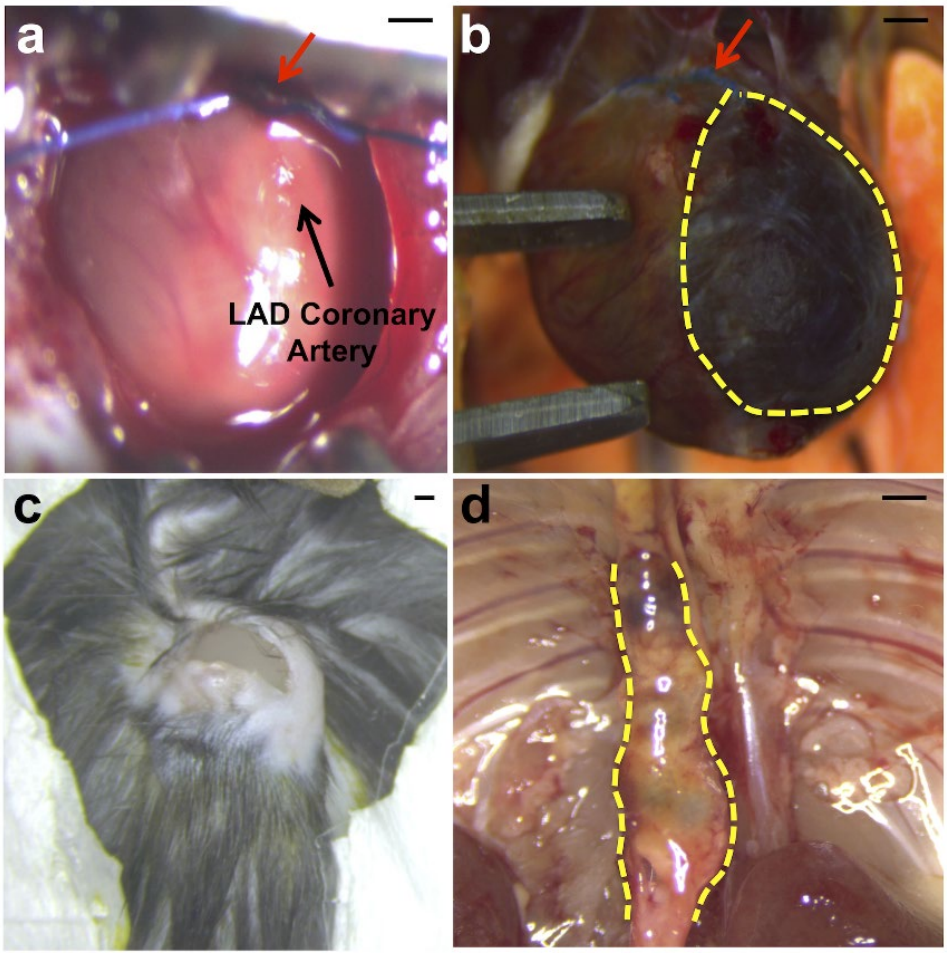

Fig. A.1: Surgical procedures and confirmation of disease states. **(a)** The left anterior-descending (LAD) coronary artery (black arrow) was permanently ligated with 8-0 sutures (red arrows) to induce myocardial infarction in mice. **(b)** A representative *in situ* image of a left ventricle, acquired 4 weeks post-LAD ligation, showed a large area of necrotic, infarcted myocardium outlined in dashed-yellow lines. **(c)** Mini-osmotic pumps containing angiotensin-II were implanted subcutaneously in apolipoprotein-E deficient mice to induce dissecting aneurysms in the abdominal aorta. **(d)** A representative *in situ* image of a mouse abdominal aorta, acquired 2 weeks post-aneurysm formation, showed a dissecting aneurysm outlined in dashed-yellow lines. Scalebar = 1mm.

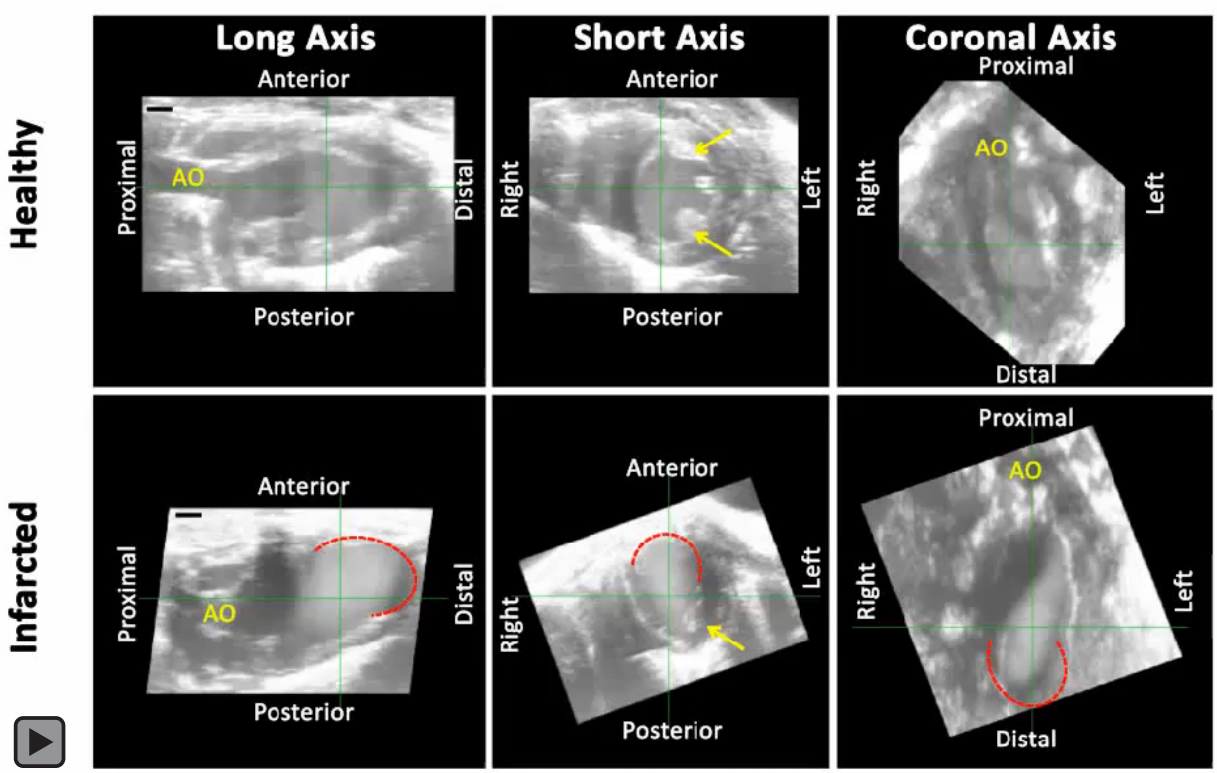

Fig. A.2: A three-axis view cine loop of a healthy mouse left ventricle **(top)** and a left ventricle with an anterior apical infarct **(bottom)**. Ultrasound images of the remodeled and infarcted left ventricle were obtained four-weeks post-coronary artery ligation. Note that the infarcted and necrotic myocardial tissue, outlined in red, exhibits akinesia and is associated with wall thinning. Papillary muscles are clearly seen in the short-axis view as extensions into the lumen (yellow arrows) with green crosshairs highlighting the center of the visualized structure. AO = aortic outflow. Scalebar = 1mm.

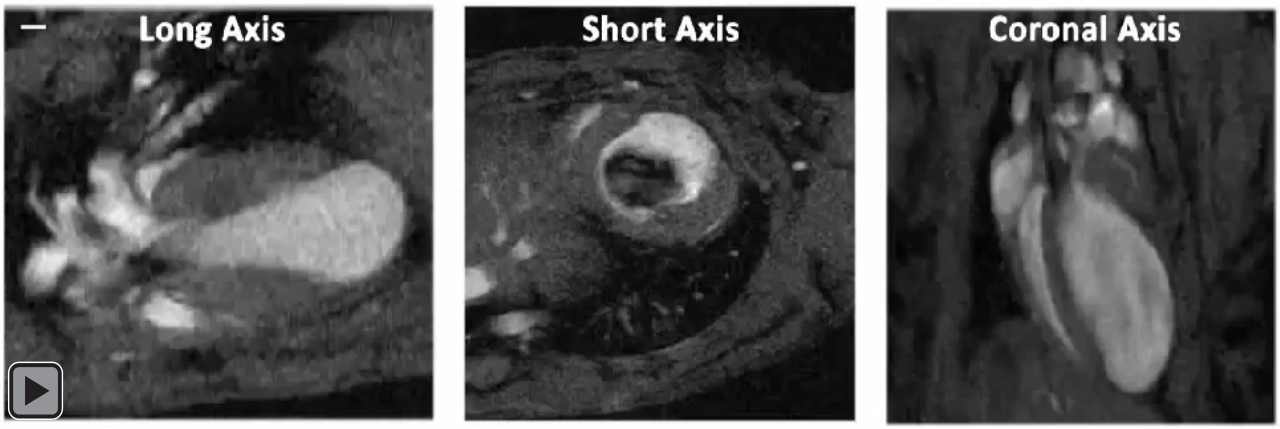

Fig. A.3: A three-axis view MRI cine loop of a mouse left ventricle with a four weeks old anterior apical infarct. Scalebar = 1mm.

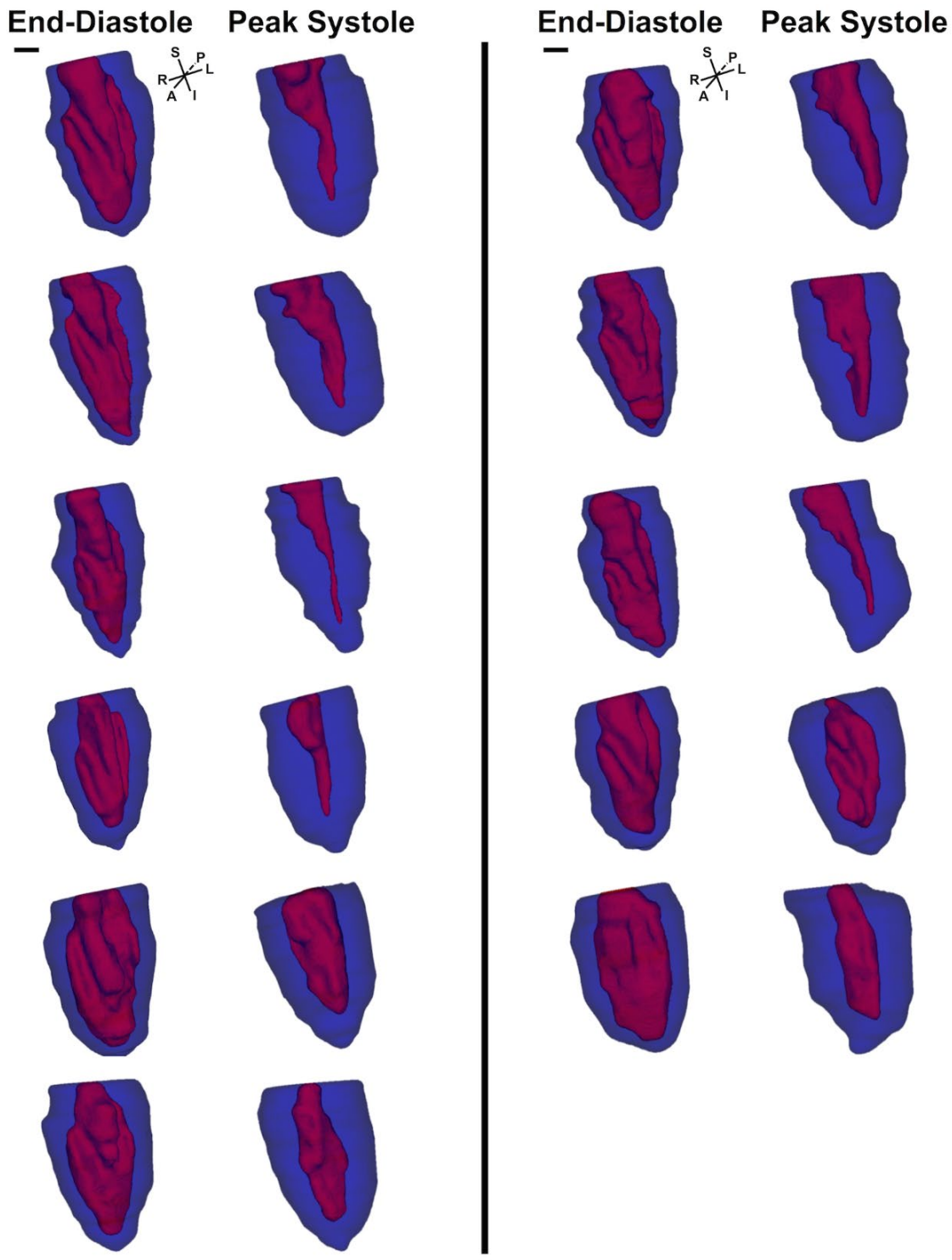

Fig. A.4: 3D renderings of the left ventricular lumen (red) and myocardial wall (blue) of healthy mice hearts, shown at end-diastole and peak-systole, demonstrate that each mouse heart has its own unique geometries (*n*=11). Papillary muscles can be clearly observed as indentations in the lumen. S = superior; I = inferior, P = posterior, A = anterior, R = right; L = left. Scalebar = 1mm.

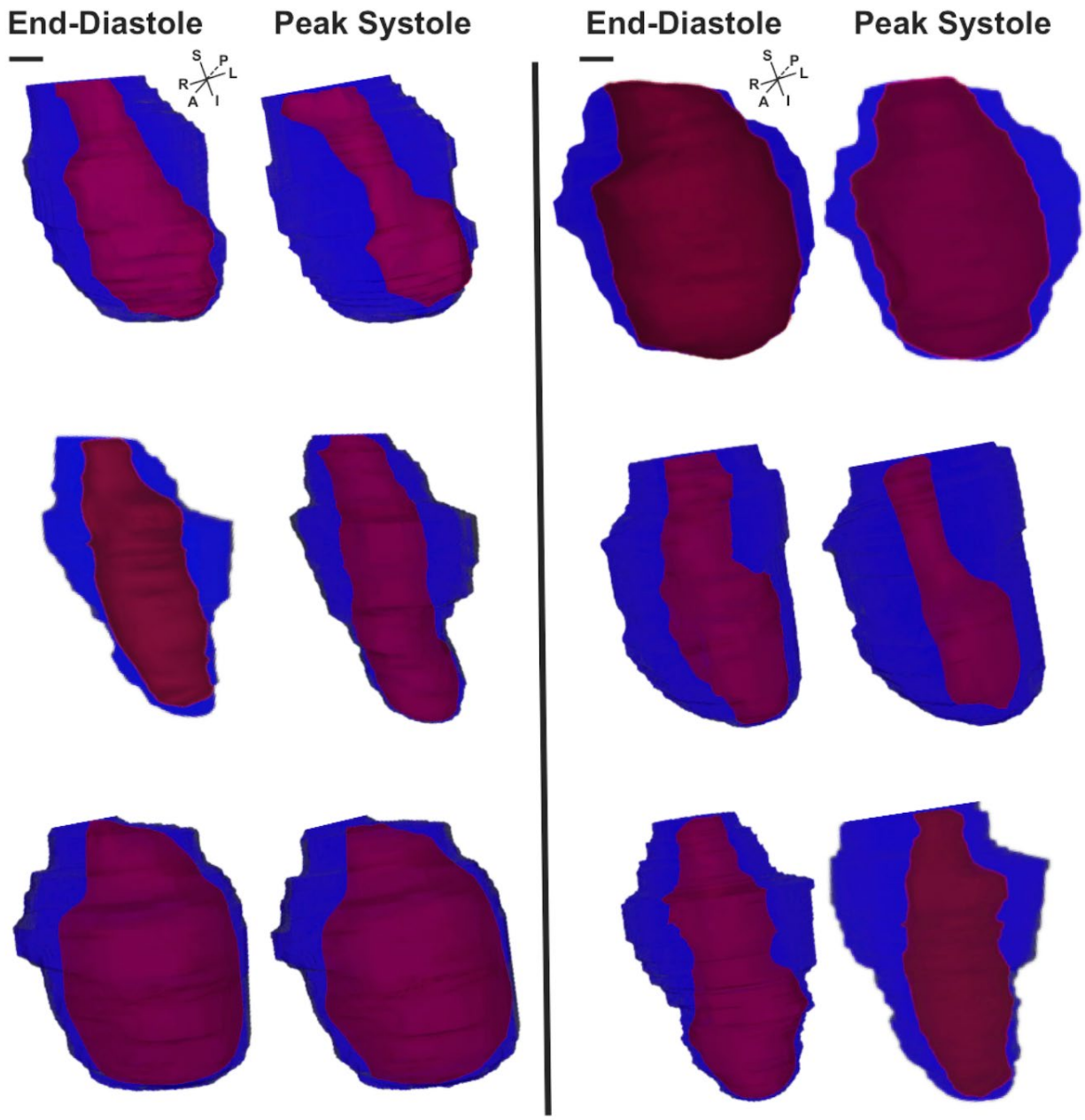

Fig. A.5: 3D renderings of the left ventricular lumen (red) and myocardial wall (blue) of remodeled mice hearts with varying degrees of myocardial infarction acquired four-weeks post coronary artery ligation (*n*=6). Comparisons of left ventricular geometries at end-diastole and peak-systole showed regions of necrotic myocardium with akinesia and wall thinning. S = superior; I = inferior, P = posterior, A = anterior, R = right; L = left. Scalebar = 1mm.

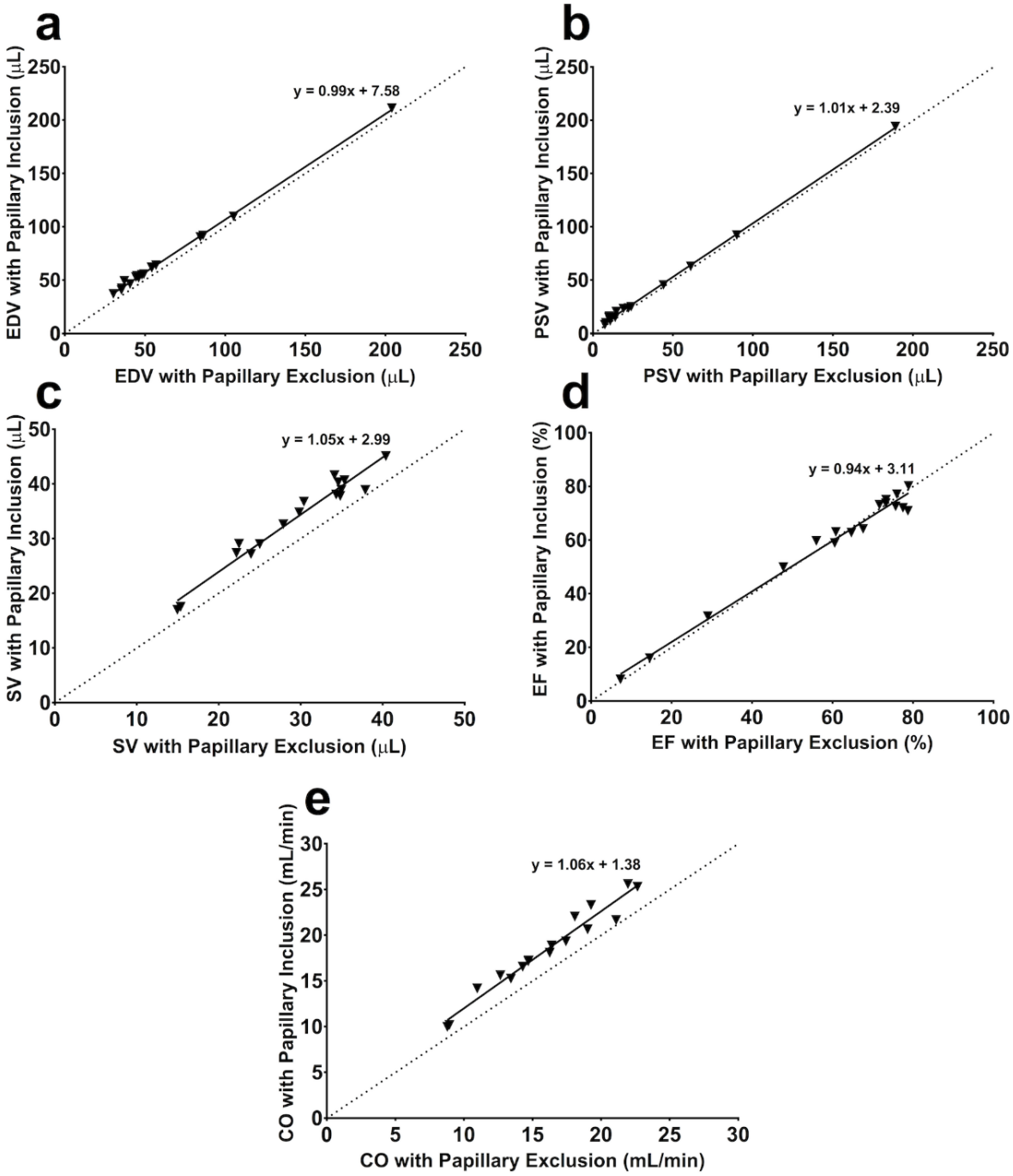

Fig. A.6: Linear regression plots comparing the contributions of papillary muscles on the direct evaluation of different cardiac parameters using the 4D technique. Here, the term papillary exclusion means that the volume contribution of the papillary muscles is not included in the determination of left ventricular volumes. EDV = end-diastolic volume; PSV = peak-systolic volume; SV = stroke volume; EF = ejection fraction; CO = cardiac output.

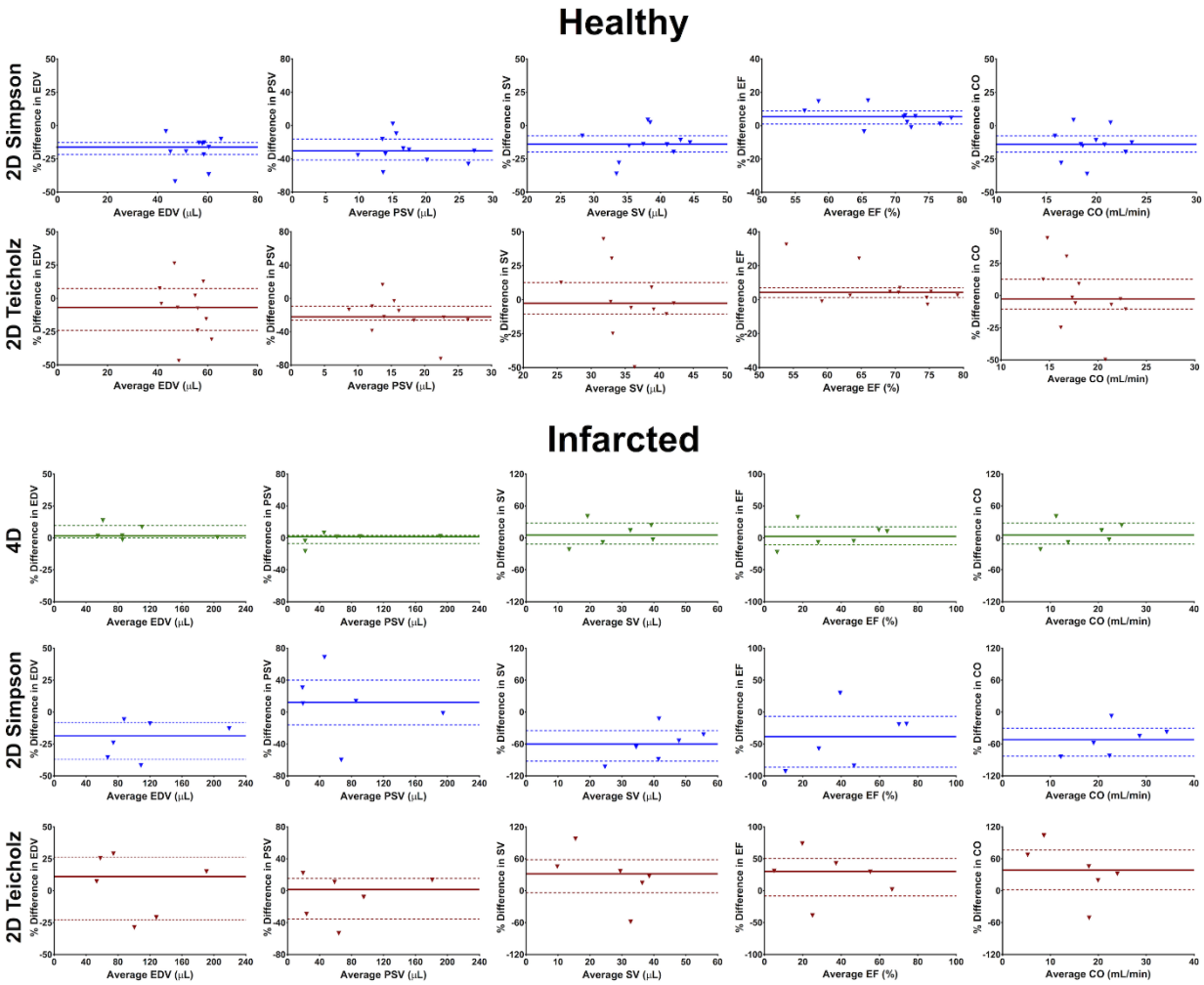

Fig. A.7: Percent difference Bland-Altman plots of cardiac parameters in healthy and infarcted left ventricles. To calculate percent difference for the healthy case, the difference between cardiac parameter values from the 4D technique and the corresponding labeled technique was divided by their averaged values. For the infarcted case, cardiac parameter values obtained from MRI was subtracted by those obtained from the corresponding labeled technique before their difference was divided by their averaged values. Note that compared to values obtained from gold-standard MRI, results acquired directly from the 4D technique aligned much more closely than those approximated from the 2D techniques when evaluating infarcted left ventricles. EDV = end-diastolic volume; PSV = peak-systolic volume; SV = stroke volume; EF = ejection fraction; CO = cardiac output. Solid lines = median; dashed lines = first and third quartile lines.

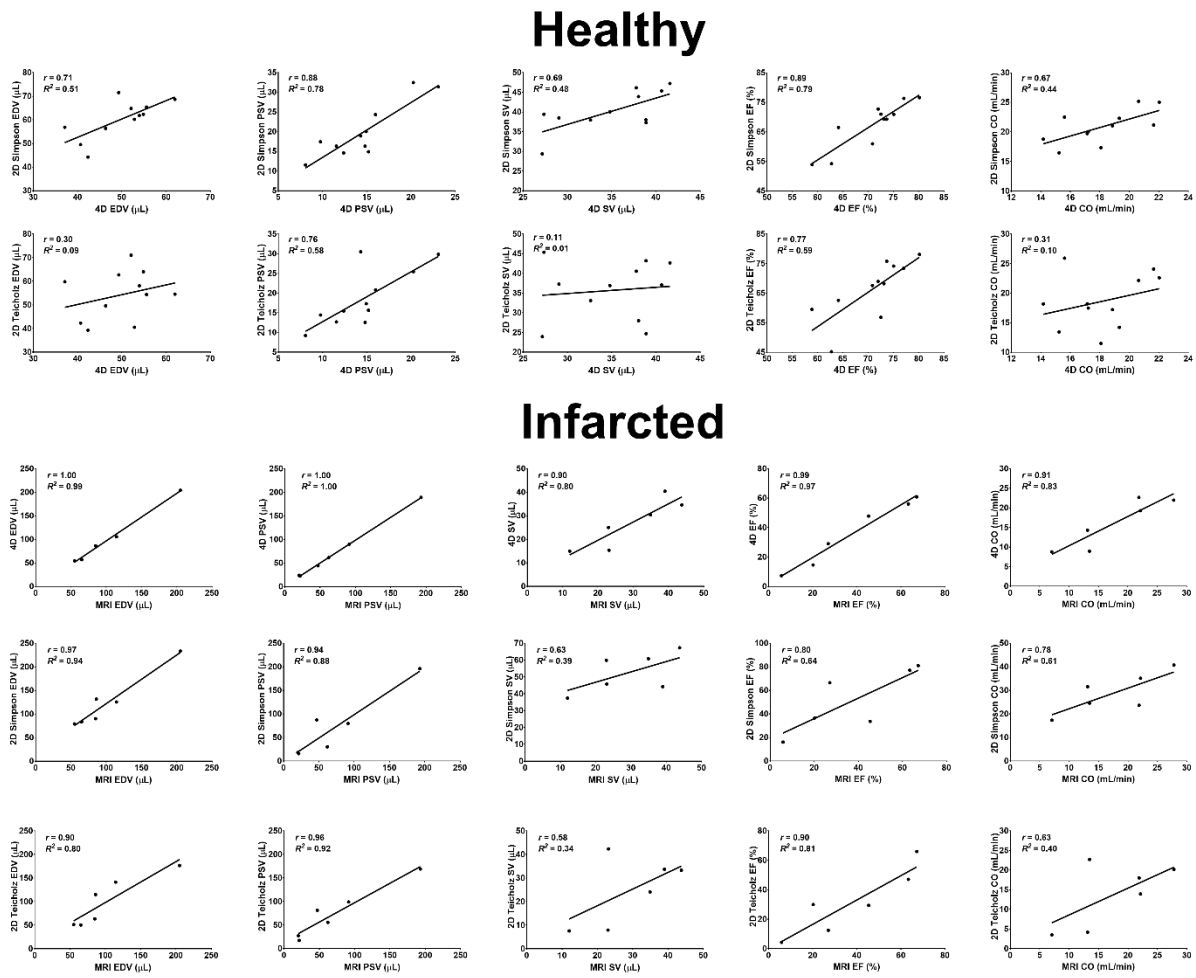

Fig. A.8: Correlation plots of cardiac parameters in healthy and infarcted left ventricles between the different analysis techniques. EDV = end-diastolic volume; PSV = peak-systolic volume; SV = stroke volume; EF = ejection fraction; CO = cardiac output.

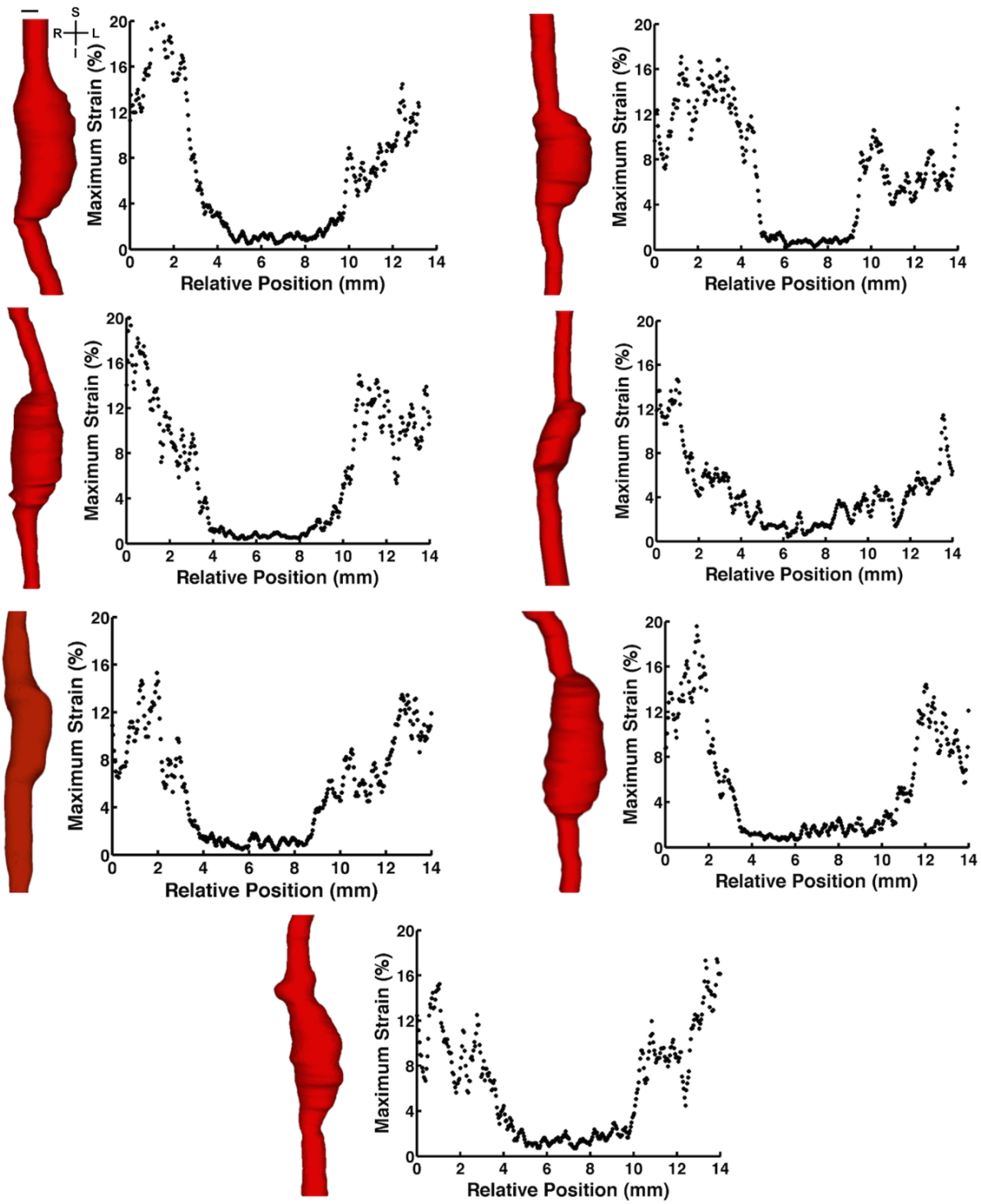

Fig. A.9: 4D ultrasound analysis of mouse AAA data (*n*=7). 3D volume renderings of mouse AAAs during systole are shown in red with the aneurysm positioned at the center. Green-Lagrange maximum circumferential strain, plotted relative to the abdominal aorta positions, are shown to the right of each AAAs, highlighting elastic walls located proximal and distal to the stiff aneurysm. S = superior; I = inferior, R = right; L = left. Scalebar = 1mm.

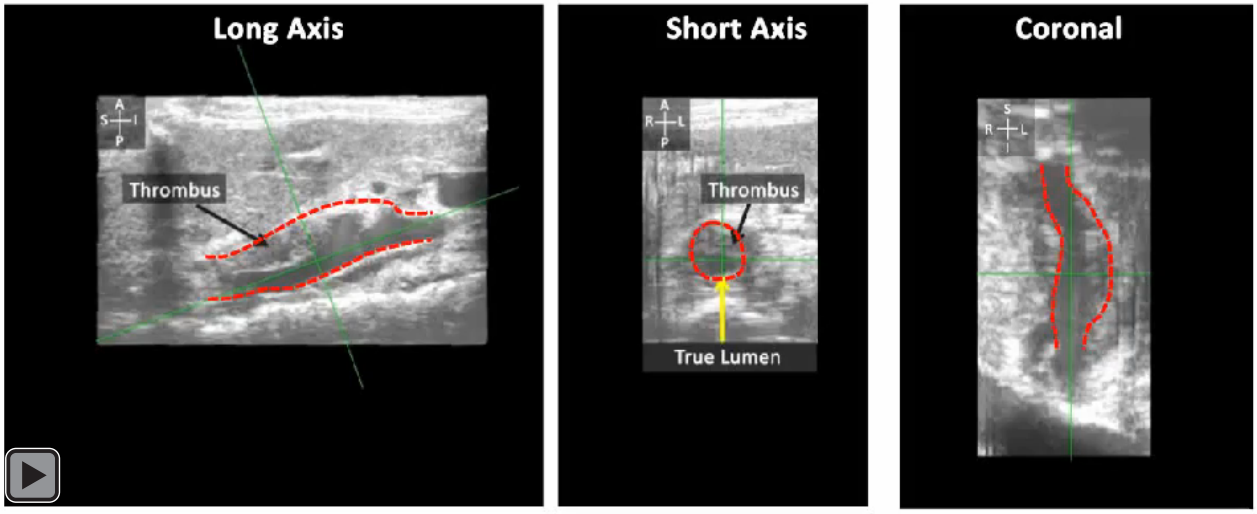

Fig. A.10: A three-axis view cine loop of a mouse abdominal aorta with a dissecting aneurysm. Ultrasound images of the aneurysm, outlined in red, were obtained two-weeks post-aneurysm formation. Note that regions proximal and distal to the aneurysm exhibit higher pulsatility that regions within the stiff aneurysm. Black arrows point to the formation of intraluminal thrombus, while yellow arrow points to the true lumen position. Green crosshairs highlight the center of the visualized structure. S = superior; I = inferior, R = right, L = left. Scalebar = 1mm.

APPENDIX B. SUPPLEMENTAL DATA TO CHAPTER 5

Appendix B.1: Validation and Benchmarking of 3D-DDE

Comparison to state of the art methods showed that 3D-DDE was more accurate and precise than displacement-based methods

To test 3D-DDE *in silico*, we first resolved non-uniform strain fields arising in an artificial image volume from a spatially- and temporally-varying deformation gradient tensor, **F**, in an orthogonal Cartesian (X,Y,Z) frame defined relative to the reference image volume:

$$\mathbf{F}(X, t)=\mathbf{I} + AtX^2\ \mathbf{e} \otimes \mathbf{e} \qquad \textbf{(B.1)}$$

where A controlled amplitude, time t ranged from 0 to 1, **I** is the second-order identity tensor, and **e** is a unit vector in the X-direction. This spatially quadratic field was chosen as a best-case scenario for competing XCOR methods because, under these conditions, XCOR's imposition of displacement compatibility on strain fields can converge to the exact strain fields [106]. When a random 3D texture was deformed according to **Eq. B.1**, 3D-DDE was more accurate and more precise than both standard 3D-XCOR and displacement-based tracking (3D-LSF) for all parameter choices **(Fig. B.1)**. Although displacement-based approaches were just as accurate as 3D-DDE for *uniform* strain fields, 3D-DDE was superior for all cases involving strain gradients **(Fig. B.1)**.

3D-DDE accurately estimated strains in representative 3D strain fields

Next, to benchmark 3D-DDE against other methods on representative data for which the true strain fields were known, displacement fields of an Eshelby inclusion were used to nonlinearly warp a volumetric image *in silico*. Using closed form solutions for a full field 3D Eshelby inclusion, true values of deformation were known *a priori* at every location in time and space for this problem **(Fig. B.2 A)** [196]. 3D-DDE was accurate and precise, with 3D-LSF and 3D-XCOR each performing successively worse **(Figs. B.2 C,D,E,F)**. The challenge of distinguishing tracking errors from true regions of elevated strain was overcome through 3D-SIMPLE, which identified the regions of high strain gradient and elevated strain surrounding the inclusion **(Fig. B.2 B)**.

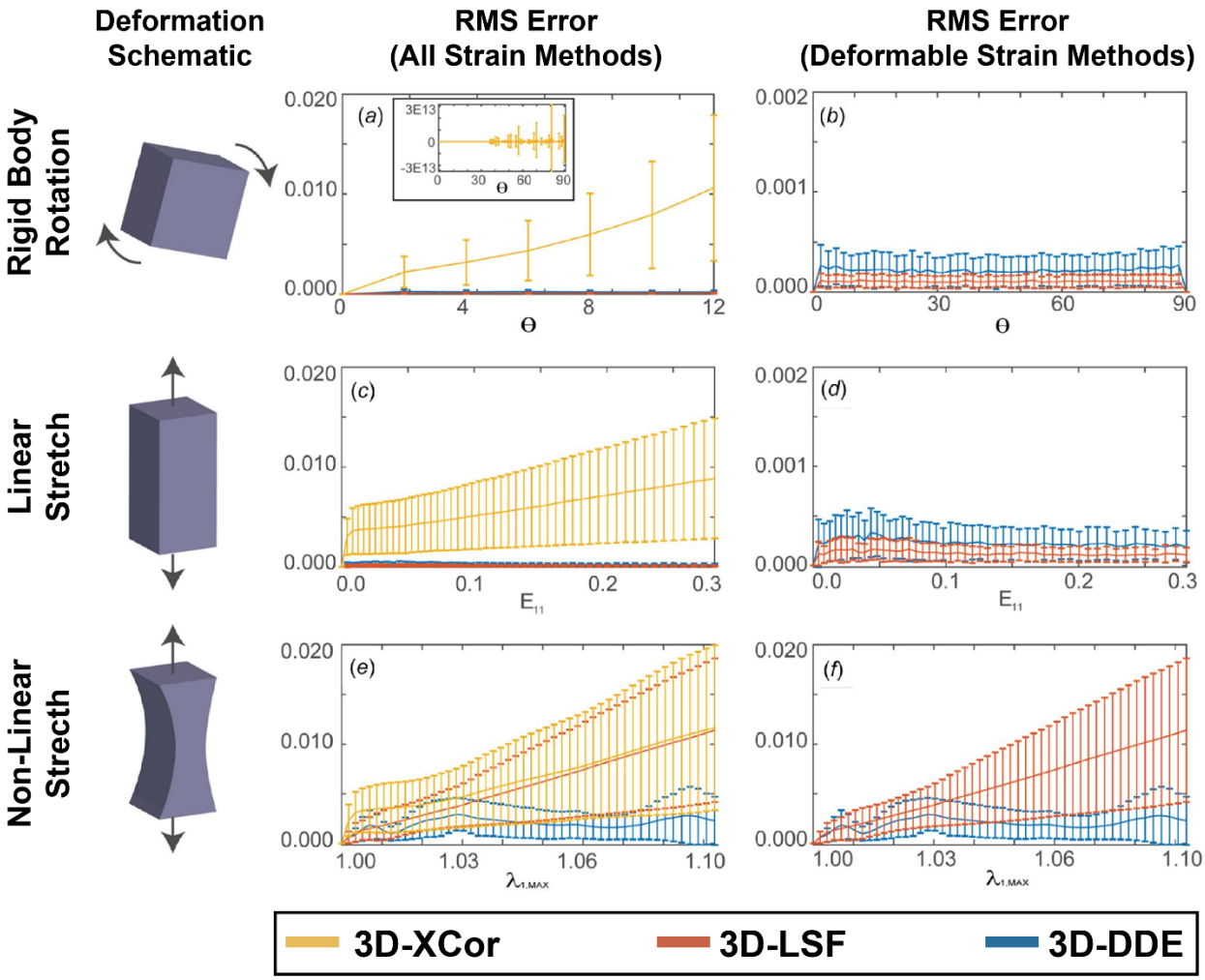

Fig. B.1: Accuracy and precision of 3D-DDE relative to other strain mapping techniques. 3D-DDE was over an order of magnitude more accurate and substantially more precise than other methods for estimating spatially varying strain fields in artificial images. **(A)** For a 3D rigid body rotated an angle Θ in one plane, 3D-XCOR failed to correctly predict the strain field, with error that was nearly unbounded for large rotation angles **(inset)**. **(B)** 3D-LSF and 3D-DDE had negligible errors for rigid body rotations. **(C)** RMS error for a uniaxial stretch E_{11} scaled with strain for 3D-XCOR. **(D)** 3D-LSF and 3D-DDE had negligible error for linear, uniform straining. **(E)** RMS error increased with stretch level λ for both 3D-XCOR and 3D-LSF in a 3D body undergoing non-linear stretch. **(F)** However, 3D-DDE again estimated strains with minimal error for these nonlinear, nonuniform strain fields. Note that panels **B**, **D**, and **F** contain data from panels **A**, **C**, and **E**, respectively, zoomed in to focus on results comparing only 3D-LSF and 3D-XCOR.

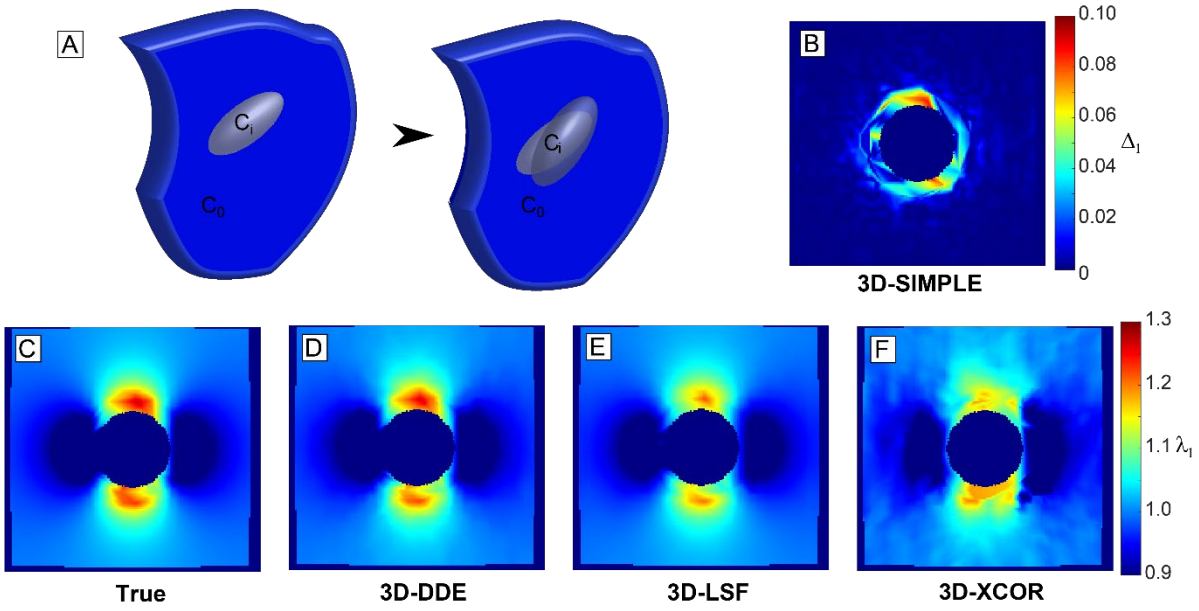

Fig. B.2: Principal stretch ratio estimations around image volumes of a contracting Eshelby inclusion, generated *in silico*. **(A)** Schematic of the Eshelby problem. **(B)** 3D-SIMPLE detected strain elevation surrounding the inclusion. **(C)** True values of the stretch ratio in the *z*-direction matched **(D)** the 3D-DDE estimated values, while **(E)** 3D-LSF- and **(F)** 3D-XCOR-estimates were successively worse.

3D-DDE and 3D-SIMPLE identified and characterized singular strain fields

To benchmark 3D-DDE against other methods on a more complicated strain field for which the exact solutions were known, displacement fields surrounding a penny-shaped crack were used to nonlinearly warp a volumetric image *in silico* following the procedures used for the Eshelby solution **(Fig. B.3 A)** [197]. During loading, the crack, initially ellipsoidal due to a pre-load, extended into a more spherical ellipsoid. Again, 3D-DDE identified the input strain field faithfully, with 3D-LSF and 3D-XCOR performing successively worse **(Fig. B.3 C-F)**. 3D-SIMPLE identified regions of elevated strain and high strain gradient, including both the singular crack tips and the displacing fracture surfaces **(Fig. B.3 B)**.

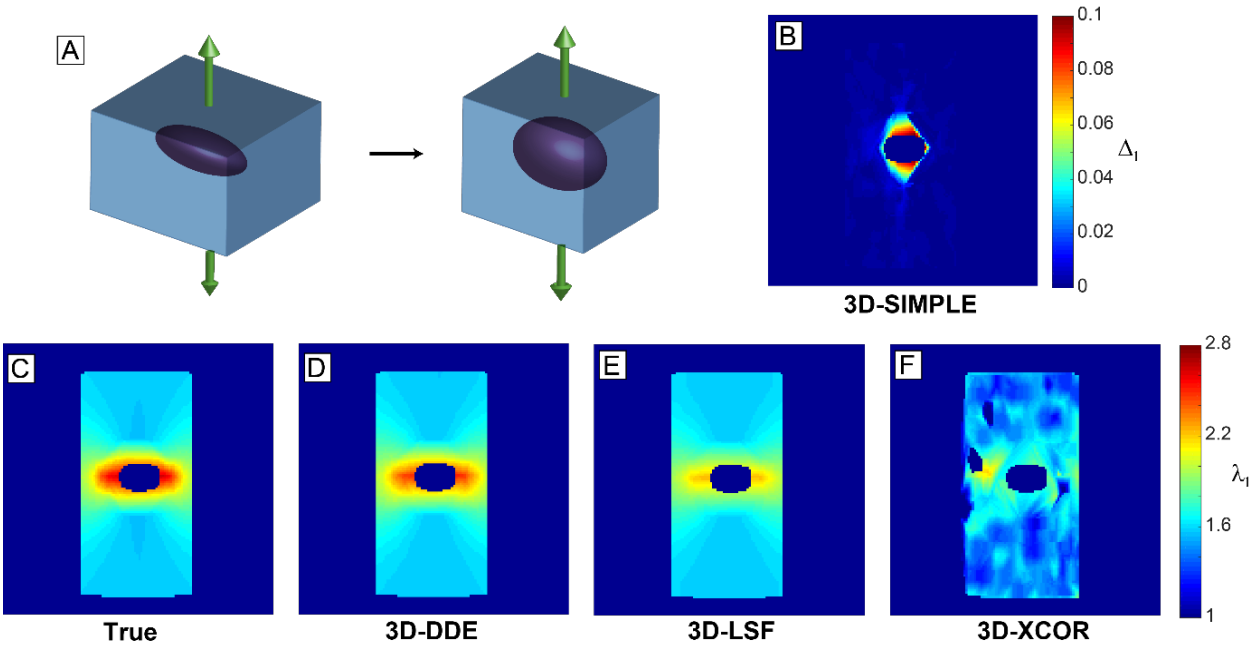

Fig. B.3: Principal stretch ratios for image volumes of a pre-loaded, penny-shaped crack generated *in silico.* **(A)** Schematic. **(B)** 3D-SIMPLE detected the developing crack, **(C-D)** 3D-DDE estimates matched the actual fields, while 3D-LSF **(E)** and 3D-XCOR **(F)** were successively less accurate.

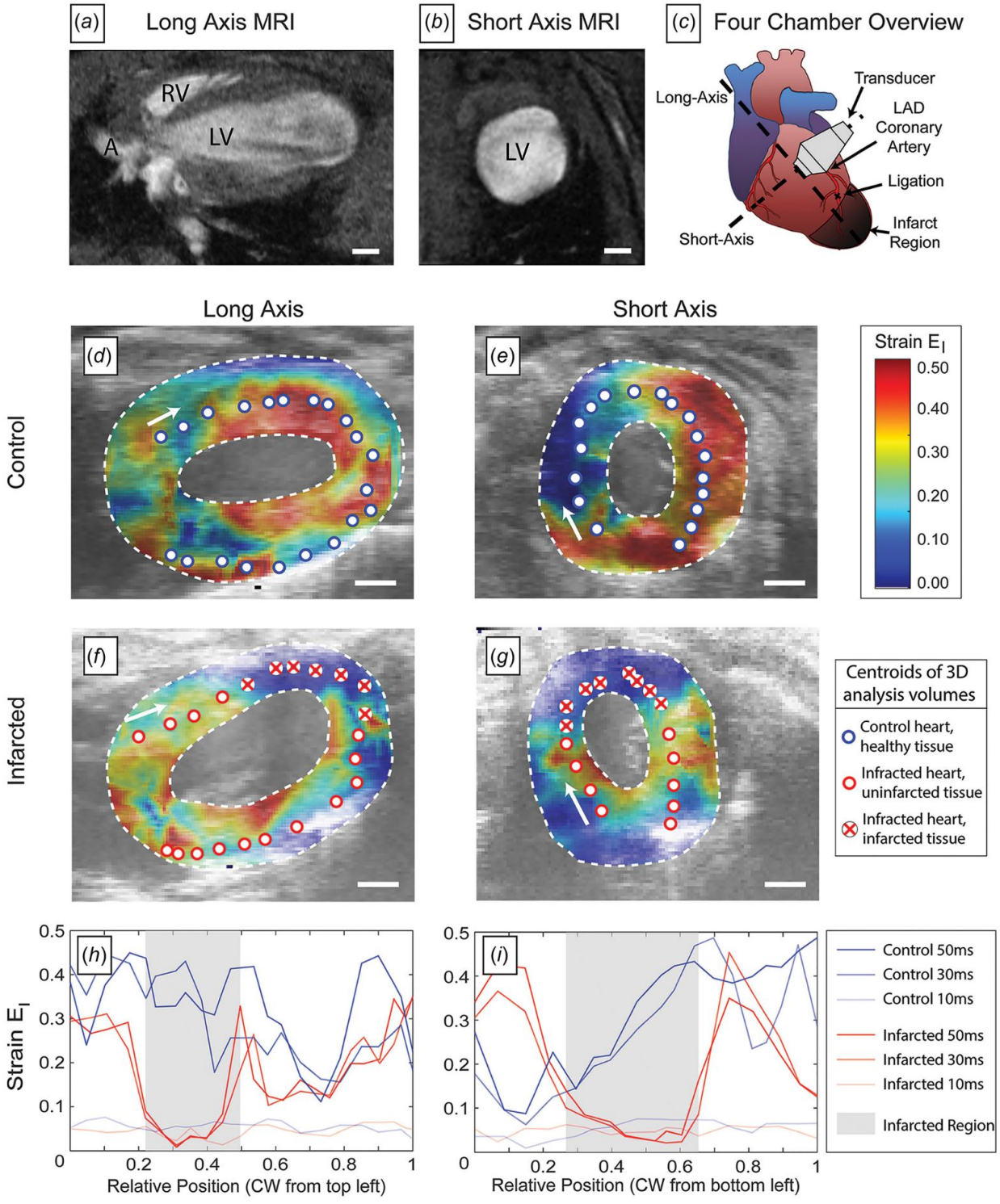

Fig. B.4: Strain patterns in control versus post-myocardial infarction hearts, demonstrating dramatically reduced strains in infarcted heart tissue. **(A,B)** Magnetic resonance images of mouse hearts showing the anatomical planes studied using 3D-DDE of ultrasound imaging volumes. **(C)** A schematic of the heart demonstrating the orientation of the short and long axis as well as the location of the infarction. **(D,E)** Peak principal strain at a specific

timepoint in control hearts. **(F,G)** Peak principal strain at this same timepoint in hearts following myocardial infarction, showing distinctly different strain patterns in both the long and short axis views. **(H)** Strain as a function of position along the midline of the long-axis view of the heart, showing strain attenuation in the infarcted tissue. Line corresponds to different times; position is measured from the base of the arrow in panel **F**. **(I)** Strain as a function of position along the midline of the short-axis view of the heart, showing strain attenuation in the infarcted tissue, and elevated strain in the tissue surrounding the infarct region. Lines again correspond to different times; position is measured from the base of the arrow in panel **G**. Scalebar: 1mm.

APPENDIX C. SUPPLEMENTAL DATA TO CHAPTER 6

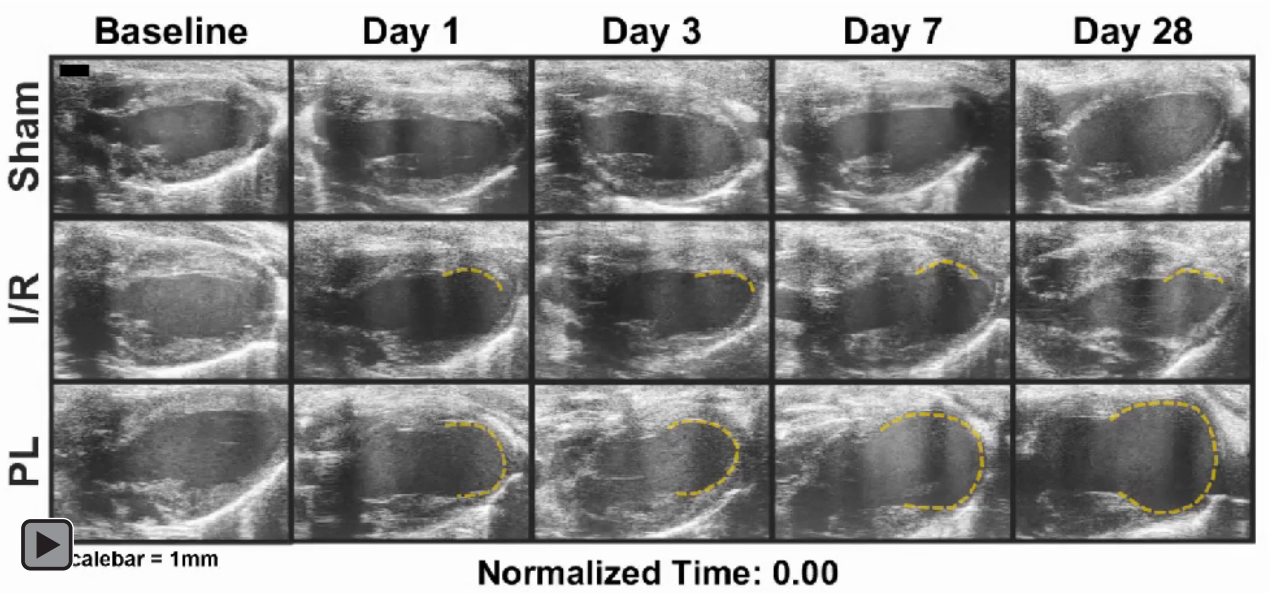

Fig. C.1: Representative long-axis videos of the remodeling mouse LVs. Cine loop data are resampled to temporally match timestamps throughout the entire cardiac cycle. Akinetic regions of the myocardial wall are outlined in dashed yellow lines. Scalebar: 1mm.

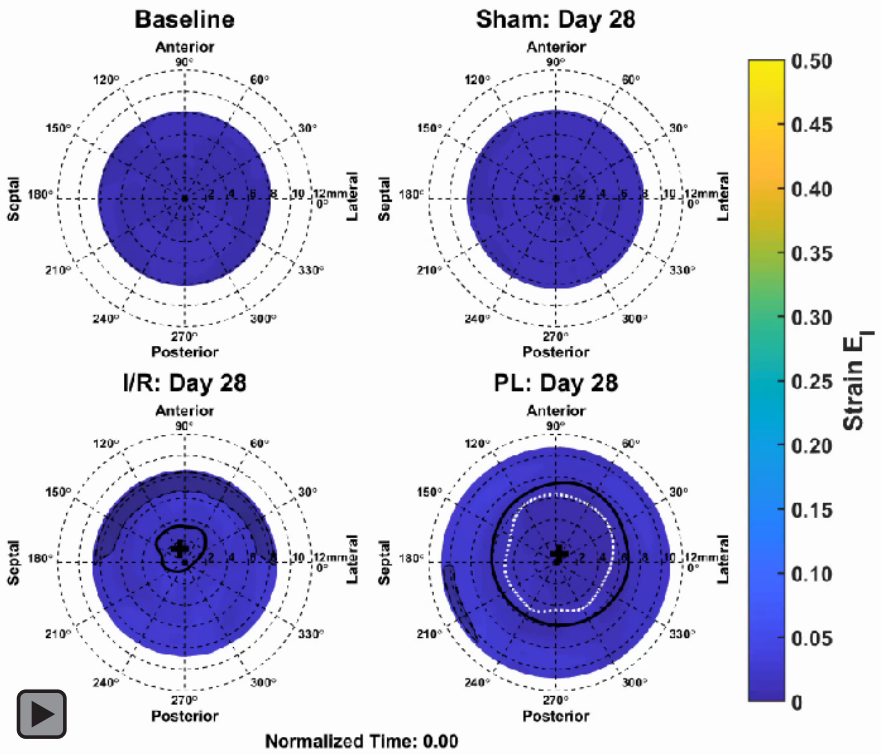

Fig. C.2: Video representations of LV bullseye strain maps throughout the cardiac cycle, taken at baseline and day 28, for a representative mouse in each surgical group.

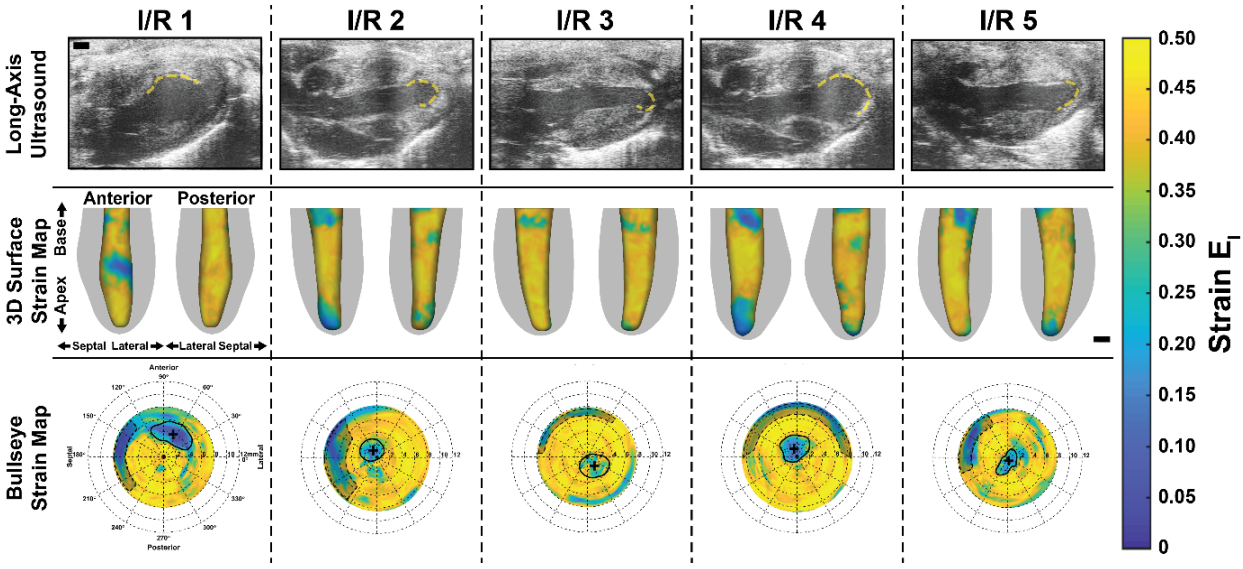

Fig. C.3: Representative day 28 long-axis ultrasound images **(top)**, 3D surface strains **(middle)**, and bullseye strain maps **(bottom)** of the remodeled LVs for all five mice in the I/R group. The akinetic myocardium is marked in dashed yellow lines, and the strain estimated infarct size is outlined in solid black line. Sternal artifact is shaded in gray with black dashed border. Scalebar: 1mm.

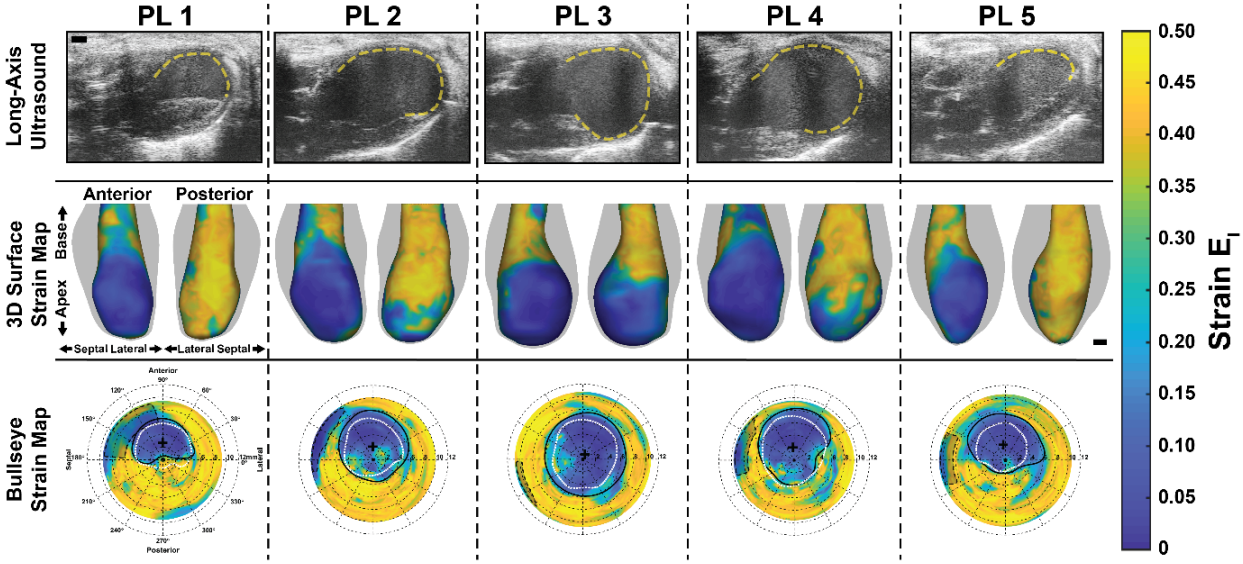

Fig. C.4: Representative day 28 long-axis ultrasound images **(top)**, 3D surface strains **(middle)**, and bullseye strain maps **(bottom)** of the remodeled LVs for all five mice in the PL group. The akinetic myocardium is marked in dashed yellow lines, the strain estimated infarct boundary is outlined in solid black line, and the wall-thinned infarct boundary is marked in dotted white line. Sternal artifact is shaded in gray with black dashed border. Scalebar: 1mm.

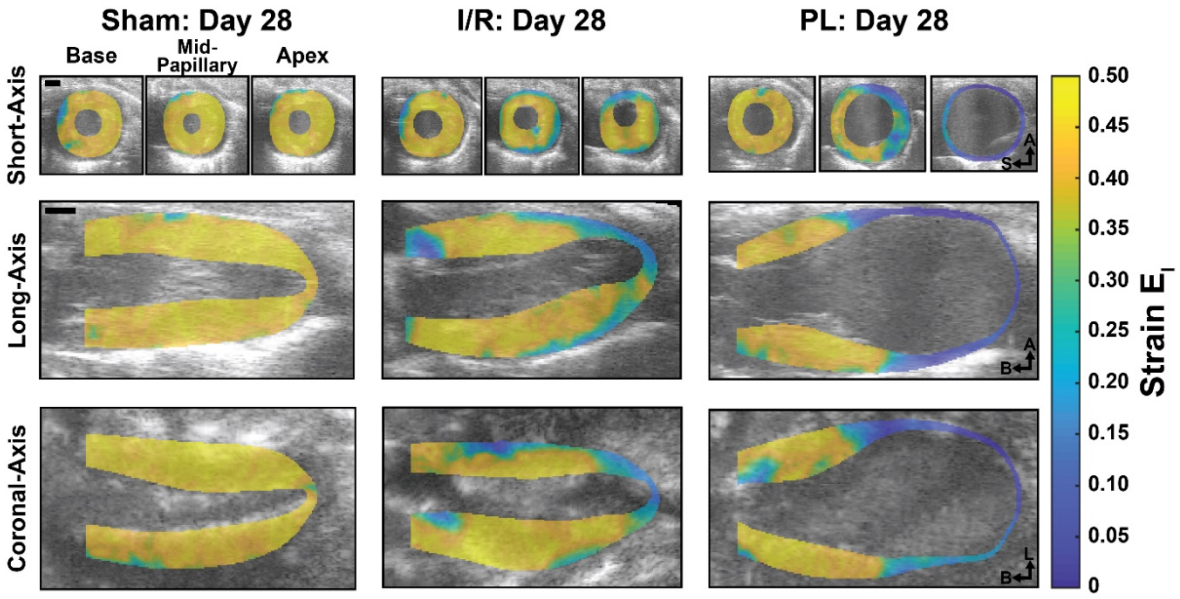

Fig. C.5: Representative day-28 maximum principal 3D strains are presented along the entire thickness of the LV wall for each surgical group. Yellow and blue regions correspond to areas of high and low strains respectively. A: anterior, S: septal, L: lateral; B: base. Scalebar: 1mm.

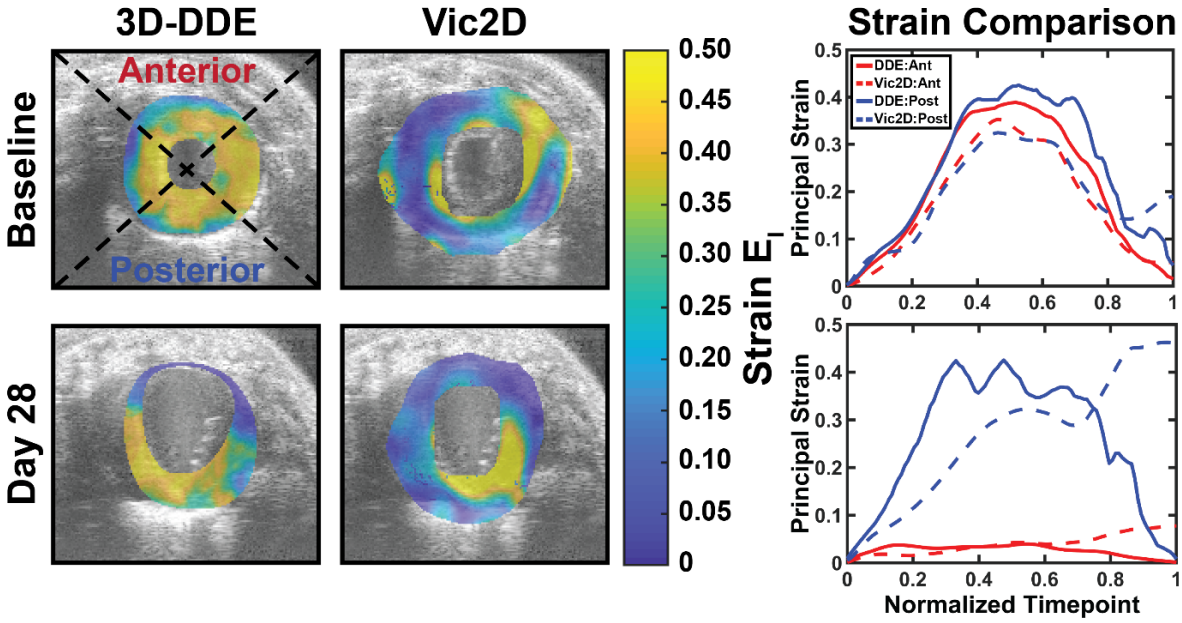

Fig. C.6: Comparison of maximum principal strains estimated with 3D Direct Deformation Estimation (DDE, solid lines) and Vic2D (dashed lines). Short-axis ultrasound strain data along the anterior (red) and posterior (blue) myocardial walls are shown at baseline and at day 28 post-permanent ligation. Although both 3D-DDE and Vic2D demonstrated significantly lower strain values along the infarcted, anterior myocardium post-surgery, the 3D-DDE method more appropriately tracked changes in myocardial strain, as strain values returned to 0 at the end of the cardiac cycle.

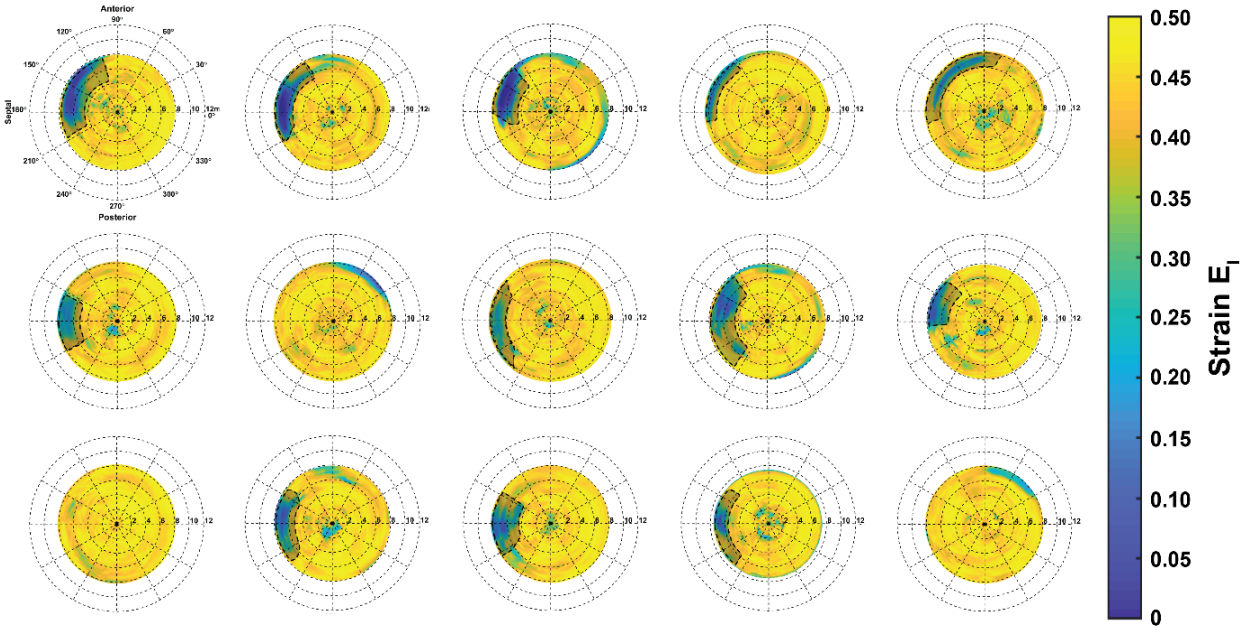

Fig. C.7: Bullseye maps of the maximum principal 3D Green-Lagrange strain (E_1) for all 15 mice at baseline. Consistent high strain values throughout the LV myocardium across all animals highlight the reproducibility of the 3D strain technique.

Table C.1: Summary of LV end-diastolic volumes for mice subjected to the different surgical procedures over 28-days.

End Diastolic Volume (µL)									
	Baseline	**Day 1**	**Day 2**	**Day 3**	**Day 5**	**Day 7**	**Day 14**	**Day 21**	**Day 28**
Sham	53 ± 3	53 ± 1	52 ± 2	53 ± 2	53 ± 2	52 ± 1	53 ± 1	53 ± 2	53 ± 1
I/R	52 ± 2	52 ± 2	53 ± 1	54 ± 2	54 ± 3	57 ± 4	61 ± 7	64 ± 8	68 ± 8
PL	52 ± 2	65 ± 3	70 ± 8	76 ± 12	95 ± 20	108 ± 24	130 ± 37	142 ± 31	151 ± 38

Data presented as mean ± standard deviations. I/R: ischemia-reperfusion, PL: permanent ligation.

Table C.2: Summary of LV peak-systolic volumes for mice subjected to the different surgical procedures over 28-days.

Peak Systolic Volume (μL)									
	Baseline	**Day 1**	**Day 2**	**Day 3**	**Day 5**	**Day 7**	**Day 14**	**Day 21**	**Day 28**
Sham	16 ± 1	18 ± 1	17 ± 1	16 ± 1	17 ± 1	17 ± 2	17 ± 1	17 ± 1	18 ± 1
I/R	17 ± 2	28 ± 2	26 ± 2	26 ± 1	26 ± 3	27 ± 3	27 ± 5	30 ± 7	34 ± 8
PL	17 ± 2	47 ± 6	48 ± 12	53 ± 14	72 ± 24	81 ± 30	101 ± 40	109 ± 36	119 ± 46

Data presented as mean ± standard deviations. I/R: ischemia-reperfusion, PL: permanent ligation.

Table C.3: Summary of LV stroke volumes for mice subjected to the different surgical procedures over 28-days.

Stroke Volume (μL)									
	Baseline	**Day 1**	**Day 2**	**Day 3**	**Day 5**	**Day 7**	**Day 14**	**Day 21**	**Day 28**
Sham	36 ± 3	35 ± 1	35 ± 1	36 ± 2	36 ± 2	35 ± 2	35 ± 1	36 ± 2	35 ± 2
I/R	35 ± 3	24 ± 2	26 ± 3	28 ± 2	28 ± 3	30 ± 2	33 ± 3	34 ± 3	34 ± 4
PL	35 ± 2	19 ± 6	22 ± 6	22 ± 4	24 ± 5	27 ± 6	29 ± 9	33 ± 11	32 ± 13

Data presented as mean ± standard deviations. I/R: ischemia-reperfusion, PL: permanent ligation.

Table C.4: Summary of LV ejection fraction for mice subjected to the different surgical procedures over 28-days.

Ejection Fraction (%)									
	Baseline	**Day 1**	**Day 2**	**Day 3**	**Day 5**	**Day 7**	**Day 14**	**Day 21**	**Day 28**
Sham	69 ± 3	67 ± 2	67 ± 1	69 ± 3	68 ± 2	67 ± 4	67 ± 3	68 ± 2	66 ± 3
I/R	67 ± 4	46 ± 3	50 ± 5	52 ± 3	51 ± 4	53 ± 3	55 ± 2	54 ± 6	50 ± 7
PL	67 ± 3	29 ± 9	33 ± 11	31 ± 9	26 ± 10	27 ± 12	24 ± 10	25 ± 11	23 ± 12

Data presented as mean ± standard deviations. I/R: ischemia-reperfusion, PL: permanent ligation.

Table C.5: Summary of LV cardiac output for mice subjected to the different surgical procedures over 28-days.

Cardiac Output (mL/min)									
	Baseline	**Day 1**	**Day 2**	**Day 3**	**Day 5**	**Day 7**	**Day 14**	**Day 21**	**Day 28**
Sham	20 ± 1	20 ± 3	21 ± 2	22 ± 1	21 ± 2	22 ± 2	21 ± 1	23 ± 2	21 ± 3
I/R	20 ± 4	13 ± 2	16 ± 3	16 ± 1	17 ± 2	17 ± 3	20 ± 3	21 ± 2	19 ± 3
PL	19 ± 1	12 ± 3	13 ± 4	13 ± 2	15 ± 3	18 ± 3	17 ± 5	20 ± 6	17 ± 7

Data presented as mean ± standard deviations. I/R: ischemia-reperfusion, PL: permanent ligation.

Table C.6: Summary of LV infarct size, as calculated by the strain-estimated or wall-thinned criteria, for mice subjected to the different surgical procedures over 28-days.

Infarct Size (% of LV)										
		Baseline	**Day 1**	**Day 2**	**Day 3**	**Day 5**	**Day 7**	**Day 14**	**Day 21**	**Day 28**
Strain Estimated	**I/R**	N/A	4 ± 3	3 ± 2	3 ± 2	7 ± 2	8 ± 3	9 ± 4	10 ± 3	11 ± 4
	PL	N/A	43 ± 13	46 ± 8	42 ± 13	48 ± 20	49 ± 19	46 ± 17	49 ± 14	46 ± 16
Wall-Thinned	**PL**	N/A	14 ± 6	17 ± 7	19 ± 5	22 ± 8	35 ± 10	34 ± 11	40 ± 12	41 ± 11

Data presented as mean ± standard deviations. I/R: ischemia-reperfusion, PL: permanent ligation.

Table C.7: Summary of LV collagen content, as measured from Masson's Trichrome histological staining, for the different regions of the LV.

Collagen Content (%)			
	Base	**Mid Papillary**	**Apex**
Sham	2 ± 1	2 ± 1	3 ± 2
I/R	7 ± 2	11 ± 3	15 ± 8
PL	7 ± 3	23 ± 6	38 ± 19

Data presented as mean ± standard deviations. I/R: ischemia-reperfusion, PL: permanent ligation.

REFERENCES

[1] Mortality, G.B.D. & Causes of Death, C. 2015 Global, regional, and national age-sex specific all-cause and cause-specific mortality for 240 causes of death, 1990-2013: a systematic analysis for the Global Burden of Disease Study 2013. *Lancet* **385**, 117-171. (doi:10.1016/S0140-6736(14)61682-2).

[2] Mozaffarian, D., Benjamin, E.J., Go, A.S., Arnett, D.K., Blaha, M.J., Cushman, M., Das, S.R., de Ferranti, S., Despres, J.P., Fullerton, H.J., et al. 2016 Heart Disease and Stroke Statistics-2016 Update: A Report From the American Heart Association. *Circulation* **133**, e38-60. (doi:10.1161/CIR.0000000000000350).

[3] Benjamin, E.J., Muntner, P., Alonso, A., Bittencourt, M.S., Callaway, C.W., Carson, A.P., Chamberlain, A.M., Chang, A.R., Cheng, S., Das, S.R., et al. 2019 Heart Disease and Stroke Statistics-2019 Update: A Report From the American Heart Association. *Circulation* **139**, e56-e528. (doi:10.1161/CIR.0000000000000659).

[4] Cohn, J.N., Ferrari, R. & Sharpe, N. 2000 Cardiac remodeling--concepts and clinical implications: a consensus paper from an international forum on cardiac remodeling. Behalf of an International Forum on Cardiac Remodeling. *J Am Coll Cardiol* **35**, 569-582. (doi:10.1016/s0735-1097(99)00630-0).

[5] Gerdes, A.M., Kellerman, S.E., Moore, J.A., Muffly, K.E., Clark, L.C., Reaves, P.Y., Malec, K.B., McKeown, P.P. & Schocken, D.D. 1992 Structural remodeling of cardiac myocytes in patients with ischemic cardiomyopathy. *Circulation* **86**, 426-430.

[6] French, B.A. & Kramer, C.M. 2007 Mechanisms of Post-Infarct Left Ventricular Remodeling. *Drug Discov Today Dis Mech* **4**, 185-196. (doi:10.1016/j.ddmec.2007.12.006).

[7] Mill, J.G., Stefanon, I., dos Santos, L. & Baldo, M.P. 2011 Remodeling in the ischemic heart: the stepwise progression for heart failure. *Braz J Med Biol Res* **44**, 890-898.

[8] Todica, A., Beetz, N.L., Gunther, L., Zacherl, M.J., Grabmaier, U., Huber, B., Bartenstein, P., Brunner, S. & Lehner, S. 2017 Monitoring of Cardiac Remodeling in a Mouse Model of Pressure-Overload Left Ventricular Hypertrophy with [(18)F]FDG MicroPET. *Mol Imaging Biol*. (doi:10.1007/s11307-017-1114-6).

[9] Matsubara, L.S., Narikawa, S., Ferreira, A.L., Paiva, S.A., Zornoff, L.M. & Matsubara, B.B. 2006 [Myocardial remodeling in chronic pressure or volume overload in the rat heart]. *Arq Bras Cardiol* **86**, 126-130. (doi:/S0066-782X2006000200008).

[10] Krumholz, H.M., Wang, Y., Chen, J., Drye, E.E., Spertus, J.A., Ross, J.S., Curtis, J.P., Nallamothu, B.K., Lichtman, J.H., Havranek, E.P., et al. 2009 Reduction in acute myocardial infarction mortality in the United States: risk-standardized mortality rates from 1995-2006. *JAMA* **302**, 767-773. (doi:10.1001/jama.2009.1178).

[11] Bui, A.L., Horwich, T.B. & Fonarow, G.C. 2011 Epidemiology and risk profile of heart failure. *Nat Rev Cardiol* **8**, 30-41. (doi:10.1038/nrcardio.2010.165).

[12] Nepper-Christensen, L., Lonborg, J., Ahtarovski, K.A., Hofsten, D.E., Kyhl, K., Ghotbi, A.A., Schoos, M.M., Goransson, C., Bertelsen, L., Kober, L., et al. 2017 Left Ventricular Hypertrophy Is Associated With Increased Infarct Size and Decreased Myocardial Salvage in Patients With ST-Segment Elevation Myocardial Infarction Undergoing Primary Percutaneous Coronary Intervention. *J Am Heart Assoc* **6**. (doi:10.1161/JAHA.116.004823).

[13] Marino, P., Golia, G. & Zardini, P. 1991 *Left ventricular shape changes and modelling during acute myocardial infarction.* Dordrecht, Springer.

[14] Richardson, W.J., Clarke, S.A., Quinn, T.A. & Holmes, J.W. 2015 Physiological Implications of Myocardial Scar Structure. *Compr Physiol* **5**, 1877-1909. (doi:10.1002/cphy.c140067).

[15] Hutchins, G.M. & Bulkley, B.H. 1978 Infarct expansion versus extension: two different complications of acute myocardial infarction. *Am J Cardiol* **41**, 1127-1132.

[16] Miller, T.D., Christian, T.F., Hopfenspirger, M.R., Hodge, D.O., Gersh, B.J. & Gibbons, R.J. 1995 Infarct size after acute myocardial infarction measured by quantitative tomographic 99mTc sestamibi imaging predicts subsequent mortality. *Circulation* **92**, 334-341.

[17] Sobel, B.E., Bresnahan, G.F., Shell, W.E. & Yoder, R.D. 1972 Estimation of infarct size in man and its relation to prognosis. *Circulation* **46**, 640-648.

[18] Whittaker, P., Boughner, D.R. & Kloner, R.A. 1991 Role of collagen in acute myocardial infarct expansion. *Circulation* **84**, 2123-2134.

[19] Ertl, G. & Frantz, S. 2005 Healing after myocardial infarction. *Cardiovasc Res* **66**, 22-32. (doi:10.1016/j.cardiores.2005.01.011).

[20] Mizuno, T., Yau, T.M., Weisel, R.D., Kiani, C.G. & Li, R.K. 2005 Elastin stabilizes an infarct and preserves ventricular function. *Circulation* **112**, I81-88. (doi:10.1161/01.CIRCULATIONAHA.105.523795).

[21] Sutton, M.G. & Sharpe, N. 2000 Left ventricular remodeling after myocardial infarction: pathophysiology and therapy. *Circulation* **101**, 2981-2988. (doi:10.1161/01.CIR.101.25.2981).

[22] Weisman, H.F., Bush, D.E., Mannisi, J.A., Weisfeldt, M.L. & Healy, B. 1988 Cellular mechanisms of myocardial infarct expansion. *Circulation* **78**, 186-201.

[23] Wells, R.G. 2013 Tissue mechanics and fibrosis. *Biochim Biophys Acta* **1832**, 884-890. (doi:10.1016/j.bbadis.2013.02.007).

[24] Gerdes, A.M. 2002 Cardiac myocyte remodeling in hypertrophy and progression to failure. *J Card Fail* **8**, S264-268. (doi:10.1054/jcaf.2002.129280).

[25] Pangonyte, D., Stalioraityte, E., Ziuraitiene, R., Kazlauskaite, D., Palubinskiene, J. & Balnyte, I. 2008 Cardiomyocyte remodeling in ischemic heart disease. *Medicina (Kaunas)* **44**, 848-854.

[26] Chiong, M., Wang, Z.V., Pedrozo, Z., Cao, D.J., Troncoso, R., Ibacache, M., Criollo, A., Nemchenko, A., Hill, J.A. & Lavandero, S. 2011 Cardiomyocyte death: mechanisms and translational implications. *Cell Death Dis* **2**, e244. (doi:10.1038/cddis.2011.130).

[27] Lesnefsky, E.J., Tandler, B., Ye, J., Slabe, T.J., Turkaly, J. & Hoppel, C.L. 1997 Myocardial ischemia decreases oxidative phosphorylation through cytochrome oxidase in subsarcolemmal mitochondria. *Am J Physiol* **273**, H1544-1554.

[28] Grynberg, A. & Demaison, L. 1996 Fatty acid oxidation in the heart. *J Cardiovasc Pharmacol* **28 Suppl 1**, S11-17.

[29] Graham, R.M., Frazier, D.P., Thompson, J.W., Haliko, S., Li, H., Wasserlauf, B.J., Spiga, M.G., Bishopric, N.H. & Webster, K.A. 2004 A unique pathway of cardiac myocyte death caused by hypoxia-acidosis. *J Exp Biol* **207**, 3189-3200. (doi:10.1242/jeb.01109).

[30] Frangogiannis, N.G. 2012 Regulation of the inflammatory response in cardiac repair. *Circ Res* **110**, 159-173. (doi:10.1161/CIRCRESAHA.111.243162).

[31] Kirichok, Y., Krapivinsky, G. & Clapham, D.E. 2004 The mitochondrial calcium uniporter is a highly selective ion channel. *Nature* **427**, 360-364. (doi:10.1038/nature02246).

[32] Peng, T.I. & Jou, M.J. 2010 Oxidative stress caused by mitochondrial calcium overload. *Ann N Y Acad Sci* **1201**, 183-188. (doi:10.1111/j.1749-6632.2010.05634.x).

[33] Gustafsson, A.B. & Gottlieb, R.A. 2008 Heart mitochondria: gates of life and death. *Cardiovasc Res* **77**, 334-343. (doi:10.1093/cvr/cvm005).

[34] Santulli, G., Xie, W., Reiken, S.R. & Marks, A.R. 2015 Mitochondrial calcium overload is a key determinant in heart failure. *Proc Natl Acad Sci U S A*. (doi:10.1073/pnas.1513047112).

[35] Palojoki, E., Saraste, A., Eriksson, A., Pulkki, K., Kallajoki, M., Voipio-Pulkki, L.M. & Tikkanen, I. 2001 Cardiomyocyte apoptosis and ventricular remodeling after myocardial infarction in rats. *Am J Physiol Heart Circ Physiol* **280**, H2726-2731.

[36] Crow, M.T., Mani, K., Nam, Y.J. & Kitsis, R.N. 2004 The mitochondrial death pathway and cardiac myocyte apoptosis. *Circ Res* **95**, 957-970. (doi:10.1161/01.RES.0000148632.35500.d9).

[37] Krijnen, P.A., Nijmeijer, R., Meijer, C.J., Visser, C.A., Hack, C.E. & Niessen, H.W. 2002 Apoptosis in myocardial ischaemia and infarction. *J Clin Pathol* **55**, 801-811.

[38] Kubasiak, L.A., Hernandez, O.M., Bishopric, N.H. & Webster, K.A. 2002 Hypoxia and acidosis activate cardiac myocyte death through the Bcl-2 family protein BNIP3. *Proc Natl Acad Sci U S A* **99**, 12825-12830. (doi:10.1073/pnas.202474099).

[39] Cleutjens, J.P., Kandala, J.C., Guarda, E., Guntaka, R.V. & Weber, K.T. 1995 Regulation of collagen degradation in the rat myocardium after infarction. *J Mol Cell Cardiol* **27**, 1281-1292.

[40] Ma, Y., de Castro Bras, L.E., Toba, H., Iyer, R.P., Hall, M.E., Winniford, M.D., Lange, R.A., Tyagi, S.C. & Lindsey, M.L. 2014 Myofibroblasts and the extracellular matrix network in post-myocardial infarction cardiac remodeling. *Pflugers Arch* **466**, 1113-1127. (doi:10.1007/s00424-014-1463-9).

[41] Raya, T.E., Gay, R.G., Lancaster, L., Aguirre, M., Moffett, C. & Goldman, S. 1988 Serial changes in left ventricular relaxation and chamber stiffness after large myocardial infarction in rats. *Circulation* **77**, 1424-1431.

[42] Olivetti, G., Capasso, J.M., Sonnenblick, E.H. & Anversa, P. 1990 Side-to-side slippage of myocytes participates in ventricular wall remodeling acutely after myocardial infarction in rats. *Circ Res* **67**, 23-34.

[43] Ju, H., Zhao, S., Tappia, P.S., Panagia, V. & Dixon, I.M. 1998 Expression of Gq alpha and PLC-beta in scar and border tissue in heart failure due to myocardial infarction. *Circulation* **97**, 892-899.

[44] Lorell, B.H. & Carabello, B.A. 2000 Left ventricular hypertrophy: pathogenesis, detection, and prognosis. *Circulation* **102**, 470-479.

[45] Kijima, K., Matsubara, H., Murasawa, S., Maruyama, K., Mori, Y., Ohkubo, N., Komuro, I., Yazaki, Y., Iwasaka, T. & Inada, M. 1996 Mechanical stretch induces enhanced expression of angiotensin II receptor subtypes in neonatal rat cardiac myocytes. *Circ Res* **79**, 887-897.

[46] Gao, X.M., Dart, A.M., Dewar, E., Jennings, G. & Du, X.J. 2000 Serial echocardiographic assessment of left ventricular dimensions and function after myocardial infarction in mice. *Cardiovasc Res* **45**, 330-338.

[47] Schaefer, A., Meyer, G.P., Hilfiker-Kleiner, D., Brand, B., Drexler, H. & Klein, G. 2005 Evaluation of Tissue Doppler Tei index for global left ventricular function in mice after myocardial infarction: comparison with Pulsed Doppler Tei index. *Eur J Echocardiogr* **6**, 367-375. (doi:10.1016/j.euje.2005.01.007).

[48] Teichholz, L.E., Cohen, M.V., Sonnenblick, E.H. & Gorlin, R. 1974 Study of left ventricular geometry and function by B-scan ultrasonography in patients with and without asynergy. *N Engl J Med* **291**, 1220-1226. (doi:10.1056/NEJM197412052912304).

[49] Folland, E.D., Parisi, A.F., Moynihan, P.F., Jones, D.R., Feldman, C.L. & Tow, D.E. 1979 Assessment of left ventricular ejection fraction and volumes by real-time, two-dimensional echocardiography. A comparison of cineangiographic and radionuclide techniques. *Circulation* **60**, 760-766.

[50] Benavides-Vallve, C., Corbacho, D., Iglesias-Garcia, O., Pelacho, B., Albiasu, E., Castano, S., Munoz-Barrutia, A., Prosper, F. & Ortiz-de-Solorzano, C. 2012 New strategies for echocardiographic evaluation of left ventricular function in a mouse model of long-term myocardial infarction. *PLoS One* **7**, e41691. (doi:10.1371/journal.pone.0041691).

[51] Kanno, S., Lerner, D.L., Schuessler, R.B., Betsuyaku, T., Yamada, K.A., Saffitz, J.E. & Kovacs, A. 2002 Echocardiographic evaluation of ventricular remodeling in a mouse model of myocardial infarction. *J Am Soc Echocardiogr* **15**, 601-609.

[52] Scherrer-Crosbie, M., Rodrigues, A.C., Hataishi, R. & Picard, M.H. 2007 Infarct size assessment in mice. *Echocardiography* **24**, 90-96. (doi:10.1111/j.1540-8175.2007.00357.x).

[53] van Melle, J.P., van der Vleuten, P.A., Hummel, Y.M., Nijveldt, R., Tio, R.A., Voors, A.A. & Zijlstra, F. 2010 Predictive value of tissue Doppler imaging for left ventricular ejection fraction, remodelling, and infarct size after percutaneous coronary intervention for acute myocardial infarction. *Eur J Echocardiogr* **11**, 596-601. (doi:10.1093/ejechocard/jeq023).

[54] Grayburn, P.A., Erickson, J.M., Escobar, J., Womack, L. & Velasco, C.E. 1995 Peripheral intravenous myocardial contrast echocardiography using a 2% dodecafluoropentane emulsion: identification of myocardial risk area and infarct size in the canine model of ischemia. *J Am Coll Cardiol* **26**, 1340-1347. (doi:10.1016/0735-1097(95)00306-1).

[55] Lafitte, S., Higashiyama, A., Masugata, H., Peters, B., Strachan, M., Kwan, O.L. & DeMaria, A.N. 2002 Contrast echocardiography can assess risk area and infarct size during coronary occlusion and reperfusion: experimental validation. *J Am Coll Cardiol* **39**, 1546-1554.

[56] Kaufmann, B.A., Lankford, M., Behm, C.Z., French, B.A., Klibanov, A.L., Xu, Y. & Lindner, J.R. 2007 High-resolution myocardial perfusion imaging in mice with high-frequency echocardiographic detection of a depot contrast agent. *J Am Soc Echocardiogr* **20**, 136-143. (doi:10.1016/j.echo.2006.08.008).

[57] Lepper, W., Belcik, T., Wei, K., Lindner, J.R., Sklenar, J. & Kaul, S. 2004 Myocardial contrast echocardiography. *Circulation* **109**, 3132-3135. (doi:10.1161/01.CIR.0000132613.53542.E9).

[58] Gray, G.A., White, C.I., Thomson, A., Kozak, A., Moran, C. & Jansen, M.A. 2013 Imaging the healing murine myocardial infarct in vivo: ultrasound, magnetic resonance imaging and fluorescence molecular tomography. *Exp Physiol* **98**, 606-613. (doi:10.1113/expphysiol.2012.064741).

[59] Golestani, R., Wu, C., Tio, R.A., Zeebregts, C.J., Petrov, A.D., Beekman, F.J., Dierckx, R.A., Boersma, H.H. & Slart, R.H. 2010 Small-animal SPECT and SPECT/CT: application in cardiovascular research. *Eur J Nucl Med Mol Imaging* **37**, 1766-1777. (doi:10.1007/s00259-009-1321-8).

[60] Liu, Z., Kastis, G.A., Stevenson, G.D., Barrett, H.H., Furenlid, L.R., Kupinski, M.A., Patton, D.D. & Wilson, D.W. 2002 Quantitative analysis of acute myocardial infarct in rat hearts with ischemia-reperfusion using a high-resolution stationary SPECT system. *J Nucl Med* **43**, 933-939.

[61] Vrachimis, A., Hermann, S., Mathe, D., Schober, O. & Schafers, M. 2012 Systematic evaluation of 99mTc-tetrofosmin versus 99mTc-sestamibi to study murine myocardial perfusion in small animal SPECT/CT. *EJNMMI Res* **2**, 21. (doi:10.1186/2191-219X-2-21).

[62] Greco, A., Petretta, M.P., Larobina, M., Gargiulo, S., Panico, M., Nekolla, S.G., Esposito, G., Petretta, M., Brunetti, A. & Cuocolo, A. 2012 Reproducibility and accuracy of non-invasive measurement of infarct size in mice with high-resolution PET/CT. *J Nucl Cardiol* **19**, 492-499. (doi:10.1007/s12350-012-9538-5).

[63] Xu, M., Yan, L., Xu, J., Yang, X. & Jiang, T. 2018 Predictors and prognosis for incident in-hospital heart failure in patients with preserved ejection fraction after first acute myocardial infarction: An observational study. *Medicine (Baltimore)* **97**, e11093. (doi:10.1097/MD.0000000000011093).

[64] Wu, J., You, J., Jiang, G., Li, L., Guan, A., Ye, Y., Li, D., Gong, H., Ge, J. & Zou, Y. 2012 Noninvasive estimation of infarct size in a mouse model of myocardial infarction by echocardiographic coronary perfusion. *J Ultrasound Med* **31**, 1111-1121.

[65] Abraham, T.P., Dimaano, V.L. & Liang, H.Y. 2007 Role of tissue Doppler and strain echocardiography in current clinical practice. *Circulation* **116**, 2597-2609. (doi:10.1161/CIRCULATIONAHA.106.647172).

[66] Humphrey, J.D. 2002 Cardiac Mechanics. *Cardiovascular Solid Mechanics: Cells, Tissues, and Organs* 599-729. New York, Springer-Verlag. (doi:10.1007/978-0-387-21576-1).

[67] Sengupta, P.P., Tajik, A.J., Chandrasekaran, K. & Khandheria, B.K. 2008 Twist mechanics of the left ventricle: principles and application. *JACC Cardiovasc Imaging* **1**, 366-376. (doi:10.1016/j.jcmg.2008.02.006).

[68] Geyer, H., Caracciolo, G., Abe, H., Wilansky, S., Carerj, S., Gentile, F., Nesser, H.J., Khandheria, B., Narula, J. & Sengupta, P.P. 2010 Assessment of myocardial mechanics using speckle tracking echocardiography: fundamentals and clinical applications. *J Am Soc Echocardiogr* **23**, 351-369; quiz 453-355. (doi:10.1016/j.echo.2010.02.015).

[69] Hung, C.L., Verma, A., Uno, H., Shin, S.H., Bourgoun, M., Hassanein, A.H., McMurray, J.J., Velazquez, E.J., Kober, L., Pfeffer, M.A., et al. 2010 Longitudinal and circumferential strain rate, left ventricular remodeling, and prognosis after myocardial infarction. *J Am Coll Cardiol* **56**, 1812-1822. (doi:10.1016/j.jacc.2010.06.044).

[70] Pellerin, D., Sharma, R., Elliott, P. & Veyrat, C. 2003 Tissue Doppler, strain, and strain rate echocardiography for the assessment of left and right systolic ventricular function. *Heart* **89 Suppl 3**, iii9-17.

[71] Hoit, B.D. 2011 Strain and strain rate echocardiography and coronary artery disease. *Circ Cardiovasc Imaging* **4**, 179-190. (doi:10.1161/CIRCIMAGING.110.959817).

[72] Urheim, S., Edvardsen, T., Torp, H., Angelsen, B. & Smiseth, O.A. 2000 Myocardial strain by Doppler echocardiography. Validation of a new method to quantify regional myocardial function. *Circulation* **102**, 1158-1164.

[73] Voigt, J.U., Arnold, M.F., Karlsson, M., Hubbert, L., Kukulski, T., Hatle, L. & Sutherland, G.R. 2000 Assessment of regional longitudinal myocardial strain rate derived from doppler myocardial imaging indexes in normal and infarcted myocardium. *J Am Soc Echocardiogr* **13**, 588-598.

[74] Hatle, L. & Sutherland, G.R. 2000 Regional myocardial function--a new approach. *Eur Heart J* **21**, 1337-1357. (doi:10.1053/euhj.2000.2251).

[75] Uematsu, M., Miyatake, K., Tanaka, N., Matsuda, H., Sano, A., Yamazaki, N., Hirama, M. & Yamagishi, M. 1995 Myocardial velocity gradient as a new indicator of regional left ventricular contraction: detection by a two-dimensional tissue Doppler imaging technique. *J Am Coll Cardiol* **26**, 217-223.

[76] Palmes, P.P., Masuyama, T., Yamamoto, K., Kondo, H., Sakata, Y., Takiuchi, S., Kuzuya, T. & Hori, M. 2000 Myocardial longitudinal motion by tissue velocity imaging in the evaluation of patients with myocardial infarction. *J Am Soc Echocardiogr* **13**, 818-826.

[77] Leitman, M., Lysyansky, P., Sidenko, S., Shir, V., Peleg, E., Binenbaum, M., Kaluski, E., Krakover, R. & Vered, Z. 2004 Two-dimensional strain-a novel software for real-time quantitative echocardiographic assessment of myocardial function. *J Am Soc Echocardiogr* **17**, 1021-1029. (doi:10.1016/j.echo.2004.06.019).

[78] De Craene, M., Piella, G., Camara, O., Duchateau, N., Silva, E., Doltra, A., D'Hooge, J., Brugada, J., Sitges, M. & Frangi, A.F. 2012 Temporal diffeomorphic free-form deformation: application to motion and strain estimation from 3D echocardiography. *Med Image Anal* **16**, 427-450. (doi:10.1016/j.media.2011.10.006).

[79] Wang, Y., Georgescu, B., Houle, H. & Comaniciu, D. 2010 Volumetric myocardial mechanics from 3D+ t ultrasound data with multi-model tracking. In *Statistical Atlases and Computational Models of the Heart* (pp. 184-193, Springer.

[80] Papademetris, X., Sinusas, A.J., Dione, D.P. & Duncan, J.S. 2001 Estimation of 3D left ventricular deformation from echocardiography. *Med Image Anal* **5**, 17-28.

[81] Papademetris, X., Sinusas, A.J., Dione, D.P., Constable, R.T. & Duncan, J.S. 2002 Estimation of 3-D left ventricular deformation from medical images using biomechanical models. *IEEE Trans Med Imaging* **21**, 786-800. (doi:10.1109/TMI.2002.801163).

[82] Elen, A., Choi, H.F., Loeckx, D., Gao, H., Claus, P., Suetens, P., Maes, F. & D'Hooge, J. 2008 Three-dimensional cardiac strain estimation using spatio-temporal elastic registration of ultrasound images: a feasibility study. *IEEE Trans Med Imaging* **27**, 1580-1591. (doi:10.1109/TMI.2008.2004420).

[83] Heyde, B., Barbosa, D., Claus, P., Maes, F. & D'hooge, J. 2013 Three-dimensional cardiac motion estimation based on non-rigid image registration using a novel transformation model adapted to the heart. In *Statistical Atlases and Computational Models of the Heart. Imaging and Modelling Challenges* (pp. 142-150, Springer.

[84] Alessandrini, M., Liebgott, H., Barbosa, D. & Bernard, O. 2013 Monogenic phase based optical flow computation for myocardial motion analysis in 3D echocardiography. *STACOM, ser. LNCS* **7746**, 159-168.

[85] Angelini, E.D. & Gerard, O. 2006 Review of myocardial motion estimation methods from optical flow tracking on ultrasound data. *Conf Proc IEEE Eng Med Biol Soc* **1**, 1537-1540. (doi:10.1109/IEMBS.2006.259640).

[86] Duan, Q., Parker, K.M., Lorsakul, A., Angelini, E.D., Hyodo, E., Homma, S., Holmes, J.W. & Laine, A.F. 2009 Quantitative Validation of Optical Flow Based Myocardial Strain Measures Using Sonomicrometry. *Proc IEEE Int Symp Biomed Imaging* **2009**, 454-457. (doi:10.1109/ISBI.2009.5193082).

[87] Li, Y., Garson, C.D., Xu, Y., Beyers, R.J., Epstein, F.H., French, B.A. & Hossack, J.A. 2007 Quantification and MRI validation of regional contractile dysfunction in mice post myocardial infarction using high resolution ultrasound. *Ultrasound Med Biol* **33**, 894-904. (doi:10.1016/j.ultrasmedbio.2006.12.008).

[88] Marwick, T.H., Leano, R.L., Brown, J., Sun, J.P., Hoffmann, R., Lysyansky, P., Becker, M. & Thomas, J.D. 2009 Myocardial strain measurement with 2-dimensional speckle-tracking echocardiography: definition of normal range. *JACC Cardiovasc Imaging* **2**, 80-84. (doi:10.1016/j.jcmg.2007.12.007).

[89] Li, Y., Garson, C.D., Xu, Y., Helm, P.A., Hossack, J.A. & French, B.A. 2011 Serial ultrasound evaluation of intramyocardial strain after reperfused myocardial infarction reveals that remote zone dyssynchrony develops in concert with left ventricular remodeling. *Ultrasound Med Biol* **37**, 1073-1086. (doi:10.1016/j.ultrasmedbio.2011.04.002).

[90] Wu, V.C., Takeuchi, M., Otani, K., Haruki, N., Yoshitani, H., Tamura, M., Abe, H., Lin, F.C. & Otsuji, Y. 2013 Effect of through-plane and twisting motion on left ventricular strain calculation: direct comparison between two-dimensional and three-dimensional speckle-tracking echocardiography. *J Am Soc Echocardiogr* **26**, 1274-1281 e1274. (doi:10.1016/j.echo.2013.07.006).

[91] Shehata, M.L., Cheng, S., Osman, N.F., Bluemke, D.A. & Lima, J.A. 2009 Myocardial tissue tagging with cardiovascular magnetic resonance. *J Cardiovasc Magn Reson* **11**, 55. (doi:10.1186/1532-429X-11-55).

[92] Zerhouni, E.A., Parish, D.M., Rogers, W.J., Yang, A. & Shapiro, E.P. 1988 Human heart: tagging with MR imaging--a method for noninvasive assessment of myocardial motion. *Radiology* **169**, 59-63. (doi:10.1148/radiology.169.1.3420283).

[93] Axel, L. & Dougherty, L. 1989 MR imaging of motion with spatial modulation of magnetization. *Radiology* **171**, 841-845. (doi:10.1148/radiology.171.3.2717762).

[94] Epstein, F.H., Yang, Z., Gilson, W.D., Berr, S.S., Kramer, C.M. & French, B.A. 2002 MR tagging early after myocardial infarction in mice demonstrates contractile dysfunction in adjacent and remote regions. *Magn Reson Med* **48**, 399-403. (doi:10.1002/mrm.10210).

[95] Oshinski, J.N., Yang, Z., Jones, J.R., Mata, J.F. & French, B.A. 2001 Imaging time after Gd-DTPA injection is critical in using delayed enhancement to determine infarct size accurately with magnetic resonance imaging. *Circulation* **104**, 2838-2842.

[96] Liu, W., Chen, J., Ji, S., Allen, J.S., Bayly, P.V., Wickline, S.A. & Yu, X. 2004 Harmonic phase MR tagging for direct quantification of Lagrangian strain in rat hearts after myocardial infarction. *Magn Reson Med* **52**, 1282-1290. (doi:10.1002/mrm.20276).

[97] Zhong, J., Liu, W. & Yu, X. 2009 Transmural myocardial strain in mouse: quantification of high-resolution MR tagging using harmonic phase (HARP) analysis. *Magn Reson Med* **61**, 1368-1373. (doi:10.1002/mrm.21942).

[98] Zhou, R., Pickup, S., Glickson, J.D., Scott, C.H. & Ferrari, V.A. 2003 Assessment of global and regional myocardial function in the mouse using cine and tagged MRI. *Magn Reson Med* **49**, 760-764. (doi:10.1002/mrm.10423).

[99] Ugolini, G.S., Pavesi, A., Rasponi, M., Fiore, G.B., Kamm, R. & Soncini, M. 2017 Human cardiac fibroblasts adaptive responses to controlled combined mechanical strain and oxygen changes in vitro. *Elife* **6**. (doi:10.7554/eLife.22847).

[100] Hafez, P., Chowdhury, S.R., Jose, S., Law, J.X., Ruszymah, B.H.I., Mohd Ramzisham, A.R. & Ng, M.H. 2018 Development of an In Vitro Cardiac Ischemic Model Using Primary Human Cardiomyocytes. *Cardiovasc Eng Technol* **9**, 529-538. (doi:10.1007/s13239-018-0368-8).

[101] Ruiz-Villalba, A., Mattiotti, A., Gunst, Q.D., Cano-Ballesteros, S., van den Hoff, M.J. & Ruijter, J.M. 2017 Reference genes for gene expression studies in the mouse heart. *Sci Rep* **7**, 24. (doi:10.1038/s41598-017-00043-9).

[102] Kubow, K.E., Klotzsch, E., Smith, M.L., Gourdon, D., Little, W.C. & Vogel, V. 2009 Crosslinking of cell-derived 3D scaffolds up-regulates the stretching and unfolding of new extracellular matrix assembled by reseeded cells. *Integr Biol (Camb)* **1**, 635-648. (doi:10.1039/b914996a).

[103] Nascimento, D.S., Valente, M., Esteves, T., de Pina Mde, F., Guedes, J.G., Freire, A., Quelhas, P. & Pinto-do, O.P. 2011 MIQuant--semi-automation of infarct size assessment in models of cardiac ischemic injury. *PLoS One* **6**, e25045. (doi:10.1371/journal.pone.0025045).

[104] Damen, F.W., Berman, A.G., Soepriatna, A.H., Ellis, J.M., Buttars, S.D., Aasa, K.L. & Goergen, C.J. 2017 High-Frequency 4-Dimensional Ultrasound (4DUS): A Reliable Method for Assessing Murine Cardiac Function. *Tomography* **3**, 180-187. (doi:10.18383/j.tom.2017.00016).

[105] Vanhoutte, L., Gerber, B.L., Gallez, B., Po, C., Magat, J., Balligand, J.L., Feron, O. & Moniotte, S. 2016 High field magnetic resonance imaging of rodents in cardiovascular research. *Basic Res Cardiol* **111**, 46. (doi:10.1007/s00395-016-0565-2).

[106] Boyle, J.J., Kume, M., Wyczalkowski, M.A., Taber, L.A., Pless, R.B., Xia, Y., Genin, G.M. & Thomopoulos, S. 2014 Simple and accurate methods for quantifying deformation, disruption, and development in biological tissues. *J R Soc Interface* **11**, 20140685. (doi:10.1098/rsif.2014.0685).

[107] Heidenreich, P.A., Trogdon, J.G., Khavjou, O.A., Butler, J., Dracup, K., Ezekowitz, M.D., Finkelstein, E.A., Hong, Y., Johnston, S.C., Khera, A., et al. 2011 Forecasting the future of cardiovascular disease in the United States: a policy statement from the American Heart Association. *Circulation* **123**, 933-944. (doi:10.1161/CIR.0b013e31820a55f5).

[108] Li, G., Citrin, D., Camphausen, K., Mueller, B., Burman, C., Mychalczak, B., Miller, R.W. & Song, Y. 2008 Advances in 4D medical imaging and 4D radiation therapy. *Technology in cancer research & treatment* **7**, 67-81.

[109] Mihalef, V., Ionasec, R.I., Sharma, P., Georgescu, B., Voigt, I., Suehling, M. & Comaniciu, D. 2011 Patient-specific modelling of whole heart anatomy, dynamics and haemodynamics from four-dimensional cardiac CT images. *Interface Focus* **1**, 286-296. (doi:10.1098/rsfs.2010.0036).

[110] Gao, M., Huang, J., Zhang, S., Qian, Z., Voros, S., Metaxas, D. & Axel, L. 2011 4D cardiac reconstruction using high resolution CT images. In *Functional Imaging and Modeling of the Heart* (pp. 153-160, Springer.

[111] Allen, B.D., Barker, A.J., Parekh, K., Sommerville, L.C., Schnell, S., Jarvis, K.B., Carr, M., Carr, J., Collins, J. & Markl, M. 2013 Incorporating time-resolved three-dimensional phase contrast (4D flow) MRI in clinical workflow: initial experiences at a large tertiary care medical center. *Resonance* **15**, P32.

[112] Stankovic, Z., Allen, B.D., Garcia, J., Jarvis, K.B. & Markl, M. 2014 4D flow imaging with MRI. *Cardiovasc Diagn Ther* **4**, 173-192. (doi:10.3978/j.issn.2223-3652.2014.01.02).

[113] Corsi, C., Saracino, G., Sarti, A. & Lamberti, C. 2002 Left ventricular volume estimation for real-time three-dimensional echocardiography. *IEEE Trans Med Imaging* **21**, 1202-1208. (doi:10.1109/TMI.2002.804418).

[114] Qin, Y., Zhang, Y., Zhou, X., Wang, Y., Sun, W., Chen, L., Zhao, D., Zhan, Y. & Cai, A. 2014 Four-dimensional echocardiography with spatiotemporal image correlation and inversion mode for detection of congenital heart disease. *Ultrasound in medicine & biology* **40**, 1434-1441. (doi:10.1016/j.ultrasmedbio.2014.02.008).

[115] Schoechlin, S., Ruile, P., Neumann, F.J. & Pache, G. 2015 Early hypoattenuated leaflet thickening and restricted leaflet motion of a Lotus transcatheter heart valve detected by 4D computed tomography angiography. *EuroIntervention* **11**, e1. (doi:10.4244/EIJV11I5A118).

[116] Po, M.J., Lorsakul, A., Duan, Q., Yeroushalmi, K.J., Hyodo, E., Oe, Y., Homma, S. & Laine, A.F. 2010 In-vivo clinical validation of cardiac deformation and strain measurements from 4D ultrasound. *Conf Proc IEEE Eng Med Biol Soc* **2010**, 41-44. (doi:10.1109/IEMBS.2010.5626332).

[117] Derwich, W., Wittek, A., Pfister, K., Nelson, K., Bereiter-Hahn, J., Fritzen, C.P., Blase, C. & Schmitz-Rixen, T. 2016 High Resolution Strain Analysis Comparing Aorta and Abdominal Aortic Aneurysm with Real Time Three Dimensional Speckle Tracking Ultrasound. *European journal of vascular and endovascular surgery : the official journal of the European Society for Vascular Surgery* **51**, 187-193. (doi:10.1016/j.ejvs.2015.07.042).

[118] Fox, J.G., Barthold, S.W., Davisson, M.T., Newcomer, C.E., Quimby, F.W. & Smith, A.L. 2007 The Mouse in Biomedical Research.

[119] Badea, C.T., Hedlund, L.W., Mackel, J.F., Mao, L., Rockman, H.A. & Johnson, G.A. 2007 Cardiac micro-computed tomography for morphological and functional phenotyping of muscle LIM protein null mice. *Molecular imaging* **6**, 261-268.

[120] Polte, C.L., Lagerstrand, K.M., Gao, S.A., Lamm, C.R. & Bech-Hanssen, O. 2015 Quantification of Left Ventricular Linear, Areal and Volumetric Dimensions: A Phantom and in Vivo Comparison of 2-D and Real-Time 3-D Echocardiography with Cardiovascular Magnetic Resonance. *Ultrasound in medicine & biology*. (doi:10.1016/j.ultrasmedbio.2015.03.001).

[121] Hoit, B.D. 2001 New approaches to phenotypic analysis in adult mice. *J Mol Cell Cardiol* **33**, 27-35. (doi:10.1006/jmcc.2000.1294).

[122] Keall, P.J., Vedam, S.S., George, R. & Williamson, J.F. 2007 Respiratory regularity gated 4D CT acquisition: concepts and proof of principle. *Australas Phys Eng Sci Med* **30**, 211-220.

[123] Coatney, R.W. 2001 Ultrasound imaging: principles and applications in rodent research. *ILAR J* **42**, 233-247.

[124] Hoole, S.P., Boyd, J., Ninios, V., Parameshwar, J. & Rusk, R.A. 2008 Measurement of cardiac output by real-time 3D echocardiography in patients undergoing assessment for cardiac transplantation. *European journal of echocardiography : the journal of the Working Group on Echocardiography of the European Society of Cardiology* **9**, 334-337. (doi:10.1016/j.euje.2007.03.033).

[125] Damen, F.W., Adelsperger, A.R., Wilson, K.E. & Goergen, C.J. 2015 Comparison of Traditional and Integrated Digital Anesthetic Vaporizers. *J Am Assoc Lab Anim Sci* **54**, 756-762.

[126] Kolk, M.V., Meyberg, D., Deuse, T., Tang-Quan, K.R., Robbins, R.C., Reichenspurner, H. & Schrepfer, S. 2009 LAD-ligation: a murine model of myocardial infarction. *J Vis Exp*. (doi:10.3791/1438).

[127] Muthuramu, I., Lox, M., Jacobs, F. & De Geest, B. 2014 Permanent ligation of the left anterior descending coronary artery in mice: a model of post-myocardial infarction remodelling and heart failure. *J Vis Exp*. (doi:10.3791/52206).

[128] Daugherty, A. & Cassis, L. 1999 Chronic angiotensin II infusion promotes atherogenesis in low density lipoprotein receptor -/- mice. *Ann N Y Acad Sci* **892**, 108-118.

[129] Daugherty, A., Manning, M.W. & Cassis, L.A. 2000 Angiotensin II promotes atherosclerotic lesions and aneurysms in apolipoprotein E-deficient mice. *J Clin Invest* **105**, 1605-1612. (doi:10.1172/JCI7818).

[130] Lang, R.M., Bierig, M., Devereux, R.B., Flachskampf, F.A., Foster, E., Pellikka, P.A., Picard, M.H., Roman, M.J., Seward, J., Shanewise, J.S., et al. 2005 Recommendations for chamber quantification: a report from the American Society of Echocardiography's Guidelines and Standards Committee and the Chamber Quantification Writing Group, developed in conjunction with the European Association of Echocardiography, a branch of the European Society of Cardiology. *Journal of the American Society of Echocardiography : official publication of the American Society of Echocardiography* **18**, 1440-1463. (doi:10.1016/j.echo.2005.10.005).

[131] Lang, R.M., Badano, L.P., Mor-Avi, V., Afilalo, J., Armstrong, A., Ernande, L., Flachskampf, F.A., Foster, E., Goldstein, S.A., Kuznetsova, T., et al. 2015 Recommendations for cardiac chamber quantification by echocardiography in adults: an update from the American Society of Echocardiography and the European Association of Cardiovascular Imaging. *Journal of the American Society of Echocardiography : official publication of the American Society of Echocardiography* **28**, 1-39 e14. (doi:10.1016/j.echo.2014.10.003).

[132] Dele-Michael, A.O., Fujikura, K., Devereux, R.B., Islam, F., Hriljac, I., Wilson, S.R., Lin, F. & Weinsaft, J.W. 2013 Left ventricular stroke volume quantification by contrast echocardiography - comparison of linear and flow-based methods to cardiac magnetic resonance. *Echocardiography* **30**, 880-888. (doi:10.1111/echo.12155).

[133] Holzapfel, G.A. 2000 Nonlinear Solid Mechanics: A Continuum Approach for Engineering.

[134] Sonesson, B., Hansen, F. & Lanne, T. 1997 Abdominal aortic aneurysm: a general defect in the vasculature with focal manifestations in the abdominal aorta? *J Vasc Surg* **26**, 247-254.

[135] Ailawadi, G., Eliason, J.L. & Upchurch, G.R., Jr. 2003 Current concepts in the pathogenesis of abdominal aortic aneurysm. *J Vasc Surg* **38**, 584-588.

[136] Phillips, E.H., Yrineo, A.A., Schroeder, H.D., Wilson, K.E., Cheng, J.-X. & Goergen, C.J. 2014 Morphological and Biomechanical Differences in the Elastase and AngII apoE−/− Rodent Models of Abdominal Aortic Aneurysms. *BioMed Research International*.

[137] Otterstad, J.E. 2002 Measuring left ventricular volume and ejection fraction with the biplane Simpson's method. *Heart* **88**, 559-560.

[138] Kasai, T., Depuey, E.G. & Shah, A.A. 2004 Compared with 3-dimensional analysis, 2-dimensional gated SPECT analysis overestimates left ventricular ejection fraction in patients with regional dyssynchrony. *Journal of nuclear cardiology : official publication of the American Society of Nuclear Cardiology* **11**, 159-164. (doi:10.1016/j.nuclcard.2003.11.005).

[139] Michael, L.H., Entman, M.L., Hartley, C.J., Youker, K.A., Zhu, J., Hall, S.R., Hawkins, H.K., Berens, K. & Ballantyne, C.M. 1995 Myocardial ischemia and reperfusion: a murine model. *Am J Physiol* **269**, H2147-2154.

[140] Brekken, R., Bang, J., Odegard, A., Aasland, J., Hernes, T.A. & Myhre, H.O. 2006 Strain estimation in abdominal aortic aneurysms from 2-D ultrasound. *Ultrasound in medicine & biology* **32**, 33-42. (doi:10.1016/j.ultrasmedbio.2005.09.007).

[141] Taniguchi, R., Hoshina, K., Hosaka, A., Miyahara, T., Okamoto, H., Shigematsu, K., Miyata, T. & Watanabe, T. 2014 Strain analysis of wall motion in abdominal aortic aneurysms. *Ann Vasc Dis* **7**, 393-398. (doi:10.3400/avd.oa.14-00067).

[142] Trachet, B., Fraga-Silva, R.A., Londono, F.J., Swillens, A., Stergiopulos, N. & Segers, P. 2015 Performance comparison of ultrasound-based methods to assess aortic diameter and stiffness in normal and aneurysmal mice. *PLoS One* **10**, e0129007. (doi:10.1371/journal.pone.0129007).

[143] Goergen, C.J., Azuma, J., Barr, K.N., Magdefessel, L., Kallop, D.Y., Gogineni, A., Grewall, A., Weimer, R.M., Connolly, A.J., Dalman, R.L., et al. 2011 Influences of aortic motion and curvature on vessel expansion in murine experimental aneurysms. *Arteriosclerosis, thrombosis, and vascular biology* **31**, 270-279. (doi:10.1161/ATVBAHA.110.216481).

[144] Luo, J., Fujikura, K., Tyrie, L.S., Tilson, M.D. & Konofagou, E.E. 2009 Pulse wave imaging of normal and aneurysmal abdominal aortas in vivo. *IEEE Trans Med Imaging* **28**, 477-486. (doi:10.1109/TMI.2008.928179).

[145] Nandlall, S.D., Goldklang, M.P., Kalashian, A., Dangra, N.A., D'Armiento, J.M. & Konofagou, E.E. 2014 Monitoring and staging abdominal aortic aneurysm disease with pulse wave imaging. *Ultrasound in medicine & biology* **40**, 2404-2414. (doi:10.1016/j.ultrasmedbio.2014.04.013).

[146] Nandlall, S.D. & Konofagou, E.E. 2016 Assessing the Stability of Aortic Aneurysms with Pulse Wave Imaging. *Radiology* **281**, 772-781. (doi:10.1148/radiol.2016151407).

[147] Goergen, C.J., Barr, K.N., Huynh, D.T., Eastham-Anderson, J.R., Choi, G., Hedehus, M., Dalman, R.L., Connolly, A.J., Taylor, C.A., Tsao, P.S., et al. 2010 In vivo quantification of murine aortic cyclic strain, motion, and curvature: implications for abdominal aortic aneurysm growth. *J Magn Reson Imaging* **32**, 847-858. (doi:10.1002/jmri.22331).

[148] Franck, C., Hong, S., Maskarinec, S.A., Tirrell, D.A. & Ravichandran, G. 2007 Three-dimensional full-field measurements of large deformations in soft materials using confocal microscopy and digital volume correlation *Exp Mech* **47**, 427-438. (doi:10.1007/s11340-007-9037-9).

[149] Bayly, P.V., Clayton, E.H. & Genin, G.M. 2012 Quantitative imaging methods for the development and validation of brain biomechanics models. *Annu Rev Biomed Eng* **14**, 369-396. (doi:10.1146/annurev-bioeng-071811-150032).

[150] Rohlfing, T., Maurer, C.R., Jr., Bluemke, D.A. & Jacobs, M.A. 2003 Volume-preserving nonrigid registration of MR breast images using free-form deformation with an incompressibility constraint. *IEEE Trans Med Imaging* **22**, 730-741. (doi:10.1109/TMI.2003.814791).

[151] Zhang, Z., Zhu, M., Ashraf, M., Broberg, C.S., Sahn, D.J. & Song, X. 2014 Right ventricular strain analysis from three-dimensional echocardiography by using temporally diffeomorphic motion estimation. *Med Phys* **41**, 122902. (doi:10.1118/1.4901253).

[152] Veress, A.I., Phatak, N. & Weiss, J.A. 2005 *Deformable image registration with hyperelastic warping*. Boston, MA, Springer; 487-533 p.

[153] Veress, A.I., Weiss, J.A., Huesman, R.H., Reutter, B.W., Taylor, S.E., Sitek, A., Feng, B., Yang, Y. & Gullberg, G.T. 2008 Measuring regional changes in the diastolic deformation of the left ventricle of SHR rats using microPET technology and hyperelastic warping. *Ann Biomed Eng* **36**, 1104-1117. (doi:10.1007/s10439-008-9497-9).

[154] Young, A.A. & Axel, L. 1992 Three-dimensional motion and deformation of the heart wall: estimation with spatial modulation of magnetization--a model-based approach. *Radiology* **185**, 241-247. (doi:10.1148/radiology.185.1.1523316).

[155] Young, A.A., Fayad, Z.A. & Axel, L. 1996 Right ventricular midwall surface motion and deformation using magnetic resonance tagging. *Am J Physiol* **271**, H2677-2688. (doi:10.1152/ajpheart.1996.271.6.H2677).

[156] Baker, S. & Matthews, I. 2004 Lucas-Kanade 20 Years On: A Unifying Framework. *International Journal of Computer Vision* **56**, 221-255.

[157] Saito, S., Masuda, K., Mori, Y., Nakatani, S., Yoshioka, Y. & Murase, K. 2017 Mapping of left ventricle wall thickness in mice using 11.7-T magnetic resonance imaging. *Magn Reson Imaging* **36**, 128-134. (doi:10.1016/j.mri.2016.10.030).

[158] Yingchoncharoen, T., Agarwal, S., Popovic, Z.B. & Marwick, T.H. 2013 Normal ranges of left ventricular strain: a meta-analysis. *J Am Soc Echocardiogr* **26**, 185-191. (doi:10.1016/j.echo.2012.10.008).

[159] Gabbay, U. & Yosefy, C. 2010 The underlying causes of chordae tendinae rupture: a systematic review. *Int J Cardiol* **143**, 113-118. (doi:10.1016/j.ijcard.2010.02.011).

[160] Ritchie, J., Jimenez, J., He, Z., Sacks, M.S. & Yoganathan, A.P. 2006 The material properties of the native porcine mitral valve chordae tendineae: an in vitro investigation. *J Biomech* **39**, 1129-1135. (doi:10.1016/j.jbiomech.2005.01.024).

[161] Zuo, K., Pham, T., Li, K., Martin, C., He, Z. & Sun, W. 2016 Characterization of biomechanical properties of aged human and ovine mitral valve chordae tendineae. *J Mech Behav Biomed Mater* **62**, 607-618. (doi:10.1016/j.jmbbm.2016.05.034).

[162] Liu, Y., Birman, V., Chen, C., Thomopoulos, S. & Genin, G.M. 2011 Mechanisms of Bimaterial Attachment at the Interface of Tendon to Bone. *J Eng Mater Technol* **133**. (doi:10.1115/1.4002641).

[163] St John Sutton, M., Pfeffer, M.A., Moye, L., Plappert, T., Rouleau, J.L., Lamas, G., Rouleau, J., Parker, J.O., Arnold, M.O., Sussex, B., et al. 1997 Cardiovascular death and left ventricular remodeling two years after myocardial infarction: baseline predictors and impact of long-term use of captopril: information from the Survival and Ventricular Enlargement (SAVE) trial. *Circulation* **96**, 3294-3299. (doi:10.1161/01.cir.96.10.3294).

[164] Richardson, W.J. & Holmes, J.W. 2015 Why Is Infarct Expansion Such an Elusive Therapeutic Target? *J Cardiovasc Transl Res* **8**, 421-430. (doi:10.1007/s12265-015-9652-2).

[165] Zimmerman, S.D., Karlon, W.J., Holmes, J.W., Omens, J.H. & Covell, J.W. 2000 Structural and mechanical factors influencing infarct scar collagen organization. *Am J Physiol Heart Circ Physiol* **278**, H194-200. (doi:10.1152/ajpheart.2000.278.1.H194).

[166] Cahill, T.J. & Kharbanda, R.K. 2017 Heart failure after myocardial infarction in the era of primary percutaneous coronary intervention: Mechanisms, incidence and identification of patients at risk. *World J Cardiol* **9**, 407-415. (doi:10.4330/wjc.v9.i5.407).

[167] van den Borne, S.W., Diez, J., Blankesteijn, W.M., Verjans, J., Hofstra, L. & Narula, J. 2010 Myocardial remodeling after infarction: the role of myofibroblasts. *Nat Rev Cardiol* **7**, 30-37. (doi:10.1038/nrcardio.2009.199).

[168] D'Elia, N., D'Hooge, J. & Marwick, T.H. 2015 Association Between Myocardial Mechanics and Ischemic LV Remodeling. *JACC Cardiovasc Imaging* **8**, 1430-1443. (doi:10.1016/j.jcmg.2015.10.005).

[169] Bhan, A., Sirker, A., Zhang, J., Protti, A., Catibog, N., Driver, W., Botnar, R., Monaghan, M.J. & Shah, A.M. 2014 High-frequency speckle tracking echocardiography in the assessment of left ventricular function and remodeling after murine myocardial infarction. *Am J Physiol Heart Circ Physiol* **306**, H1371-1383. (doi:10.1152/ajpheart.00553.2013).

[170] Biere, L., Donal, E., Terrien, G., Kervio, G., Willoteaux, S., Furber, A. & Prunier, F. 2014 Longitudinal strain is a marker of microvascular obstruction and infarct size in patients with acute ST-segment elevation myocardial infarction. *PLoS One* **9**, e86959. (doi:10.1371/journal.pone.0086959).

[171] Bauer, M., Cheng, S., Jain, M., Ngoy, S., Theodoropoulos, C., Trujillo, A., Lin, F.C. & Liao, R. 2011 Echocardiographic speckle-tracking based strain imaging for rapid cardiovascular phenotyping in mice. *Circ Res* **108**, 908-916. (doi:10.1161/CIRCRESAHA.110.239574).

[172] Torres, W.M., Jacobs, J., Doviak, H., Barlow, S.C., Zile, M.R., Shazly, T. & Spinale, F.G. 2018 Regional and temporal changes in left ventricular strain and stiffness in a porcine model of myocardial infarction. *Am J Physiol Heart Circ Physiol* **315**, H958-H967. (doi:10.1152/ajpheart.00279.2018).

[173] Soepriatna, A.H., Damen, F.W., Vlachos, P.P. & Goergen, C.J. 2018 Cardiac and respiratory-gated volumetric murine ultrasound. *Int J Cardiovasc Imaging* **34**, 713-724. (doi:10.1007/s10554-017-1283-z).

[174] Grune, J., Blumrich, A., Brix, S., Jeuthe, S., Drescher, C., Grune, T., Foryst-Ludwig, A., Messroghli, D., Kuebler, W.M., Ott, C., et al. 2018 Evaluation of a commercial multi-dimensional echocardiography technique for ventricular volumetry in small animals. *Cardiovasc Ultrasound* **16**, 10. (doi:10.1186/s12947-018-0128-9).

[175] Ahn, H.S., Kim, Y.K., Song, H.C., Choi, E.J., Kim, G.H., Cho, J.S., Ihm, S.H., Kim, H.Y., Park, C.S. & Youn, H.J. 2017 The impact of preload on 3-dimensional deformation parameters: principal strain, twist and torsion. *Cardiovasc Ultrasound* **15**, 22. (doi:10.1186/s12947-017-0111-x).

[176] Xia, J.Z., Xia, J.Y., Li, G., Ma, W.Y. & Wang, Q.Q. 2014 Left ventricular strain examination of different aged adults with 3D speckle tracking echocardiography. *Echocardiography* **31**, 335-339. (doi:10.1111/echo.12367).

[177] Boyle, J., Soepriatna, A., Damen, F., Rowe, R., Pless, R., Kovacs, A., Goergen, C., Thomopoulos, S. & Genin, G.M. 2018 Accurate and noise insensitive strain mapping enables ultrasound analysis of cardiac function in three dimensions. *J Biomech Eng*. (doi:10.1115/1.4041576).

[178] Satriano, A., Heydari, B., Narous, M., Exner, D.V., Mikami, Y., Attwood, M.M., Tyberg, J.V., Lydell, C.P., Howarth, A.G., Fine, N.M., et al. 2017 Clinical feasibility and validation of 3D principal strain analysis from cine MRI: comparison to 2D strain by MRI and 3D speckle tracking echocardiography. *Int J Cardiovasc Imaging* **33**, 1979-1992. (doi:10.1007/s10554-017-1199-7).

[179] Young, A.A., French, B.A., Yang, Z., Cowan, B.R., Gilson, W.D., Berr, S.S., Kramer, C.M. & Epstein, F.H. 2006 Reperfused myocardial infarction in mice: 3D mapping of late gadolinium enhancement and strain. *J Cardiovasc Magn Reson* **8**, 685-692. (doi:10.1080/10976640600721767).

[180] Hashmi, S. & Al-Salam, S. 2015 Acute myocardial infarction and myocardial ischemia-reperfusion injury: a comparison. *Int J Clin Exp Pathol* **8**, 8786-8796.

[181] Updegrove, A., Wilson, N.M., Merkow, J., Lan, H., Marsden, A.L. & Shadden, S.C. 2017 SimVascular: An Open Source Pipeline for Cardiovascular Simulation. *Ann Biomed Eng* **45**, 525-541. (doi:10.1007/s10439-016-1762-8).

[182] Chernak Slane, L. & Thelen, D.G. 2014 The use of 2D ultrasound elastography for measuring tendon motion and strain. *J Biomech* **47**, 750-754. (doi:10.1016/j.jbiomech.2013.11.023).

[183] O'Connell, G.D., Johannessen, W., Vresilovic, E.J. & Elliott, D.M. 2007 Human internal disc strains in axial compression measured noninvasively using magnetic resonance imaging. *Spine (Phila Pa 1976)* **32**, 2860-2868. (doi:10.1097/BRS.0b013e31815b75fb).

[184] Cerqueira, M.D., Weissman, N.J., Dilsizian, V., Jacobs, A.K., Kaul, S., Laskey, W.K., Pennell, D.J., Rumberger, J.A., Ryan, T., Verani, M.S., et al. 2002 Standardized myocardial segmentation and nomenclature for tomographic imaging of the heart. A statement for healthcare professionals from the Cardiac Imaging Committee of the Council on Clinical Cardiology of the American Heart Association. *Circulation* **105**, 539-542. (doi:10.1161/hc0402.102975).

[185] Diwan, A., Krenz, M., Syed, F.M., Wansapura, J., Ren, X., Koesters, A.G., Li, H., Kirshenbaum, L.A., Hahn, H.S., Robbins, J., et al. 2007 Inhibition of ischemic cardiomyocyte apoptosis through targeted ablation of Bnip3 restrains postinfarction remodeling in mice. *J Clin Invest* **117**, 2825-2833. (doi:10.1172/JCI32490).

[186] Schneider, C.A., Rasband, W.S. & Eliceiri, K.W. 2012 NIH Image to ImageJ: 25 years of image analysis. *Nat Methods* **9**, 671-675. (doi:10.1038/nmeth.2089).

[187] Thevenaz, P. & Unser, M. 2007 User-friendly semiautomated assembly of accurate image mosaics in microscopy. *Microsc Res Tech* **70**, 135-146. (doi:10.1002/jemt.20393).

[188] Richardson, W.J. & Holmes, J.W. 2016 Emergence of Collagen Orientation Heterogeneity in Healing Infarcts and an Agent-Based Model. *Biophys J* **110**, 2266-2277. (doi:10.1016/j.bpj.2016.04.014).

[189] Fomovsky, G.M., Rouillard, A.D. & Holmes, J.W. 2012 Regional mechanics determine collagen fiber structure in healing myocardial infarcts. *J Mol Cell Cardiol* **52**, 1083-1090. (doi:10.1016/j.yjmcc.2012.02.012).

[190] Van De Water, L., Varney, S. & Tomasek, J.J. 2013 Mechanoregulation of the Myofibroblast in Wound Contraction, Scarring, and Fibrosis: Opportunities for New Therapeutic Intervention. *Adv Wound Care (New Rochelle)* **2**, 122-141. (doi:10.1089/wound.2012.0393).

[191] Preda, M.B. & Burlacu, A. 2010 Electrocardiography as a tool for validating myocardial ischemia-reperfusion procedures in mice. *Comp Med* **60**, 443-447.

[192] Thibault, H., Gomez, L., Donal, E., Pontier, G., Scherrer-Crosbie, M., Ovize, M. & Derumeaux, G. 2007 Acute myocardial infarction in mice: assessment of transmurality by strain rate imaging. *Am J Physiol Heart Circ Physiol* **293**, H496-502. (doi:10.1152/ajpheart.00087.2007).

[193] Gao, X.M., White, D.A., Dart, A.M. & Du, X.J. 2012 Post-infarct cardiac rupture: recent insights on pathogenesis and therapeutic interventions. *Pharmacol Ther* **134**, 156-179. (doi:10.1016/j.pharmthera.2011.12.010).

[194] Hankiewicz, J.H., Goldspink, P.H., Buttrick, P.M. & Lewandowski, E.D. 2008 Principal strain changes precede ventricular wall thinning during transition to heart failure in a mouse model of dilated cardiomyopathy. *Am J Physiol Heart Circ Physiol* **294**, H330-336. (doi:10.1152/ajpheart.01109.2007).

[195] Pilla, J.J., Koomalsingh, K.J., McGarvey, J.R., Witschey, W.R., Dougherty, L., Gorman, J.H., 3rd & Gorman, R.C. 2015 Regional myocardial three-dimensional principal strains during postinfarction remodeling. *Ann Thorac Surg* **99**, 770-778. (doi:10.1016/j.athoracsur.2014.10.067).

[196] Eshelby, J.D. 1957 The Determination of the Elastic Field of an Ellipsoidal Inclusion and Related Problems. *Proc R Soc London A Math Phys Eng Sci* **241**.

[197] Tada, H., Paris, P.C. & Irwin, G.R. 2000 *The Stress Analysis of Cracks Handbook*. 3 ed.

PUBLICATIONS

The following list provides a comprehensive view of all published manuscripts and their scientific impact as quantified by the number of citations.

1. J. B. Lin, E. H. Phillips, T. E. Riggins, G. S. Sangha, S. Chakraborty, J. Y. Lee, R. J. Lycke, C. L. Hernandez, **A. H. Soepriatna**, B. R. Thorne, A. A. Yrineo, and C. J. Goergen, "Imaging of Small Animal Peripheral Artery Disease Models: Recent Advancements and Translational Potential," *Int J Mol Sci,* May 2015 (*Review Article*). – Citations: 19

2. F. W. Damen, A. G. Berman, **A. H. Soepriatna**, J. M. Ellis, S. Buttars, K. Aasa, and C. J. Goergen, "High Frequency Four-Dimensional Ultrasound (4DUS): A Reliable Method for Assessing Murine Cardiac Function," *Tomography*, October 2017 (*Original Contribution*). - Citations: 5

3. **A. H. Soepriatna**, F. W. Damen, P. P. Vlachos, and C. J. Goergen, "Cardiac and Respiratory-Gated Volumetric Murine Ultrasound," *Int J Cardiovasc Imaging*, May 2018 (*Original Contribution*). – Citations: 7

4. J. J. Boyle, **A. H. Soepriatna**, F. W. Damen, R. A. Rowe, R. B. Pless, A. Kovacs, C. J. Goergen, S. Thomopoulos, and G. M. Genin, "Regularization-Free Strain Mapping in Three Dimensions, With Application to Cardiac Ultrasound," *J Biomech Eng*, October 2018 (*Original Contribution*). - Citations: 2

5. A. M. Dieterly, G. Uzunalli, **A. H. Soepriatna**, C. J. Goergen, and L. T. Lyle, "Epithelial-Mesenchymal Transition Phenotypes in Vertebral Metastases of Lung Cancer," *Toxicol Pathol*, February 2019 (*Original Contribution*). – Citations: 0

6. H. L. Cebull, **A. H. Soepriatna**, J. J. Boyle, S. M. Rothenberger, and C. J. Goergen, "Strain Mapping from Four-Dimensional Ultrasound Reveals Complex Remodeling in Dissecting Murine Abdominal Aortic Aneurysms," *J Biomech Eng,* March 2019 (*Original Contribution*). – Citations: 3

7. G. Uzunalli, A. M. Dieterly, C. Kemet, H. Weng, **A. H. Soepriatna**, C. J. Goergen, A. B. Shinde, M. Wendt, and L. T. Lyle, "Dynamic Transition of the Blood-Brain Barrier in the Development of Non-small Cell Lung Cancer Brain Metastases," *Oncotarget*, October 2019 (*Original Contribution*). – Citations: 0

8. **A. H. Soepriatna**, A. K. Yeh, A. D. Clifford, S. E. Bezci, G. D. O'Connell, and C. J. Goergen, "Three-Dimensional Myocardial Strain Correlates with Murine Left Ventricular Remodeling Severity Post-Infarction," *J Royal Soc Interface*, November 2019 (*Original Contribution*). – Citations: 0